

2012

# Surface Science Studies of Nitrogen-Containing Cyclic Hydrocarbons on Pt(111) and Sn/Pt(111) Surface Alloys

Lindsey Ann Welch  
*Lehigh University*

Follow this and additional works at: <http://preserve.lehigh.edu/etd>

---

## Recommended Citation

Welch, Lindsey Ann, "Surface Science Studies of Nitrogen-Containing Cyclic Hydrocarbons on Pt(111) and Sn/Pt(111) Surface Alloys" (2012). *Theses and Dissertations*. Paper 1336.

This Dissertation is brought to you for free and open access by Lehigh Preserve. It has been accepted for inclusion in Theses and Dissertations by an authorized administrator of Lehigh Preserve. For more information, please contact [preserve@lehigh.edu](mailto:preserve@lehigh.edu).

Surface Science Studies of Nitrogen-Containing Cyclic Hydrocarbons on Pt(111) and  
Sn/Pt(111) Surface Alloys

by

Lindsey A. Welch

A Dissertation

Presented to the Graduate and Research Committee

of Lehigh University

in Candidacy for the Degree of

Doctor of Philosophy

in

The Department of Chemistry

Lehigh University

September 2012

© 2012 Copyright  
Lindsey A. Welch

Approved and recommended for acceptance as a dissertation in partial fulfillment of the requirements for the degree of Doctor of Philosophy

Lindsey A. Welch

Surface Science Studies of Nitrogen-Containing Cyclic Hydrocarbons on Pt(111) and Sn/Pt(111) Surface Alloys

---

Defense Date

---

Approved Date

---

David T. Moore  
(Dissertation Co-Director)

---

Bruce E. Koel  
(Dissertation Co-Director)

Committee Members:

---

Gregory S. Ferguson

---

Israel E. Wachs

## ACKNOWLEDGEMENTS

First, I would like to thank Prof. Bruce E. Koel, my advisor, for his knowledge and guidance while pursuing my degree here at Lehigh University. His passion for science has inspired me and helped me grow into the chemist I am today. I thank the members of my dissertation committee, Prof. Gregory Ferguson, Prof. David Moore, and Prof. Israel E. Wachs for their guidance and support along the way. Each of you has played an important role in contributing to my progress and I have valued you as mentors.

I would like to acknowledge my fellow group members, Dr. Mauricio Valencia Ramos, Dr. Xiaofang Yang, Jie Fu, and John Martin. Also, the guidance of Dr. Alfred Miller with the Scienta ESCA facility and the assistance of Mr. Joseph A. Zelinski in the Physics Department machine shop were invaluable in the process of completing my degree.

I thank my parents, family and friends for their love, support, and encouragement. I know it was hard to understand the process from the outside looking in, but you were always supportive of me and I appreciate your enthusiasm. Mom, it was a joy pursuing our degrees at the same time.

Finally, I would like to recognize my boyfriend, Chris Montis. I love you and appreciate your understanding, love, and support during this long process. You were there in the good times and the bad and we made it through together.

Funding from the Lehigh University Chemistry Department and The National Science Foundation is gratefully acknowledged.

## TABLE OF CONTENTS

	Page Number
I. List of Tables	vii
II. List of Figures	viii
III. List of Abbreviations	x
IV. Abstract	1
V. Chapter 1: Introduction	2
1.1. Use of Pt and SnPt Alloys in Catalysis	3
1.2. Definitions Used in Sn/Pt(111) Studies	5
1.3. Motivation for Current Work	8
1.4. References	10
VI. Chapter 2: Experimental Methods	
2.1. Scienta ESCA 300 Chamber	14
A. Manipulator and Crystal Mounting	
B. Sample Preparation and Dosers	
2.2. HREELS Chamber	17
A. Chamber Description and Crystal Mounting	
B. Gas Dosing	
2.3. Crystal Cleaning Procedure	20
2.4. Sn/Pt(111) Alloy Formation	21
2.5. Description of Experimental Techniques	22
A. Auger Electron Spectroscopy (AES)	
B. X-ray Photoelectron Spectroscopy (XPS)	
C. Low Energy Electron Diffraction (LEED)	
D. Temperature-Programmed Desorption (TPD)	
E. Molecular Beam Kinetics Experiments	
2.6. Construction of a Simple Molecular Beam	27
2.6.1. Description of the New Molecular Beam	27
2.6.2. Alignment and Testing	30
2.7. References	33
VII. Chapter 3: Adsorption and Reaction of Pyridine on Pt(111)	
3.0 Abstract	35
3.1. Introduction	35

3.2. Experimental Methods	41
3.3. Results and Discussion	42
3.4. Conclusion	51
3.5. References	53
VIII. Chapter 4: Adsorption and Reaction of Cyclohexylamine on Pt(111)	
4.0 Abstract	55
4.1. Introduction	55
4.2. Experimental Methods	63
4.3. Results and Discussion	64
4.4. Conclusion	71
4.5. References	72
IX. Chapter 5: Adsorption and Reaction of Piperidine on Pt(111) and Sn/Pt(111) Surface Alloys	
5.0 Abstract	74
5.1. Introduction	74
5.2. Experimental Methods	77
5.3. Results and Discussion	
5.3.1 Piperidine Adsorption on Pt(111)	78
5.3.2 Piperidine Adsorption on Sn/Pt(111) Surface Alloys	86
5.3.3 Comparison of Pyridine, Cyclohexylamine, and Piperidine Adsorption on Pt(111)	88
5.4. Conclusion	91
5.5. References	92
X. Chapter 6: Thermal Stability of Oxide Films Formed by Oxidation of Sn-Pt Surface Alloys Measured by High Resolution X-ray Photoelectron Spectroscopy (HR-XPS)	
6.0 Abstract	94
6.1. Introduction	94
6.2. Experimental Methods	99
6.3. Results and Discussion	100
6.4. Conclusion	105
6.5. References	106
XI. Chapter 7: Summary and Outlook	108
Curriculum Vita	110

## LIST OF TABLES

**Chapter 1**

**Chapter 2**

**Chapter 3**

**Chapter 4**

**Chapter 5**

**Chapter 6**

**Table 6.1** Sn  $3d_{5/2}$  XPS peak positions and full width at half maximum (FWHM) for each spectrum in Figure 6.1.



## LIST OF FIGURES

### Chapter 1

**Figure 1.1** Sn/Pt(111) surface alloys. Top:  $(2\times 2)$ -Sn/Pt(111) Bottom:  $(\sqrt{3}\times\sqrt{3})R30^\circ$ -Sn/Pt(111)

### Chapter 2

**Figure 2.1** (A) Molybdenum sample stub. (B) Side view of the molybdenum sample stub. (C) Top view of the Mo sample stub with the Pt(111) crystal mounted with Ta wires and Mo screws.

**Figure 2.2** Electron beam heater. Top Left: End view of the electron beam heater used for annealing in the Scienta ESCA chamber. Top Right: Side view of the Mo stub in the electron beam heater. The filaments used were Alcatel tungsten #053146, operated at 8 W. Bottom: Top view of the electron beam heater.

**Figure 2.3** Ultrahigh vacuum chamber used for temperature-programmed desorption experiments. (Left) Front view. (Right) Top view of levels 1-3.

**Figure 2.4** Glass test tube used for TPD dosing.

**Figure 2.5**  $(\sqrt{3}\times\sqrt{3})R30^\circ$ -Sn/Pt(111) LEED pattern obtained in the Scienta chamber.

**Figure 2.6** Pt(111)- $(1\times 1)$  LEED pattern obtained in the Scienta chamber.

**Figure 2.7**  $(2\times 2)$ -Sn/Pt(111) LEED pattern obtained in the Scienta chamber.

**Figure 2.8** Effusive molecular beam diagram. This apparatus was equipped with a source chamber and two pumping stages (Stages 1 and 2). Pressures for each of the sections of the beam are labeled  $P_{\text{source}}$ ,  $P_1$ ,  $P_2$ , and  $P_{\text{UHV}}$  for the source chamber, Stage 1, Stage 2, and the UHV chamber, respectively. Gas entered Stage 1 from the source chamber through a TEM grid with a 0.1 mm aperture. Gas entered Stage 2 from Stage 1 through a skimmer with a 0.5 mm diameter orifice. A flag with the capability for vertical movement was positioned in Stage 2. A gate valve was positioned between Stage 2 and the main UHV chamber. Gas entered the UHV chamber from Stage 2 through a collimator with a 3-mm diameter aperture.

**Figure 2.9** Alternate molecular beam diagram. This apparatus was used for preliminary dehydrogenation studies of 1,3-cyclohexadiene on Pt(111).

### Chapter 3

**Figure 3.1** Structure of pyridine

**Figure 3.2** Pyridine TPD after exposures of pyridine on Pt(111) at 100 K of 0.0135, 0.003, and 0.0012 L.

**Figure 3.3** Product TPD after pyridine exposure of 0.0135 L on Pt(111) at 100 K. Pyridine, H<sub>2</sub>, HCN and C<sub>2</sub>N<sub>2</sub> desorption is shown by following 52, 2, 27, and 52 amu, respectively. Pyridine and cyanogen were both followed using 52 amu, but the high-temperature desorption was determined to only be cyanogen by simultaneously monitoring 26 amu, a fragment of cyanogen.

**Figure 3.4** Hydrogen (H<sub>2</sub>) TPD after exposures of pyridine on Pt(111) at 100 K of 0.0135, 0.006, and 0.0012 L.

**Figure 3.5** Hydrogen cyanide (HCN) TPD after exposures of pyridine on Pt(111) at 100 K of 0.0135, 0.003, and 0.0012 L.

**Figure 3.6** Cyanogen (C<sub>2</sub>N<sub>2</sub>) TPD after exposures of pyridine on Pt(111) at 100 K of 0.0135, 0.003, and 0.0012 L. Mass 26 was also monitored (not shown) to identify that this high temperature desorption was due to cyanogen, since pyridine also produces a cracking fraction at 52 amu.

## Chapter 4

**Figure 4.1** Structure of cyclohexylamine

**Figure 4.2** Cyclohexylamine TPD after exposures of cyclohexylamine on Pt(111) at 100 K of 0.324, 0.01125, 0.0072, and 0.0036 L.

**Figure 4.3** Products monitored by TPD after a cyclohexylamine exposure of 0.01125 L on Pt(111) at 100 K. Signals at 56, 2, 27, and 52 amu were monitored for cyclohexylamine, H<sub>2</sub>, HCN, and C<sub>2</sub>N<sub>2</sub>, respectively. The signals for H<sub>2</sub> and HCN were multiplied by 0.01 and 0.1, respectively, to account for the different sensitivity factors used during data acquisition.

**Figure 4.4** H<sub>2</sub> TPD after exposures of cyclohexylamine on Pt(111) at 100 K of 0.324, 0.0081, 0.0036, and 0.0009 L.

**Figure 4.5** HCN TPD after exposures of cyclohexylamine on Pt(111) at 100 K. The signal at 27 amu was monitored for cyclohexylamine exposures of 0.324, 0.01125, and 0.0072 L.

**Figure 4.6** Cyanogen (C<sub>2</sub>N<sub>2</sub>) TPD after exposures of cyclohexylamine on Pt(111) at 100 K. The signal at 52 amu was monitored for cyclohexylamine exposures of 0.01125, 0.0076, and 0.0036 L.

## Chapter 5

**Figure 5.1** Structure of piperidine.

**Figure 5.2** Piperidine TPD after exposures of piperidine on Pt(111) at 100 K of >0.25, 0.0756, 0.012, 0.0066, 0.006, and 0 L.

**Figure 5.3** Product TPD after exposures of piperidine on Pt(111) at 100 K. Desorption of H<sub>2</sub> (2 amu) and HCN (27 amu), was monitored after a piperidine exposure of 0.0168 L. Desorption of piperidine (85 amu), pyridine and C<sub>2</sub>N<sub>2</sub> (both monitored by 52 amu) was monitored after a piperidine exposure of 0.0012 L.

**Figure 5.4** Hydrogen (H<sub>2</sub>) TPD after 0.0432, 0.024, 0.0048, and 0 L exposures of piperidine on Pt(111) at 100 K.

**Figure 5.5** Pyridine TPD after exposures of piperidine on Pt(111) at 100 K of 0.0756, 0.03, 0.012, 0.0066, 0.006, and 0 L.

**Figure 5.6** Hydrogen cyanide (HCN) TPD after exposures of piperidine on Pt(111) at 100 K of 0.0432, 0.024, 0.0168, 0.0048, and 0 L.

**Figure 5.7** Cyanogen (C<sub>2</sub>N<sub>2</sub>) TPD after exposures of piperidine on Pt(111) at 100 K of 0.045, 0.012, 0.0066, and 0.006 L.

Figure 5.8 Piperidine TPD after exposures of piperidine on Pt(111) and Sn/Pt(111) surfaces at 100 K. This figure shows spectra obtained after a low-exposure and a high-exposure dose of piperidine on Pt(111) and Sn/Pt(111) alloy surfaces. Piperidine exposures on Pt(111) were 0.0012 and 0.0756 L, and exposures on the Sn/Pt(111) surface alloy were 0.0135 and 0.09 L.

**Figure 5.9** TPD of monolayer molecular desorption of pyridine, cyclohexylamine, and piperidine from Pt(111).

**Figure 5.10** H<sub>2</sub> TPD after monolayer exposures of pyridine, cyclohexylamine, and piperidine on Pt(111) at 100 K.

## Chapter 6

**Figure 6.1** Sn 3d<sub>5/2</sub> HR-XPS spectra of the ( $\sqrt{3}\times\sqrt{3}$ )R30° Sn/Pt(111) alloy before and after oxidation by NO<sub>2</sub> and thermal reduction: (A) clean  $\sqrt{3}$  alloy; (B)  $\sqrt{3}$  alloy after maximum exposure at 400 K; (C) after thermal reduction of (B) by annealing to 700 K; (D) after thermal reduction of (C) by annealing to 743 K; and (E) after thermal reduction of (D) by annealing to 1000 K.

**Figure 6.2** O 1s spectra of the ( $\sqrt{3}\times\sqrt{3}$ )R30° Sn/Pt(111) alloy before and after oxidation by NO<sub>2</sub> and thermal reduction: (A) clean  $\sqrt{3}$  alloy; (B)  $\sqrt{3}$  alloy after maximum exposure at 400 K; (C) after thermal reduction of (B) by annealing to 700 K; (D) after thermal reduction of (C) by annealing to 743 K; and (E) after thermal reduction of (D) by annealing to 1000 K.

**Figure 6.3** Pt 4f spectra of the ( $\sqrt{3}\times\sqrt{3}$ )R30° Sn/Pt(111) alloy before and after oxidation by NO<sub>2</sub> and thermal reduction: (A) clean  $\sqrt{3}$  alloy; (B)  $\sqrt{3}$  alloy after maximum exposure

at 400 K; (C) after thermal reduction of (B) by annealing to 700 K; (D) after thermal reduction of (C) by annealing to 743 K; and (E) after thermal reduction of (D) by annealing to 1000 K.

## LIST OF ABBREVIATIONS (ALPHABETICAL ORDER)

AES – Auger Electron Spectroscopy

CMA – Cylindrical Mirror Analyzer

DFT – Density Functional Theory

ESCA – Electron Spectroscopy for Chemical Analysis

FYNES – Fluorescence Yield Near Edge Spectroscopy

HDN – Hydrodenitrogenation

HDS – Hydrodesulfurization

HREELS – High Resolution Electron Energy Loss Spectroscopy

HP-PES– High Pressure Photoemission Spectroscopy

HR-XPS – High Resolution X-ray Photoelectron Spectroscopy

LEED – Low Energy Electron Diffraction

QMS – Quadrupole Mass Spectrometer

STM – Scanning Tunneling Microscopy

TEM – Transmission Electron Microscope

TPD – Temperature Programmed Desorption

TSP – Titanium Sublimation Pump

## Abstract

This thesis is based on two projects involving work on Pt(111) and Sn/Pt(111) surface alloys. The first project focused on the adsorption and surface chemistry of pyridine, cyclohexylamine, and piperidine, which were studied on a Pt(111) single crystal in ultrahigh vacuum (UHV) using temperature-programmed desorption (TPD). Piperidine was also studied on Sn/Pt(111) alloy surfaces. Some reversible adsorption was observed for each molecule, though the molecules mainly decomposed on the Pt(111) surface to form hydrogen, H<sub>2</sub>, hydrogen cyanide, HCN, and cyanogen, C<sub>2</sub>N<sub>2</sub>, as desorption products. Activation barriers for C-N bond cleavage are reported.

The second project was a study of the thermal decomposition of metal oxides formed by the oxidation of the ( $\sqrt{3}\times\sqrt{3}$ )R30° Sn/Pt(111) surface with NO<sub>2</sub>, which was studied using high-resolution X-ray photoelectron spectroscopy (HR-XPS). The goal of the HR-XPS work was to determine if NO<sub>2</sub> created an oxide of both Pt and Sn, and to clarify previous results from TPD studies on the oxidized Sn/Pt(111) surface alloys. Nitrogen dioxide, NO<sub>2</sub>, was not found to oxidize Pt; only Sn was oxidized. The Sn oxide underwent thermal decomposition at temperatures as low as 700 K. No oxygen was detected on the alloy surface above 743 K. NO<sub>2</sub> was found to be a weaker oxidizing agent than ozone.

## Chapter 1: Introduction

### 1.1. Use of Pt and PtSn Alloys in Catalysis

Heterogeneous catalysis occurs at the interface of a solid surface and either liquid or gaseous reactants. Platinum is an important catalyst in many industrial processes, yet the expense of this metal has inspired researchers to find ways to use less expensive metals combined with platinum both to reduce cost and improve performance. Specifically, PtSn bimetallic catalysts have been used for catalytic reforming,<sup>1-3</sup> selective hydrogenation<sup>4,5</sup> and dehydrogenation.<sup>6-12</sup> Bimetallic catalysts were first studied back in the 1940s<sup>13</sup>, however the Pt-Sn bimetallic catalyst system appeared in the 1960s and has been extensively researched only in the past few decades. Adding Sn to Pt catalysts has improved activity and selectivity by preventing deactivation from coking and by decreasing the ensemble size of Pt atoms at the catalyst surface.<sup>14</sup> Hydrocracking, or the breakdown of larger hydrocarbons to smaller carbon compounds, causes coking on a catalyst surface. The number of contiguous platinum atoms is reduced in a PtSn alloy, and this hinders the pathway for hydrocracking, which relies on larger platinum ensemble sizes. Studies have also shown that incorporation of Sn with Pt creates electronic effects which enhance catalyst performance. For example, in the selective hydrogenation of  $\alpha,\beta$ -unsaturated aldehydes over supported SnPt catalysts, the presence of both metallic Sn in an alloy phase with Pt and oxidized Sn in contact with the catalyst support play roles in reducing an aldehyde to an unsaturated alcohol.<sup>15</sup> Metallic Sn in the alloy phase with Pt dilutes the Pt atoms and reduces the number of active sites for alkene hydrogenation. By hindering the pathway for alkene hydrogenation, selectivity for the hydrogenation of the carbonyl group is enhanced. Oxidized Sn has been linked to the activation of the carbonyl bond in catalytic hydrogenation.

While industrial research of supported catalysts determines catalyst performance in true reactor conditions (high temperature and pressure), surface science studies on model single-crystal catalysts reveal the fundamental chemistry occurring at the surface without the effects of support materials. These surface studies contribute to catalyst research by determining activation barriers for desorption and reaction, identifying structure-sensitive reactions, and determining adsorption geometries. For example, for face centered cubic (fcc) metals, e.g. platinum, palladium, rhodium, and nickel, three common crystal faces are studied: 100, 111, and 110. Metals with alternate crystal structures, e.g. ruthenium (hexagonal close packed) and molybdenum and tungsten (both body centered cubic), also have common low-index surface planes used in surface science studies. The (111) fcc crystal face has the highest atomic density at the surface compared to (100) and (110), which have more open structures. Surface structure effects have the capacity to affect adsorption geometry of molecules and ultimately change the selectivity of a catalyst.<sup>16</sup> These effects are discussed in specific cases in future chapters.

In addition to structure effects, the activity of a metal for a particular reaction is determined in part by the availability of *d* orbitals for adsorbate bonding. The general trend in the transition metals is that increasing activity is observed from right to left in the *d* block of the periodic table. An analysis of the adsorption of benzene on transition metals reviewed how copper, silver and gold interact weakly with benzene, with molecular desorption at temperatures below 300 K, whereas benzene desorbs near 400 K from metals such as platinum, rhodium, and ruthenium.<sup>17</sup>  $\pi$  electron backdonation from the metal to the adsorbate plays an important role in such unsaturated hydrocarbons, and stronger adsorbate-metal interactions are linked to the likelihood for the molecule to



dissociate on the surface. The strongest interactions occur at low adsorbate coverages, and this can lead to dissociative adsorption and decomposition during heating of the surface at low coverage, while at higher coverages molecular desorption and dissociation can be competitive processes at the surface or completely reversible adsorption can occur.

The role of the metal in such catalytic processes is crucial in the choice of the catalyst. Surface science studies specifically examine the effect on molecular adsorption and reaction of different metals, their surface structures, and their concentration in bimetallic systems. Platinum single crystals have been extensively studied in the Koel group and unsaturated molecules on platinum constitute a large fraction of the group's work. Small alkenes such as ethylene, propylene and butylene have been studied, as well as larger  $\pi$  systems such as benzene, 1,3-cyclohexadiene, n-hexene and 1,5-hexadiene.<sup>18-</sup>  
<sup>26</sup> Platinum is very active in dehydrogenation. Alkane adsorption studies, including n-hexane, butane, isobutane, and cyclohexane, as well as one publication examining bicyclohexane and trans-decahydronaphthalene have shown significant evolution of hydrogen from the surface during TPD due to dehydrogenation.<sup>24,26,27-29</sup>

The surface chemistry of organic molecules with heteroatoms has also been of interest. Acetaldehyde, crotonaldehyde, light alcohols and cyclohexanone have all been studied on Pt surfaces.<sup>30-34</sup> A lesser focus has been on nitrogen-containing compounds.<sup>35</sup> Broadening the information about the interactions between nitrogen-containing hydrocarbons and metals will lead to a better understanding of catalyst function in such processes as hydrotreating. This thesis provides new information regarding the

adsorption and reaction of pyridine, cyclohexylamine and piperidine on Pt(111) and Sn/Pt(111) surfaces.

The oxidation state of a metal alters the chemical reactivity of the surface. Fundamental surface science work on metallic single crystals provides information regarding molecular adsorption and reactions, but “bridging the gap” between a metal single crystal in UHV and a commercial supported heterogeneous catalyst under reaction conditions is incredibly important to make connections between surface science and industrial results. One way to “bridge this gap” is by performing catalysis on single crystal surfaces at higher pressures. Several papers discuss catalytic studies at pressures in the 1-20 Torr range.<sup>31,33,36-38</sup> Another way is to study the formation, stability, and reactivity of oxidized single crystals, since oxidation may occur under more extreme conditions. For example, PtSn/TiO<sub>2</sub> is selective for the hydrogenation of crotonaldehyde to form the desirable product of unsaturated alcohol crotyl alcohol.<sup>39</sup> Crotonaldehyde hydrogenation on the reduced alloyed Sn/Pt(111) surfaces led to formation of the undesirable saturated aldehyde butyraldehyde.<sup>31</sup> This experiment revealed an increased turnover frequency for hydrogenation on the (2×2)Sn/Pt(111) alloy, but alloying did not lead to higher selectivity than Pt, indicating that an oxidized Sn species was responsible for the increased selectivity of the bimetallic catalyst.

Use of DFT calculations and vibrational studies have led to a better understanding of how molecules with electronegative heteroatoms bond to metal surfaces.<sup>34,40-44</sup> For example, cyclohexanone bonds to Pt(111) via the oxygen atom and the adsorption geometry is such that the molecular ring is tilted upward from the surface.<sup>34</sup> On Sn/Pt(111), cyclohexanone bonds more weakly and the oxygen atom bonds preferentially

to surface Sn atoms instead of to Pt atoms. An increase of the surface Sn concentration from 0.25 to 0.33 monolayers weakens the adsorption strength. Also, on the ordered Sn/Pt(111) surface alloys, the influence of ensemble size on reactions has been reported.<sup>24</sup> Strong chemisorption of olefinic molecules requires adjacent Pt atoms, and the addition of Sn has an important site-blocking component in its influence on the adsorption of unsaturated molecules.

Research on the chemistry of ordered Sn/Pt(111) alloy surfaces in the Koel group included many hydrocarbon and organic molecules, but also included a number of surface oxidation studies.<sup>45-52</sup> These surface oxidation studies investigated the formation and thermal stability of platinum and tin oxides formed from the use of ozone, nitrogen dioxide and dioxygen. Other researchers have also studied surface oxidation by the use of oxygen plasma sources and oxygen atom dosers.<sup>53,54</sup> This literature is discussed in Chapter 6, and is the basis for the high resolution X-ray photoelectron spectroscopy (HR-XPS) study in this thesis.

Previous unpublished work by Saliba in the Koel group identified an oxidic phase with a thermal stability intermediate to platinum and tin oxides. The unidentified oxide species was created by oxidation of a Sn/Pt(111) surface alloy with ozone. In addition to identifying this oxide species, a need for HR-XPS analysis of the surface alloys after oxidation by NO<sub>2</sub> existed because previous XPS data was obtained using lower resolution than that available at the Scienta facility at Lehigh University. The HR-XPS work presented in this thesis details the thermal stability of a ( $\sqrt{3}\times\sqrt{3}$ )R30°-Sn/Pt(111) surface oxidized by NO<sub>2</sub>. Oxidation of the surface by exposure to NO<sub>2</sub> does not produce the unidentified oxide species that was found on the ozone-treated surface. Tin oxide, but

not platinum oxide, was formed in this study. The thermal decomposition of the Sn oxide is presented in a series of spectra obtained with the Scienta ESCA 300. This work confirms the presumption from earlier publications: NO<sub>2</sub> does not form platinum oxide when oxidizing the PtSn surface alloy on a Pt single crystal.

Formation of two PtSn ordered surface alloys on a Pt(111) single crystal was initially characterized by Windham and Paffett, who obtained the surface alloys by vapor deposition of Sn on Pt(111) followed by annealing.<sup>55</sup> Both the Pt<sub>2</sub>Sn and Pt<sub>3</sub>Sn crystal faces, with one-third and one-fourth of a monolayer of Sn, respectively, were observed by low-energy electron diffraction (LEED). Additional structural studies of the PtSn surface alloys have also been reported.<sup>56,57</sup> These model systems have aided in understanding industrial alloy catalysts by allowing for the measurement of adsorption energies and by performing catalysis in the absence of oxidized Sn species and oxide support interactions.

## 1.2 Definitions Used in Sn/Pt(111) Studies

The Sn/Pt(111) surface alloys were formed by vapor deposition of Sn onto a Pt(111) single crystal followed by annealing to create two ordered surfaces, the (2×2)-Sn/Pt(111) and ( $\sqrt{3}\times\sqrt{3}$ )R30°-Sn/Pt(111) surfaces (Figure 1.1). Reactions on these ordered surfaces have been extensively studied by the Koel group, as detailed previously, and the research presented within this thesis is based on these surfaces, which will be referred to from here forward as the 2×2 and the  $\sqrt{3}$  surfaces, which contain 0.25 monolayers (ML) and 0.33 ML Sn, respectively. One monolayer, 1.0 ML, is defined as the density of atoms on the Pt(111) surface and is  $1.505 \times 10^{15}$  atoms/cm<sup>2</sup>. This thesis will present work on these two surface alloys in two different aspects. First, adsorption and reaction of nitrogen-containing molecules on Pt(111) and PtSn surface alloys using

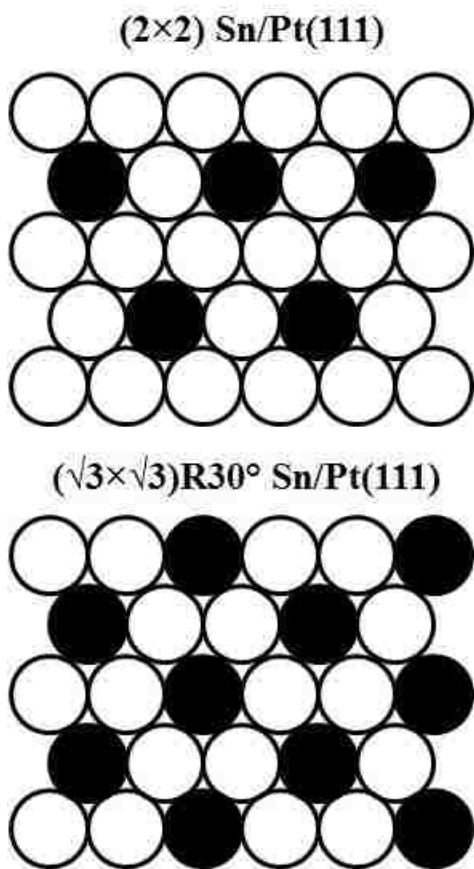


**Figure 1.1** Sn/Pt(111) surface alloys. Top: (2×2)-Sn/Pt(111)  
Bottom: (√3×√3)R30°-Sn/Pt(111)

temperature-programmed desorption (TPD) will be presented. Three molecules were studied: pyridine, cyclohexylamine, and piperidine. Secondly HR-XPS was used to study the oxidation of the  $\sqrt{3}$  alloy surface with  $\text{NO}_2$ .

### 1.3 Motivation for Current Work

A recent study has shown that a supported PtSn bimetallic catalyst has both higher selectivity and activity than the commercial NiMo/ $\text{Al}_2\text{O}_3$  catalyst in hydrodesulfurization (HDS) and hydrodenitrogenation (HDN) processes.<sup>58</sup> Hydrodenitrogenation was studied for carbazole over PtSn/ $\text{SiO}_2$ , PtSn/ $\text{Al}_2\text{O}_3$ , and NiMo/ $\text{Al}_2\text{O}_3$ . A PtSn/ $\text{SiO}_2$  catalyst had similar conversion and slightly higher HDN activity than the commercial

catalyst. Both PtSn/ $\text{SiO}_2$  and NiMo/ $\text{Al}_2\text{O}_3$  had significantly better performance in conversion and HDN of carbazole compared to PtSn/ $\text{Al}_2\text{O}_3$ . These results are of particular interest to our group because the PtSn catalysts supported on silica exhibit more alloyed phases than on alumina supports.<sup>59,60</sup> Sn/Pt(111) surface alloys could be used to understand the chemistry of nitrogen-containing cyclic hydrocarbons to determine what role alloying has on the reaction of these molecules. Some information is available regarding the interaction of nitrogen-containing cyclic hydrocarbons on Pt single crystal surfaces,<sup>61-70</sup> but at the time that this thesis was written, no information from PtSn

surface studies was available. By studying the interaction of pyridine, cyclohexylamine and piperidine on Pt(111), the activity of the surface was determined in the absence of Sn. Then, piperidine was adsorbed on the PtSn surface alloys to determine the effect of Sn on surface reactions.

Another purpose of the work presented here is to investigate the influence of the nitrogen atom environment on the adsorption and reaction of a series of related molecules on a Pt(111) surface. Pyridine ( $C_5H_5N$ ), cyclohexylamine ( $C_6H_{11}NH_2$ ), and piperidine ( $C_5H_{10}NH$ ) adsorption and reaction on Pt(111) were studied by TPD. This technique utilizes a mass spectrometer in line-of-sight with the crystal to detect desorption products as the sample is warmed by a steady heating rate. In addition, preliminary data on the reaction of piperidine on the Sn/Pt(111) surface alloys show that Sn weakens the interaction of this molecule with the surface.

Motivation for the HR-XPS research on the thermal stability of oxides formed from oxidation of the  $\sqrt{3}$  alloy by  $NO_2$  stems from the desire to determine if this oxidation technique is efficient enough to form both Pt and Sn oxides. Saliba, a former student in the Koel group, studied the oxidation of the PtSn surface alloys with ozone in several TPD experiments.<sup>71</sup> While ordered surface alloys have been created on both Pt(111) and Pt(100), for the purpose of this thesis, only ordered surface alloys on Pt(111) are reviewed here. Her work discovered that oxidation of the surface alloys by ozone created oxides which were less thermally stable than Sn oxide. It was suggested that alloying Sn with Pt affected the thermal stability of Sn oxide and decomposition by thermal reduction required less energy. Supported catalysts often have metals with multiple oxidation states, and the thermal stability of metal oxides in catalysts is

important to understand because these materials are regularly exposed to both high temperature and pressure in industrial catalysis settings. Work in this thesis reports the identity of oxides present during the thermal reduction of the  $\sqrt{3}$  PtSn surface alloy after oxidation by NO<sub>2</sub>. Previous studies reported the use of NO<sub>2</sub> doses at 400 K to deposit oxygen atoms on single crystal surfaces.<sup>72-75</sup> This method is detailed later in Chapter 6. HR-XPS data was obtained in conjunction with step-wise heating to monitor the stability of metal oxides.

#### 1.4. References

1. Gonzalez-Marcos, M. P.; Inarra, B.; Guil, J. M.; Gutierrez-Ortiz, M. A. *Appl. Catal. , A* **2004**, *273*, 259-268.
2. Mal, N. K.; Sasidharan, M.; Matsukata, M.; Sivasanker, S.; Ramaswamy, A. V. *Stud. Surf. Sci. Catal.* **2004**, *154C*, 2403-2410.
3. Vilella, I. M.; Borbath, I.; Margitfalvi, J. L.; Lazar, K.; de, M., S. R.; Scelza, O. A. *Appl. Catal. , A* **2007**, *326*, 37-47.
4. Merlo, A. B.; Machado, B. F.; Vetere, V.; Faria, J. L.; Casella, M. L. *Appl. Catal. , A* **2010**, *383*, 43-49.
5. Plomp, A. J.; van, A., D. M. P.; van, der Eerden, A. M. J.; Maeki-Arvela, P.; Murzin, D. Y.; de, J., K. P.; Bitter, J. H. *J. Catal.* **2009**, *263*, 146-154.
6. Bocanegra, S. A.; de, M., Sergio R.; Borbath, I.; Margitfalvi, J. L.; Scelza, O. A. *J. Mol. Catal. A: Chem.* **2009**, *301*, 52-60.
7. He, S.; Sun, C.; Bai, Z.; Dai, X.; Wang, B. *Appl. Catal. , A* **2009**, *356*, 88-98.
8. Santhosh, K., M.; Chen, D.; Holmen, A.; Walmsley, J. C. *Catal. Today* **2009**, *142*, 17-23.
9. Nawaz, Z.; Tang, X.; Zhang, Q.; Wang, D.; Fei, W. *Catal. Commun.* **2009**, *10*, 1925-1930.
10. Bocanegra, S.; Ballarini, A.; Zgolicz, P.; Scelza, O.; de, M., S. *Catal. Today* **2009**, *143*, 334-340.

11. Zhang, Y.; Zhou, Y.; Qiu, A.; Wang, Y.; Xu, Y.; Wu, P. *Catal. Commun.* **2006**, *7*, 860-866.
12. Kogan, S. B.; Herskowitz, M. *React. Kinet. Catal. Lett.* **2005**, *85*, 341-345.
13. Ertl, G.; Knozinger, H.; Schuth, F.; Weitkamp, J., Eds.; In *Handbook of Heterogeneous Catalysis*; Wiley: Weinheim, 2008; Vol. 3.
14. Arteaga, G. J.; Anderson, J. A.; Rochester, C. H. *J. Catal.* **1999**, *184*, 268-279.
15. Ramallo-Lopez, J. M.; Santori, G. F.; Giovanetti, L.; Casella, M. L.; Ferretti, O. A.; Requejo, F. G. *J Phys Chem B* **2003**, *107*, 11441-11451.
16. Kolasinski, K. W. In *Surface Science: Foundations of Catalysis and Nanoscience*; John Wiley & Sons Ltd.: New York, 2002.
17. Netzer, F.P.; *Langmuir* **1991**, *7*, 2544-2547.
18. Zhao, H.; Koel, B.E.; *Surf. Sci.* **2004**, *572*, 261-268
19. Zhao, H.; Koel, B.E.; *J. Catal.* **2005**, *234*, 24-32.
20. Windham, R.G.; Bartram, M.E.; Koel, B.E.; *J. Phys. Chem.* **1988**, *92*, 2861-2870.
21. Paffett, M.T.; Gebhard, S.C.; Windham, R.G.; Koel, B.E.; *Surf. Sci.* **1989**, *223*, 449-464.
22. Tsai, Y.-L.; Koel, B.E. *J. Phys. Chem. B* **1997**, *101*, 2895-2906
23. Tsai, Y.-L.; Xu, C.; Koel, B.E.; *Surf. Sci.* **1997**, *385*, 37-59.
24. Zhao, H.; Koel, B.E.; *J. Phys. Chem.* **2009**, *113*, 18152-18162.
25. Peck, J.W.; Koel, B.E.; *J. Am. Chem. Soc.* **1996**, *118*, 2708-2717.
26. Xu, C.; Tsai, Y.-L.; Koel, B.E.; *J. Phys. Chem.* **1994**, *98*, 585-593.
27. Carter, E.A.; Koel, B.E.; *J. Molec. Catal. A* **1998**, *101*, 2895-2906.
28. Xu, C.; Koel, B.E.; Paffett, M.T.; *Langmuir* **1994**, *10*, 166-171.
29. Zhao, H.; Koel, B.E.; *Surf. Sci.* **2004**, *573*, 413-425.
30. Zhao, H.; Kim, J.; Koel, B.E.; *Surf. Sci.* **2003**, *538*, 147-159.
31. Jerdev, D.; Olivas, A.; Koel, B.E.; *J. Catal.* **2002**, *205*, 278-288.



32. Panja, C.; Saliba, N.; Koel, B.E.; *Surf. Sci.* **1998**, *395*, 248-259.
33. Olivas, A.; Jerdev, D.I.; Koel, B.E.; *J. Catal.* **2004**, *222*, 285-292.
34. Kim, J.; Welch, L.A.; Olivas, A.; Podkolzin, S.G.; Koel, B.E.; *Langmuir* **2010**, *26*, 16401-16411.
35. Peck, J.W.; Mahon, D.I.; Beck, D.E.; Koel, B.E.; *Surf. Sci.* **1998**, *410*, 170-188.
36. Bertolini, J.C.; Cassuto, A.; Jugnet, Y.; Massardier, J.; Tardy, B.; Tourillon, G.; *Surf. Sci.* **1996**, *349*, 88-96.
37. Bratlie, K.M.; Flores, L.D.; Somorjai, G.A.; *Surf. Sci.* **2005**, *599*, 93-106.
38. Huang, S.X.; Gland, J.L.; *J. Phys. Chem.* **1996**, *100*, 2206-2212.
39. Huidobro, A.; Sepulveda-Escribano, A.; Rodriguez-Reinoso, F.; *J. Catal.* **2002**, *212*, 94-103.
40. Haubrich, J.; Loffreda, D.; Delbecq, F.; Sautet, P.; Jugnet, Y.; Becker, C.; Wandelt, K. *J. Phys. Chem. C* **2010**, *114*, 1073-1084.
41. Vigne, F.; Haubrich, J.; Loffreda, D.; Sautet, P.; Delbecq, F. *J. Catal.* **2010**, *275*, 129-139.
42. Haubrich, J.; Loffreda, D.; Delbecq, F.; Sautet, P.; Krupski, A.; Becker, C.; Wandelt, K. *J. Phys. Chem. C* **2009**, *113*, 13947-13967.
43. Haubrich, J.; Loffreda, D.; Delbecq, F.; Sautet, P.; Jugnet, Y.; Krupski, A.; Becker, C.; Wandelt, K. *J. Phys. Chem. C* **2008**, *112*, 3701-3718.
44. Haubrich, J.; Loffreda, D.; Delbecq, F.; Jugnet, Y.; Sautet, P.; Krupski, A.; Becker, C.; Wandelt, K. *Chem. Phys. Lett.* **2006**, *433*, 188-192.
45. Jerdev, D. I.; Koel, B. E. *Surf. Sci.* **2001**, *492*, 106-114.
46. Saliba, N. A.; Tsai, Y. L.; Koel, B. E. *J. Phys. Chem. B* **1999**, *103*, 1532-1541.
47. Voss, M. R.; Zhao, H.; Koel, B. E. *Surf. Sci.* **2004**, *560*, 235-245.
48. Batzill, M.; Kim, J.; Beck, D. E.; Koel, B. E. *Phys. Rev. B* **2004**, *69*, 165403-165414.
49. Batzill, M.; Beck, D. E.; Koel, B. E. *Phys. Rev. B* **2001**, *64*, 245402-245412.
50. Parker, D. H.; Koel, B. E. *J. Vac. Sci. Technol. A* **1990**, *8*, 2585-2590.

51. Bartram, M. E.; Windham, R. G.; Koel, B. E. *Surf. Sci.* **1987**, *184*, 57-74.
52. Saliba, N. A.; Tsai, Y. L.; Panja, C.; Koel, B. E. *Surf. Sci.* **1999**, *419*, 79-88.
53. Weaver, J. F.; Chen, J. J.; Gerrard, A. L. *Surf. Sci.* **2005**, *592*, 83-103.
54. Shumbera, R. B.; Kan, H. H.; Weaver, J. F. *Surf. Sci.* **2007**, *601*, 235-246.
55. Paffett, M. T.; Windham, R. G. *Surf. Sci.* **1989**, *208*, 34-54.
56. Overbury, S.H.; Mullins, D.R.; Paffett, M.T.; Koel, B.E.; *Surf. Sci.* **1991**, *254*, 45-57.
57. Overbury, S.H.; Ku, Y.; *Phys. Rev. B*, **1992**, *46*, 7868-7872.
58. Lewandowski, M.; Sarbak, Z. *Appl. Catal. , B* **2008**, *79*, 313-322.
59. Meitzner, G.; Via, G.H.; Lytle, F.W.; Fung, S.C.; Sinfelt, J.H.; *J. Phys. Chem.* **1988**, *92*, 2925-2932.
60. Li, Y.-X.; Klabunde, J.; Davis, B.H.; *J. Catal.* **1991**, *128*, 1-12.
61. Haq, S.; King, D. A. *J. Phys. Chem.* **1996**, *100*, 16957-16965.
62. Grassian, V.H.; Muetterties, E.L.; *J. Phys. Chem.* **1986**, *90*, 5900-5907.
63. Johnson, A.L.; Muetterties, E.L.; Stöhr, J.; Sette, F.; *J. Phys. Chem.* **1985**, *89*, 4071-4075.
64. Lee, I.C.; Masel, R.I.; *J. Phys. Chem. B* **2002**, *106*, 368-373.
65. Gland, J.L.; Somorjai, G.A.; *Surf. Sci.* **1973**, *38*, 157-186.
66. Kliewer, C. J.; Somorjai, G. A. *Catal. Lett.* **2010**, *137*, 118-122.
67. Surman, M.; Bare, S.R.; Hofmann, P.; King, D.A.; *Surf. Sci.* **1987**, *179*, 243-253.
68. Connolly, M.; Somers, J.; Bridge, M.E.; Lloyd, D.R.; *Surf. Sci.* **1987**, *185*, 559-568.
69. Gland, J.L.; Somorjai, G.A.; *Adv. Coll. Interf. Sci.* **1976**, *5*, 205-243.
70. Huang, S.X.; Fischer, D.A.; Gland, J.L.; *J. Vac. Sci. Technol. A* **1994**, *12*, 2164-2169.
71. Saliba, N.; unpublished work.
72. Saliba, N. A.; Tsai, Y. L.; Panja, C.; Koel, B. E. *Surf. Sci.* **1999**, *419*, 79-88.
73. Weaver, J. F.; Chen, J. J.; Gerrard, A. L. *Surf. Sci.* **2005**, *592*, 83-103.
74. Shumbera, R. B.; Kan, H. H.; Weaver, J. F. *Surf. Sci.* **2007**, *601*, 235-246.
75. Parkinson, C. R.; Walker, M.; McConville, C. F.; *Surf. Sci.* **2003**, *545*, 19-33.

## Chapter 2: Experimental Methods

### 2.1 Scienta ESCA 300

High resolution XPS (HR-XPS) data for those studies of the thermal decomposition of metal oxides were obtained using the Scienta ESCA 300 facility at Lehigh University. This facility uses a monochromatic Al K $\alpha$  X-ray source from a rotating anode. X-ray power can be as high as 7.5 kW. The hemispherical analyzer is 300 mm in diameter. Data from the Scienta facility were taken in the analysis chamber with the sample stub seated on a stage capable of 360° rotation and movement on 5 axes, sample heating to ~875 K, as well as the ability to automate data collection for angle-resolved studies. The analysis chamber is equipped with an ion gun for Ar<sup>+</sup> sputtering.

A Pt(111) single crystal was mounted on a specially-made Mo stub, as seen in Figure 2.1. Molybdenum was chosen for the stub material due to its high thermal



**Figure 2.1** (A) Molybdenum sample stub. (B) Side view of the molybdenum sample stub. (C) Top view of the Mo sample stub with the Pt(111) crystal mounted with Ta wires and Mo screws.

stability. This stub had tapped holes for 0.256” Mo screws. The stub had three different notches for the manipulator forks. The surface of the stub was polished by using 600, 1500, and then 3  $\mu$ m-grit sand paper. The crystal was affixed to the stub by applied pressure from two 0.020” tungsten wires that were pressed tightly to the stub surface with Mo screws.

The preparation chamber in the Scienta facility is equipped with an electron beam heater designed in part by Dr. Mauricio Valencia Ramos.

Figure 2.2 shows a schematic diagram of the electron beam heater. This heater was specially made to function with the stub described above and has the capability to heat

the stub and crystal to 1200 K. This heater was able to reach the temperatures necessary to anneal the single crystal and obtain an ordered surface using 3 V, 8 A on the filament and 450 V bias on the stub and crystal. The electron beam heater (mounted in the preparation chamber) is separate from the sample stage heater (in the analysis chamber). Annealing to order the crystal can only be accomplished by using the high temperature capabilities of the electron beam heater in the preparation chamber. During heating, the

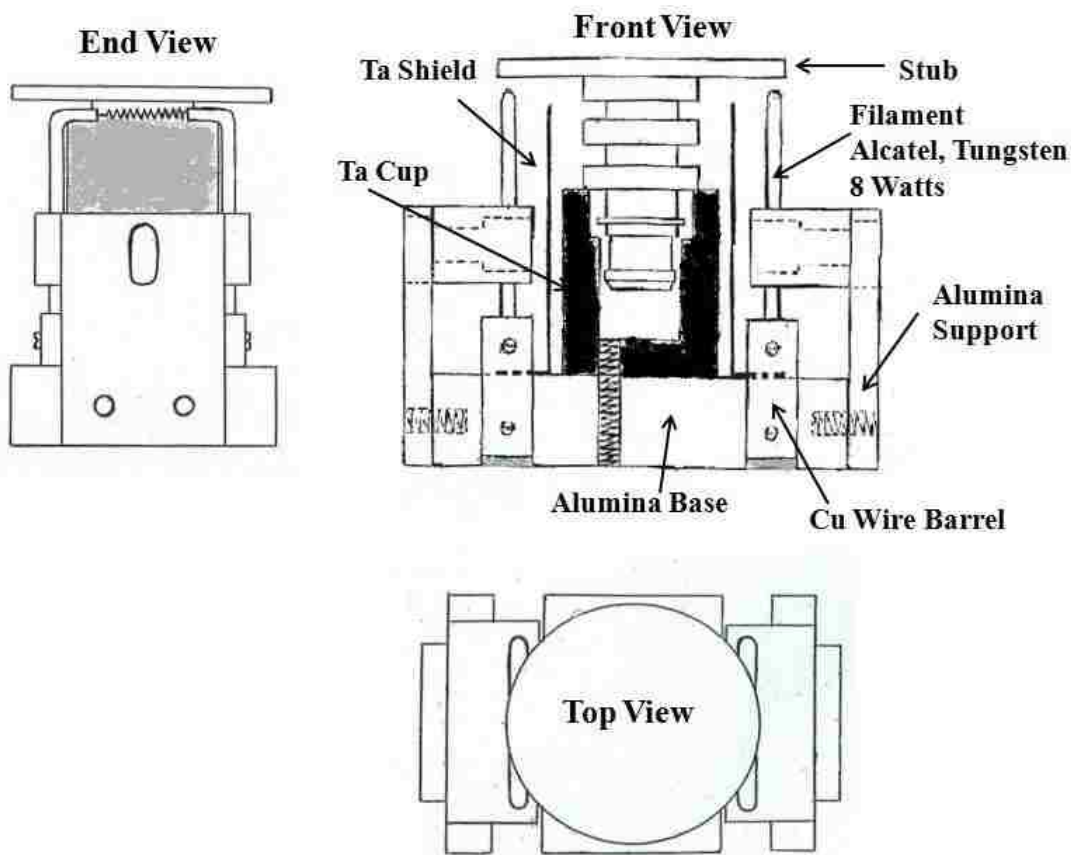


**Figure 2.2** Electron beam heater. Top Left: End view of the electron beam heater used for annealing in the Scienta ESCA chamber. Top Right: Side view of the Mo stub in the electron beam heater. The filaments used were Alcatel tungsten #053146, operated at 8 W. Bottom: Top view of the electron beam heater.

crystal temperature was monitored by a pyrometer (Pulsar, model E<sub>2</sub>T). The emissivity was adjustable between 0.1 and 1.0. The pyrometer accuracy was checked by

monitoring a crystal with an attached thermocouple. The pyrometer had the capability to read temperatures between 600 and 1700 K with an accuracy of  $\pm 5$  K. The ordered surface was verified in the preparation chamber with the low-energy electron diffraction (LEED) optics. The manipulator fork in the preparation chamber is able to rotate  $360^\circ$  and has some ability to tilt. To use the LEED optics in the preparation chamber of the Scienta facility, the crystal on the stub must be rotated to face the LEED optics and then a C-clamp was tightened on the bellows to tilt the manipulator downward so that the crystal was in front of the LEED screen.

A Sn doser was also within the preparation chamber. This doser was constructed with a 2  $\frac{3}{4}$ " Conflat™ flange with 2- $\frac{1}{8}$  in. copper feedthroughs. Two 1/16-in. dia. stainless steel welding rods were cut and bent into "L" shapes and affixed to the Cu feedthroughs. A Mo bowl purchased through ESPI was filled with two pieces of 1/4-in. dia. Sn shot (6N purity, ESPI) and then sealed by spot-welding a Ta sheet on top of the bowl. The Ta lid for the bowl was pierced one time to allow for Sn evaporation out of the doser via a 1.5 mm dia. pinhole. The sealed bowl was spot-welded to the two stainless steel "L" rods with thin Ta strips. The Sn doser was then mounted on a Conflat™ flange at the base of the preparation chamber so that the doser protruded into the chamber vertically. The crystal inverted on the manipulator fork was within  $\sim 1.5$ " of the doser pinhole. The manipulator fork needed to be in the lowest notch of the stub for the crystal to be at its closest distance to the doser. The Sn doser was resistively heated with a DC power supply at 3 V, 21 A to evaporate Sn onto the crystal surface at a convenient rate (0.005 monolayers/sec).

Oxidation of the Sn/Pt(111) surfaces was performed using a leak valve on the analysis chamber. Attached to this leak valve is a retractable 1/4"-diameter stainless steel tube to provide directed doses of NO<sub>2</sub> to the surface. This tube was able to be moved close enough to touch the crystal surface, and dosing was carried out with the tube at a distance of less than 1 cm. Stainless steel tubing connected the leak valve to the fast entry chamber for pumping. All connections along this line of tubing were made with either stainless steel or Au-plated gaskets to minimize the decomposition of NO<sub>2</sub> due to interactions with Cu gaskets. The tubing was evacuated via the fast entry chamber turbomolecular pump, and then baked at 400 K for 1.5 hours. The NO<sub>2</sub> gas was backfilled into the stainless steel tubing freshly for each dose. After the crystal was heated to 400 K, NO<sub>2</sub> was dosed onto the surface. This procedure relies on the fact that desorption of NO occurs below 400 K, so upon dosing NO<sub>2</sub>, NO desorbs and leaves atomic oxygen on the surface. More details regarding this procedure are discussed in Chapter 6.<sup>1</sup>

## 2.2 HREELS Chamber

Temperature programmed desorption (TPD) experiments were performed in a 3-level ultrahigh vacuum (UHV) chamber, Figure 2.3, with base pressures in the 10<sup>-10</sup> Torr range. The top level of the chamber contained a dual Mg K $\alpha$  and Al K $\alpha$  anode X-ray source and a double-pass cylindrical mirror analyzer (CMA) for Auger electron spectroscopy (AES) and XPS. Also in the top level was an ion gun for Ar<sup>+</sup> ion sputtering. Argon ion sputtering was performed by backfilling the chamber with 3 $\times$ 10<sup>-5</sup> Torr Ar. The ion gun was used at a 1.0-keV beam energy with a 25-mA emission current, and the ion gun was defocused to achieve uniform sputtering. The second level

contained a reverse-view LEED optics and a quadrupole mass spectrometer (QMS). The third level contained a high-resolution electron energy loss spectrometer (HREELS). The UHV chamber was equipped with a rotary-vane oil pump, 240 liter/s turbomolecular pump, 400 liter/s ion pump, and a titanium sublimation pump (TSP).

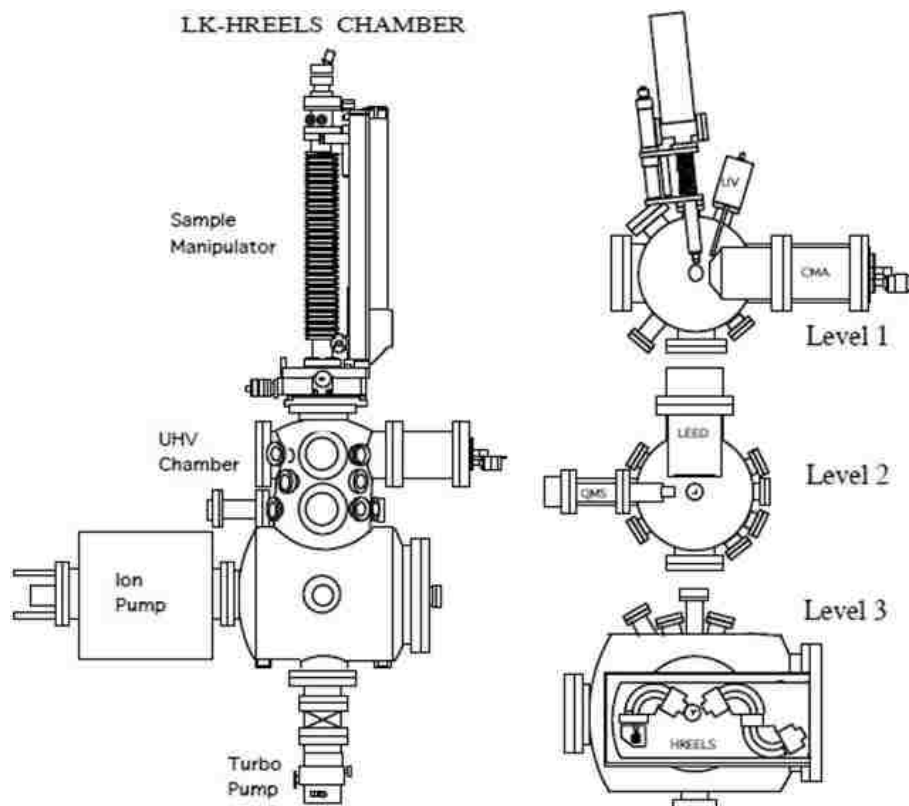


**Figure 2.3** Ultrahigh vacuum chamber used for temperature-programmed desorption experiments. (Left) Front view. (Right) Top view of levels 1-3.

The sample manipulator is capable of 360° rotation and movement on three axes.

A Pt(111) single crystal (1-cm diameter) was mounted in the chamber between two tantalum rods and 0.020" Ta wire spot-welded to the sides of the crystal. A 0.005" K-type (chromel-alumel) thermocouple was spot-welded to the side of the crystal for temperature measurement. The crystal could be resistively heated to 1200 K and cooled

with liquid nitrogen to below 90 K. Leak valves were strategically placed for gas dosing and a Sn doser was located between the first and second levels.

Gas dosing for TPD experiments was performed by constructing a stainless steel gas handling line using VCR™ fittings with several Nupro™ valves and leak valves. One leak valve was used for the introduction of oxygen into the chamber for surface cleaning. The doser for molecules studied in TPD experiments consisted of a leak valve equipped with a 1/8" diameter stainless steel tube with an open end protruding into the chamber to within 2 cm of the crystal face. On the outside of the UHV chamber, the leak valve was connected to a tee, with one connection leading to a 1/4" stainless steel tubing



**Figure 2.4** Glass test tube used for TPD dosing.

with a glass test tube attached via an Ultratorr™ fitting and the other end connected to a rotary vane pump. This test tube was similar to the model CG-960 Chem-Vac with Chem-cap (High Vacuum 90°, 1-arm) available through ChemGlass. The test tube was adapted to have a 1/4" glass tube sidearm. The valve was made of Teflon and a suitable replacement plug is model CG-961 (with no o-ring), which is available through ChemGlass.

The specialized glass test tube (Figure 2.4) had a valve at the top and a 1/4" glass tube arm that fits in an Ultratorr™ or Swagelok connector. Stainless steel gaskets were used to connect VCR® fittings in the reagent dosing line to prevent reactions between the chemicals and Cu gaskets. Each liquid chemical reagent in the test tube underwent freeze-pump-thaw cycles, where the



liquid was frozen in the test tube with liquid nitrogen and the gases above the frozen chemical evacuated by pumping. Then the liquid was thawed and the cycle was repeated a minimum of three times. This procedure removed dissolved gases from the reagents. Molecular sieves were used to remove water for all TPD reagents except pyridine.

Gas dosing on the Pt(111) crystal was measured with the ion gauge, and exposures are reported in units of Langmuir ( $1 \text{ L} = 1 \times 10^{-6} \text{ Torr}\cdot\text{sec}$ ). These exposures are reported without corrections for ion gauge sensitivities. Molecules were dosed on the Pt(111) surface, which was cooled to  $< 100 \text{ K}$  with liquid nitrogen. TPD experiments were performed with the crystal positioned in line-of-sight with the QMS and less than 2 mm from the mouth of the QMS. The QMS was fitted with a nozzle with a circular opening, which is smaller than the 1 cm diameter of the single crystal and limited desorption products entering the QMS to molecules desorbing mainly from the front of the crystal, and so that contributions of products from the sides and back of the crystal were limited.

### 2.3 Crystal-Cleaning Procedure

The Pt(111) crystal was cleaned by  $\text{Ar}^+$  ion sputtering to remove surface contamination. The crystal was annealed to 850 K in  $1 \times 10^{-6} \text{ Torr O}_2$  for 2 min. to remove carbonaceous material from the surface when less than one monolayer of carbon contamination was present. After that, the crystal surface was annealed to 1200 K in UHV for 30 sec and an ordered surface was verified by LEED (Figure 2.5). Following each TPD experiment on Pt(111), sputtering was unnecessary and only annealing in  $\text{O}_2$  was needed to remove surface contaminants. The clean surface was verified by AES.

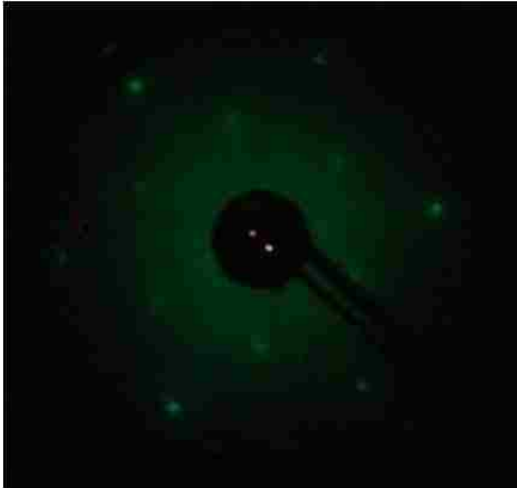


**Figure 2.5**  $(\sqrt{3} \times \sqrt{3})R30^\circ$ -Sn/Pt(111) LEED pattern obtained in the Scienta chamber.

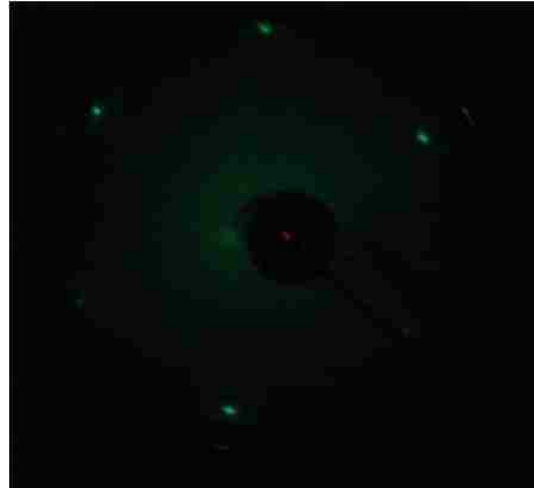


**Figure 2.6** Pt(111)- $(1 \times 1)$  LEED pattern obtained in the Scienta chamber.

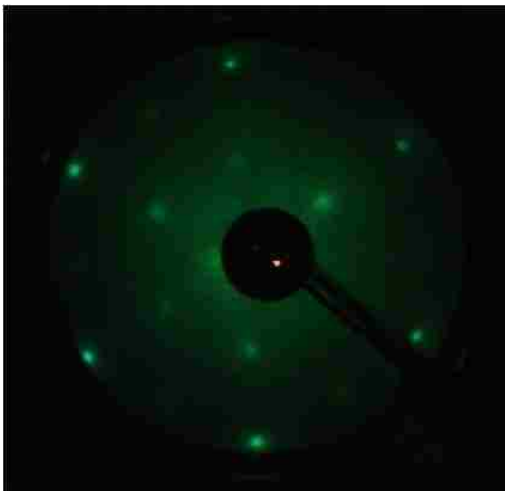


**Figure 2.7**  $(2 \times 2)$ -Sn/Pt(111) LEED pattern obtained in the Scienta chamber.

#### 2.4 Sn/Pt(111) Alloy Formation

The ordered Sn/Pt(111) surface alloys were formed by vapor deposition of Sn onto a clean Pt(111) surface. After preparation of a clean Pt(111) surface, approximately 1 monolayer (ML) of Sn was evaporated onto the surface, as monitored by AES in the HREELS chamber and XPS in the Scienta chamber. One monolayer is defined as the density of atoms on

the Pt(111) surface and is  $1.505 \times 10^{15}$  atoms/cm<sup>2</sup>. Previous studies have determined the AES signal ratio for Sn:Pt corresponding to 1 ML of Sn.<sup>2</sup> For the HR-XPS work, the XPS signal ratio for Sn:Pt corresponding to 1 ML of Sn was based on earlier unpublished work by Xiaofang Yang. Following deposition of 1 ML of Sn onto the surface, the crystal was annealed to 770 and 820 K for 20 s to form the  $(\sqrt{3} \times \sqrt{3})R30^\circ$  Sn/Pt(111) and  $(2 \times 2)$  Sn/Pt(111) ordered alloy surfaces, respectively. These ordered surfaces were

verified by LEED, and images of these LEED patterns are shown in Figures 2.6 and 2.7, respectively. Each experiment on these surface alloys was followed by sputtering the surface clean and annealing to regenerate the clean Pt(111) surface and freshly forming the surface alloy again.

## 2.5 Surface Science Techniques

Auger electron spectroscopy (AES) is a technique in which incident electrons of 3 to 5 keV energy, directed at the sample surface by an electron gun, cause a core-level electron to be ionized.<sup>3</sup> The resulting hole is then filled by an electron from an outer shell relaxing to fill the core level. No radiation is emitted in this step, so the energy from this relaxation causes a second electron to be emitted, the Auger electron. From the kinetic energy of the Auger electron, the elemental surface composition can be determined. A typical AES spectrum shows the derivative of the energy distribution function,  $dN(E)/dE$ , versus kinetic energy. The Auger electron kinetic energy (KE) is a unique function of the separation of energy levels of the atom from which it was released.<sup>4</sup> In this work, a double-pass CMA equipped with an internal electron gun was used to obtain AES spectra. Excluding hydrogen and helium, AES can detect all other elements.<sup>3-5</sup> The depth sensitivity for AES is limited to the top several atomic layers, 0 – 10 nm for transitions of 0 – 2 keV KE.<sup>5</sup> Inelastic electron scattering prevents the emission of characteristic electrons from atoms deeper in the sample surface.

X-ray photoelectron spectroscopy (XPS) is a technique in which soft X-rays are directed at a sample surface, which cause core shell electrons to be ionized. These photoelectrons that are emitted from the surface atoms escape into an analyzer with their original kinetic energy, which is characteristic of the ionized atom. The kinetic energy of

the electrons determined by the analyzer is usually converted to a binding energy by subtracting it from the photon energy and then used to determine the elemental surface composition. The energy of the incident photon is equal to the sum of the kinetic energy of the photoelectron emitted from the surface, the binding energy of that core electron, and the work function,  $\Phi$ . The work function is a measure of the energy needed for the electron to leave the surface and enter vacuum. Photoelectrons detected by the analyzer typically come from the first 1-10 nm of the surface region, just as in AES, for kinetic energies of 0 –1.5 keV, and collecting electrons from low take-off angles (the angle between the surface and the analyzer) enhances surface sensitivity because photoelectrons away from the surface are less likely to escape from the sample.

Low-energy electron diffraction (LEED) is a technique used to characterize ordered surface structures. The instrument is composed of an electron gun directed at the sample surface, a phosphor screen, and grids biased so that only elastically scattered electrons are detected.<sup>6</sup> This is a surface sensitive technique and structural information on only atoms in the top one to three layers is obtained when using 50-150 eV electrons. When the sample surface has long-range ordering, the electrons diffracted back from the surface and onto the phosphor screen in the LEED instrument reveal an ordered spot pattern. This pattern relates to the orientation and size of the surface unit cell. When a surface is disordered, LEED spots may be weak and broad or may not appear at all. This technique is helpful in experiments performed on single crystal surfaces to determine the cleanliness of the sample as well as to detect the specific ordering of the Sn/Pt(111) surface alloys formed by vapor deposition. This technique is also used to detect ordered patterns of adsorbates on surfaces.<sup>7</sup>

Temperature programmed desorption (TPD) is a technique frequently used in surface science studies to determine reaction products desorbing from the surface into the gas phase.<sup>8</sup> The technique utilizes a mass spectrometer to monitor desorption products and a thermocouple to monitor the surface temperature. After condensing a reactant molecule on the surface of a sample, in this work cooled to below 100 K by liquid nitrogen, the sample is positioned in line-of-sight of the mass spectrometer. The surface is then warmed with a controlled, linear heating ramp, while both temperature and mass spectrometer signals are simultaneously recorded. The resulting data are plotted in a figure showing the QMS signal versus temperature. From the peak desorption temperatures of products, desorption activation barriers can be calculated using Redhead analysis,<sup>9</sup> as shown in Equation 1. This provides the relationship between the desorption activation energy ( $E$ ), desorption peak temperature ( $T_p$ ), heating rate ( $\beta$ ), gas constant ( $R$ ), and the preexponential factor,  $\nu_1$ , assumed to be  $1 \times 10^{13} \text{ s}^{-1}$ . The error associated with the relationship between  $E/RT_p$  is  $\pm 1.5$  percent for values of  $\nu/\beta$  between  $10^8$  and  $10^{13} \text{ K}^{-1}$ .<sup>9</sup> Peak shapes observed in TPD spectra can indicate the kinetics of desorption. For example, first order desorption occurs with a TPD curve asymmetric about the desorption peak temperature that does not shift with coverage, while second order desorption occurs with a TPD peak more symmetric about the desorption peak temperature and shifts strongly with coverage at low coverages. The information from a combination of TPD, electron spectroscopy, and vibrational techniques can provide insight into how reactions occur on surfaces.

$$\frac{E}{RT_p} = \ln \frac{\nu_1 T_p}{\beta} - 3.64 \quad (1)$$

Temperature programmed desorption data were obtained using the LabView software, version 8.5, from National Instruments. A program was written by Dr. Xiaofang Yang to enable monitoring of temperature, time, and mass spectrometer signal. An interface box was connected between the computer and the UTI 100C quadrupole mass spectrometer. The UTI 100C can detect masses between 0-300 amu, and in addition, the electronics has sensitivity switching capability between  $10^{-5}$ - $10^{-11}$  Torr partial pressures. The temperature was monitored directly by the thermocouple spot-welded on the side of the crystal. The temperature reported in the TPD data was altered to match room temperature, which was obtained when the crystal had not been affected by heating or cooling overnight. This assumed that the temperature in the vacuum chamber was the same as room temperature, which is a reasonable assumption because the temperature in the laboratory typically did not change significantly from day to day.

Broad scans of mass spectra as well as TPD spectra using discreet mass peaks were obtained using LabView software. The TPD spectra were obtained after calibration involving setting known peaks to correspond to the masses measured in a program while obtaining broad scan mass spectra. After recording a broad scan (0-100 amu) mass spectrum, up to 8 masses could be chosen to be monitored simultaneously by the TPD software. Placing a marker on the center of a mass peak in the mass spectrum selected that mass for the TPD program. After up to 8 masses were selected, the sensitivity for each mass was chosen. Other parameters in the TPD program included a dwell time (ms) and a wait time (ms). The dwell time was the time per mass that the spectrometer spent collecting signal, and the wait time referred to the amount of time the spectrometer allowed between recording signal from a mass after switching sensitivity and

spectrometer voltage. The dwell and wait times were optimized to allow for the quickest scan without observing “cross-talk” between masses. Cross-talk occurs when an insufficient time for switching between masses caused remnant or ghost signals to appear from the previous mass in the next mass signal. Because more than 8 masses were monitored for each of the molecules studied in this TPD work, numerous scans were necessary to search for possible products and molecular cracking fractions. TPD experiments were repeated to obtain data from several different exposures (coverages) of the dosed molecule.

Molecular beam experiments are used in surface science to determine the kinetics of reactions on surfaces as well as the sticking probability of molecules. Kinetics experiments are performed by directing a molecular beam at a substrate in UHV while monitoring gas-phase products via mass spectrometry. In our experiments, the mass spectrometer was positioned out of line-of-sight of the crystal sample so that the molecules being detected were from the background gases in the UHV chamber. Sticking probability measurements can be performed by directing the molecular beam at the crystal sample, which is initially blocked by a mechanical flag, and then moving the mechanical flag from in front of the crystal so that the molecular beam directly impinges on the crystal. The molecular beam is ideally smaller in diameter than the crystal so that all molecules in the beam hit the crystal. The sticking coefficient is calculated from the ratio of the number of the beam molecules sticking (i.e., adsorbing) on the surface compared to the number of molecules that hit the surface. The sticking coefficient is affected by the adsorbate coverage on the crystal, with the initial sticking coefficient calculated when the surface is clean.

## 2.6 Construction of a Simple Molecular Beam

Constructing a simple, cheap but efficient effusive molecular beam apparatus presents a number of challenges. One design has been proposed by Bowker's group.<sup>10,11</sup> In addition to Bowker, other groups involved in molecular beam research include the Zaera Mullins groups.<sup>12-19</sup> One significant challenge that was encountered while attempting to construct such a source was the alignment of the beam apertures, which consisted of a glass capillary with an approximate inner diameter of 2  $\mu\text{m}$ , a stainless steel skimmer with diameter of 300  $\mu\text{m}$ , and a glass final collimator with an inner diameter of approximately 2.33 mm at the exit. Alignment of these three components was difficult, so a new design was desired. A new molecular beam was designed and built to replace the previous version in the Koel group.

### 2.6.1 Description of the New Molecular Beam

The new design was composed of all stainless steel parts. Figure 2.8 shows a diagram of the molecular beam. There was an initial aperture that was mounted in a replaceable cap screwed onto the end of a 3/8" diameter stretch of tubing. The final collimator was a 3 mm aperture on the end of a length of 3/8" tubing. Both the tubes for the initial aperture and the final collimator were welded onto 2 3/4" stainless steel Conflat<sup>TM</sup> double-sided flanges. The beam was mounted on the side of a UHV chamber equipped with capability for HREELS and XPS, and a QMS for use in the beam experiments. There were a series of differentially pumped stages in the beamline. The source chamber was comprised of a series of VCR fittings that could be evacuated with a mechanical pump. The source gas or liquid (in a test tube, as described above) was connected to the VCR<sup>®</sup> fitting through



an UltraTorr™ connection. Pressure measurement in the source chamber was provided by a MKS Baratron® gauge with a range of 0-10 Torr.

The Conflat™ double-sided flange with the initial aperture was mounted between the source chamber and Stage 1. This initial aperture was a gold-plated copper TEM grid with a 3-mm diameter and a centered 100- $\mu$ m hole. This grid was mounted in a replaceable cap made of stainless steel. The cap screwed onto the end of a threaded tube mounted on the Conflat™ double-sided flange. The proximity of the initial aperture to the skimmer could be adjusted along three axes. Stage 1 was the differentially pumped space between the initial aperture and the skimmer. This stage was pumped by a 170 L/s turbomolecular pump. Pressure was monitored via an ion gauge. The Conflat™ double-sided flange on which the skimmer was mounted was connected between Stage 1 and Stage 2. The skimmer was obtained commercially (Model 2, 0.5-mm orifice, nickel; Beam Dynamics, Inc). The skimmer was cone-shaped with steep edges and a knife-edge orifice. Care was taken to protect the knife edges of the skimmer entrance because it is very delicate. The skimmer was not touched with bare hands, and it was handled only using clean tweezers with special consideration to prevent bending or denting the delicate, thin material.

Stage 2 consisted of the area in the beamline between the skimmer and the final collimator. This stage had a flag which could be moved vertically in and out of the beam. The area was differentially pumped by a 230 L/s turbomolecular pump closely coupled to the stage. Pressure was monitored via an ion gauge. Within Stage 2, a metal-sealed valve separated the beamline from the main chamber, so that when the beamline was not in use or needed to be altered, the main chamber could be used without interruption by

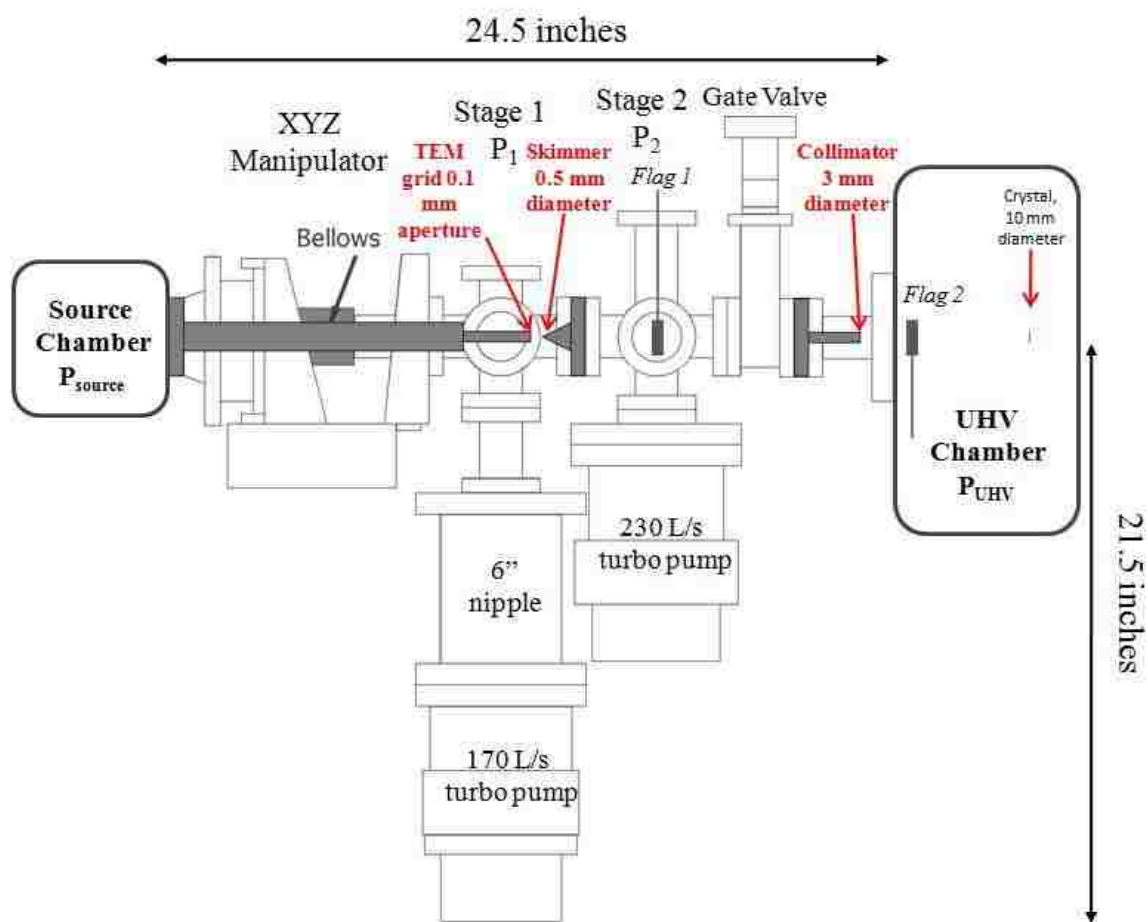


**Figure 2.8** Effusive molecular beam diagram. This apparatus was equipped with a source chamber and two pumping stages (Stages 1 and 2). Pressures for each of the sections of the beam are labeled  $P_{\text{source}}$ ,  $P_1$ ,  $P_2$ , and  $P_{\text{UHV}}$  for the source chamber, Stage 1, Stage 2, and the UHV chamber, respectively. Gas entered Stage 1 from the source chamber through a TEM grid with a 0.1 mm aperture. Gas entered Stage 2 from Stage 1 through a skimmer with a 0.5 mm diameter orifice. A flag with the capability for vertical movement was positioned in Stage 2. A gate valve was positioned between Stage 2 and the main UHV chamber. Gas entered the UHV chamber from Stage 2 through a collimator with a 3-mm diameter aperture.

venting. The final collimator was sandwiched between the UHV valve and the main chamber, so that the collimator protruded into the main chamber. The final collimator had a 3 mm aperture within a replaceable cap at the end protruding into the main

chamber. The aperture could be changed to be smaller if necessary. The crystal was positioned 7 inches from the exit of the collimator.

An alteration to the final aperture in the beam was the replacement of the 3 mm aperture on the protruding tube to a small stainless steel aperture which was machined to screw into a solid Cu gasket mounted between the main chamber and Stage 2. The stainless steel piece is able to be exchanged to change the final aperture diameter.

A rotatable flag inside the UHV chamber was mounted on a flange adjacent to the flange where the molecular beam was mounted. This rotatable flag could be moved in and out of the beam to block the crystal from intercepting the molecular beam directly. The flag was constructed from a rectangular piece of stainless steel shim stock that was spot welded onto a thin, stainless steel rod. The rod was bent in a manner so that the flag could easily be rotated into the beam path and also be kept away from the other instruments in the main chamber when not in use.

### 2.6.2 Alignment and Testing

The beam apertures were aligned while the molecular beam was on the bench prior to the beam being mounted on the main chamber. A surveyor's scope was used to center the initial 100- $\mu\text{m}$  aperture with the skimmer orifice. The scope was placed facing the exit side of the skimmer, and a light was shone through the initial source tube. The skimmer aperture was then similarly aligned with the collimator aperture. By altering the focal point on the scope, each aperture was brought into focus and centered on the crosshairs of the scope.

To test the beam performance, the crystal was placed in front of the collimator at the end of the beam. The crystal was cooled to approximately 90 K with liquid nitrogen.

While using the flag within the chamber to block the beam from being intercepted by the crystal, approximately 2 Torr of a mixture of hexanes was leaked into the source chamber. The QMS in the main chamber monitored the cracking fraction at 43 amu as the molecules entered the chamber. The hexanes were chosen because it was a solvent readily available in the laboratory. The signal at 43 amu was followed because a large portion of the hexanes was composed of methylpentane isomers, all of which have a large fragmentation peak at 43 amu. Fragmentation occurs in a mass spectrometer due to molecules being broken apart during ionization. When the flag was moved to allow the beam to be intercepted by the crystal, the QMS signal dropped approximately 5-10%, and the signal increased when the flag was placed back in the beam-blocking position. The signal did not rise while the crystal was in front of the beam because the crystal was cooled with liquid nitrogen, and so the adsorption and condensation of hexanes continued until the crystal was blocked by a flag.

Moving the crystal did not improve the amount of the beam that directly impinged on the crystal. The conclusion was that the beam was too broad with too much background gas interfering with the beam. Possible strategies to reduce the beam size would be to exchange the final collimator aperture for a smaller, perhaps 2-mm aperture, or to add a second skimmer to the beam line.

If a future student were to continue this project, several steps can be taken to improve the performance of the current beam. First, the pumping speed of the consecutive stages must be significantly increased by installing pumps with speeds of 400 L/s to enhance the evacuation of background pressure in each stage. This was determined by adding a second turbo pump on the second stage, which resulted in a clear

increase in the beam signal to background ratio. Any method to decrease the pressure in all of the stages would greatly enhance the beam performance. Second, the alignment of the beam could be improved by adding an additional skimmer. The current construction includes an initial aperture, one commercial skimmer and a final aperture. Phone conversations with Prof. C. Buddie Mullins, who leads a group performing successful beam studies at the University of Texas at Austin, were helpful in identifying flaws in the current and past constructions, and he was a helpful source of information on this topic.

Preliminary results using an alternate molecular beam design (Figure 2.9), which was described in a previous publication<sup>20</sup>, were presented in a poster at the 2010 New York Metropolitan Catalysis Society Spring Symposium. This apparatus was constructed

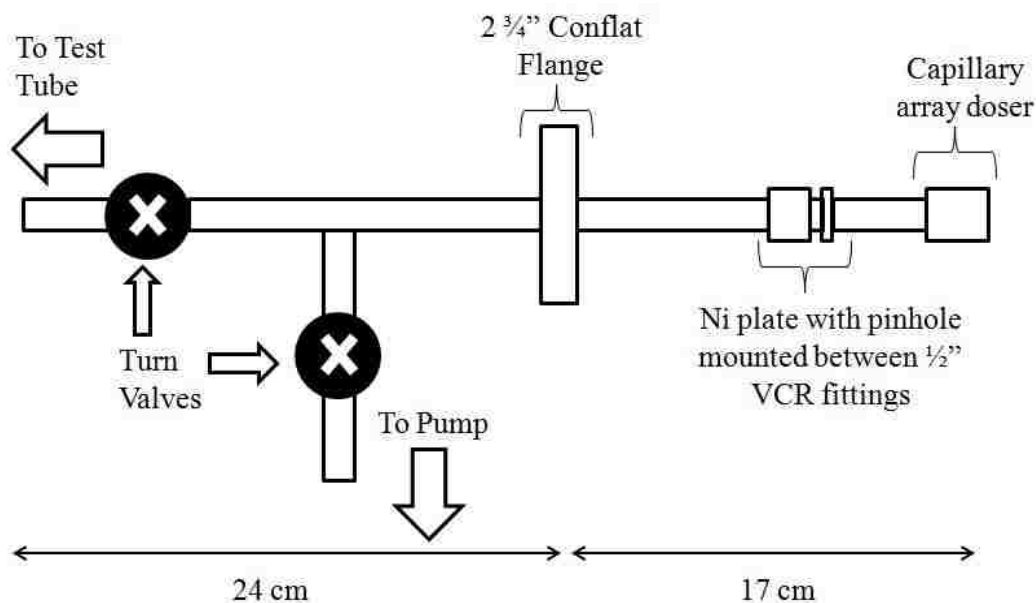


**Figure 2.9** Alternate molecular beam diagram. This apparatus was used for preliminary dehydrogenation studies of 1,3-cyclohexadiene on Pt(111).

of stainless steel tubing welded to a 2 3/4" Conflat<sup>TM</sup> flange. On the vacuum side of the flange, a VCR connection held a nickel plate with a pinhole through which dosing

molecules flow. A microcapillary array doser was connected to the end of the vacuum side of the apparatus. Outside the chamber, there was a stainless steel tee. One side of the tee led to a mechanical pump, while the other side was connected to the source gas test tube. The dehydrogenation of 1,3-cyclohexadiene to benzene over a Pt(111) surface was monitored with this beam apparatus. The QMS signal for benzene increased simultaneously with hydrogen when the crystal was exposed to 1,3-cyclohexadiene. Further work was not pursued because the beam efficiency was not optimal for taking data.

## 2.7 References

1. Bartram, M. E.; Windham, R. G.; Koel, B. E. *Surf. Sci.* **1987**, *184*, 57-74.
2. Zhao, H. Doctoral thesis, **2004**.
3. Kolasinski, K. W. In *Surface Science: Foundations of Catalysis and Nanoscience*; John Wiley & Sons Ltd.: New York, 2002; 64-66.
4. Somorjai, G. A. In *Introduction to Surface Science and Catalysis*; John Wiley & Sons, Inc.: New York, 1994; 389-390.
5. Settle, F., Ed.; In *Handbook of Instrumental Techniques for Analytical Chemistry* Prentice Hall: New York, 1997; 794.
6. Kolasinski, K. W. In *Surface Science: Foundations of Catalysis and Nanoscience*; John Wiley & Sons Ltd.: New York, 2002; 45-52.
7. Paffett, M. T.; Gebhard, S. C.; Windham, R. G.; Koel, B. E. *J. Phys. Chem.* **1990**, *94*, 6831-6839.
8. Adamson, A.W.; Gast, A.P.; *Physical Chemistry of Surfaces*; John Wiley & Sons, Inc.: New York, 1997; 696-698.
9. Redhead, P. *Vacuum* **1962**, *12*, 203-211.
10. Bowker, M. *Appl. Catal.*, *A* **1997**, *160*, 89-98.

11. Bowker, M.; Pudney, P. D. A.; Barnes, C. J. *J. Vac. Sci. Technol. A* **1990**, *8*, 816-820.
12. Bowker, M.; Holroyd, R.; Perkins, N.; Bhantoo, J.; Counsell, J.; Carley, A.; Morgan, C.; *Surf. Sci.*, **2007**, 3651-3660.
13. Bowker, M.; Morgan, C.; Zhdanov, V.P.; *Phys. Chem. Chem. Phys.*, **2007**, *9*, 5700-5703.
14. Wilson, J.; Guo, H.; Morales, R.; Podgorov, E.; Lee, I.; Zaera, F.; *Phys. Chem. Chem. Phys.*, **2007**, *9*, 3830-3852.
15. Unac, R.O.; Bustos, V.; Wilson, J.; Zgrablich, G.; Zaera, F.; *J. Chem. Phys.* **2006**, *125*, 074705-074713.
16. Gong, J.; Mullins, C.B.; *Acc. Chem. Res.*, **2009**, *42*, 1063-1073.
17. Yan, T.; Gong, J.; Flaherty, D.W.; Mullins, C.B.; *J. Phys. Chem. C*, **2011**, *115*, 2057-2065.
18. Yan, T.; Gong, J.; Mullins, C.B.; *J. Am. Chem. Soc.*, **2009**, *131*, 16189-16194.
19. Pan, M.; Hoang, S.; Mullins, C.B.; *Catal. Today*, **2011**, *160*, 198-203.
20. Jiang, L. Q.; Koel, B. E. *J. Phys. Chem.* **1992**, *96*, 8694-8697.

## Chapter 3: Adsorption and Reaction of Pyridine on Pt(111)

### 3.0 Abstract

Adsorption and reaction of pyridine on a Pt(111) surface was studied by temperature programmed desorption (TPD). Molecular desorption was observed from the multilayer and monolayer at 168 K and 247 K, respectively. Pyridine molecules that did not desorb molecularly decomposed to form products which subsequently desorbed, including hydrogen ( $H_2$ ), hydrogen cyanide (HCN), cyanogen ( $C_2N_2$ ), and ammonia ( $NH_3$ ). A thorough analysis of the decomposition of adsorbed pyridine on Pt(111) contributes supporting information to previous vibrational studies and less-detailed thermal desorption studies of nitrogen-containing cyclic molecules, namely pyridine. This chapter describes the adsorption and reaction of pyridine on Pt(111), and an analysis of the current knowledge regarding the adsorption and reaction of nitrogen-containing molecules on metal surfaces is provided. Cleavage of the C-N bond in the pyridine ring is reported to occur with an activation barrier between 21 and 26 kcal/mol. Subsequent chapters make comparisons of the adsorption of two similar molecules, cyclohexylamine and piperidine, to pyridine on Pt(111).

### 3.1 Introduction

In the oil refining industry, crude oil undergoes a hydrotreating process, which removes nitrogen and sulfur prior to the catalytic processes that yield marketable products.<sup>1</sup> The hydrotreating process is a combination of hydrodesulfurization (HDS) and hydrodenitrogenation (HDN) and is important because combustion of hydrocarbon fuels retaining sulfur and nitrogen will form toxic exhaust components, i.e. sulfur and nitrogen oxides.<sup>1</sup> In addition, sulfur has been cited as a poison for platinum catalysts used in catalytic converters, and nitrogen-containing molecules bond more strongly to metal catalysts than hydrocarbons, so removal of nitrogen is necessary to limit catalyst deactivation due to high occupation of active sites during petroleum processing.<sup>1</sup> Commercial hydrotreating catalysts are commonly composed of bimetallic materials such as NiMo/Al<sub>2</sub>O<sub>3</sub><sup>2,4</sup> and CoMo/Al<sub>2</sub>O<sub>3</sub><sup>4</sup>, however a recent publication has shown that a platinum-tin bimetallic catalyst yields both higher activity and conversion for HDS and HDN compared to a commercial NiMo/Al<sub>2</sub>O<sub>3</sub> catalyst.<sup>2</sup> In this study, HDN of carbazole



was compared over PtSn/SiO<sub>2</sub>, PtSn/Al<sub>2</sub>O<sub>3</sub>, and NiMo/Al<sub>2</sub>O<sub>3</sub>. A PtSn/SiO<sub>2</sub> catalyst had similar conversion and higher HDN activity than the commercial catalyst. Both PtSn/SiO<sub>2</sub> and NiMo/Al<sub>2</sub>O<sub>3</sub> had significantly better performance in conversion and HDN of carbazole compared to PtSn/Al<sub>2</sub>O<sub>3</sub>, which was most active for hydrogenation. These results are of particular interest to us because PtSn catalysts supported on silica exhibit a larger concentration of alloyed phases than on alumina supports.<sup>2</sup> Thus, Sn/Pt(111) surface alloys might be useful for understanding the chemistry of nitrogen-containing cyclic hydrocarbons and determining what role alloy composition and structure has on the reaction of these molecules. While the expense of platinum, a precious metal, may deter industrial chemists from using a Pt hydrotreating catalyst, it is important to understand why a platinum catalyst performs slightly better than the commercial nickel-molybdenum catalyst.

A recent review of HDN reported that supported monometallic platinum catalysts, especially sulfided platinum, exhibited higher activity than current commercial catalysts, which are generally bimetallic combinations of nickel, molybdenum, tungsten, and cobalt.<sup>1</sup> Frequently sulfided catalysts are used to enhance activity for particular reactions (e.g. sulfidation of a CoMo/Al<sub>2</sub>O<sub>3</sub> showed higher activity for hydrogenolysis of nitrogen ring compounds and sulfidation of NiMo/Al<sub>2</sub>O<sub>3</sub> showed higher activity for hydrogenation).<sup>1</sup> Both hydrogenation and hydrogenolysis are necessary reactions in the hydrotreating process. References within a 2005 HDN review<sup>1</sup> discuss the superior performance of supported platinum catalysts compared to typical commercial catalysts. Sulfided platinum supported on carbon demonstrated a ten-fold greater HDN activity than Ni(Co)Mo/Al<sub>2</sub>O<sub>3</sub>.<sup>4</sup> Gamma-alumina supported platinum was compared to other

noble metals supported on  $\gamma$ -Al<sub>2</sub>O<sub>3</sub> for the hydrogenolysis of indole, a nitrogen-containing cyclic molecule.<sup>1</sup> Sulfided Pt/ $\gamma$ -Al<sub>2</sub>O<sub>3</sub> showed the highest activity of all noble metals tested. Platinum and iridium sulfides show more selectivity for HDN than HDS<sup>4</sup>, and while noble metals typically act as promoters for HDN, the activity of NiW/Al<sub>2</sub>O<sub>3</sub> was not enhanced by addition of Pt, Ru, or Ir.<sup>4</sup>

Certain supported bimetallic platinum catalysts, e.g. PtSn/SiO<sub>2</sub>,<sup>2</sup> and Pd-Pt supported on amorphous silica-alumina,<sup>5</sup> show simultaneous selectivity for HDN and HDS with activity superior to commercial catalysts composed of combinations of Ni, Co, W and Mo. Fundamental studies of the effect of metals on the reaction of nitrogen-containing molecules are needed to explain the differences in activity between catalytic materials. Further research is also needed to understand the effect of supports on HDN.

Catalytic studies provide data regarding the activity, selectivity, and stability of catalysts, but surface science studies provide information regarding the fundamental



**Figure 3.1**  
Structure of  
pyridine

surface chemistry behind the catalytic performance. By studying the adsorption and reaction pathways for nitrogen-containing hydrocarbons on single crystals, researchers have determined how molecules decompose on metal surfaces, as well as the activation barriers associated with reaction, decomposition and desorption. Specifically, pyridine (Figure 3.1) has been studied on Pt(111), Pt(100) and Pt(110) surfaces using thermal desorption and vibrational spectroscopies.<sup>6-13</sup> In addition, pyridine adsorption and reaction was monitored on Ni, Mo, Ag, Cu, Ir, Pd, Rh, W, and Ru single crystal surfaces.<sup>14-28</sup>

Pyridine adsorption studies have identified the geometry of pyridine adsorbed on metal surfaces. On Pt(111), pyridine adsorbs molecularly with the ring parallel to the surface at low coverage and low temperature.<sup>6</sup> Both increasing the temperature and coverage causes the molecule to tilt upward and bond via the lone pair of electrons on the nitrogen atom. Pyridine bonds via the electronegative nitrogen atom when the surface coverage is increased, and this is consistent with oxygen-containing molecule adsorption studies. For example, cyclohexanone and crotonaldehyde bond via the electronegative oxygen atom on Pt(111).<sup>29-31</sup>

Adsorption of pyridine on Pt(100) during hydrogenation at a H<sub>2</sub> pressure of 100 Torr and pyridine pressure of 10 Torr is nearly vertical until the surface is warmed to 350 K, where pyridine adopts a geometry with the ring parallel to the surface.<sup>11</sup> The disappearance of an aromatic C-H stretch at 3050 cm<sup>-1</sup> was evidence for this transition. Adsorption of pyridine on Pt(110) is similar to Pt(100). At low coverage, pyridine's ring is parallel to the surface and it shifts to bond upright via the nitrogen atom at high coverage.<sup>9,12</sup>

On Pt(100), pyridine is suggested to form an  $\alpha$ -pyridyl intermediate on the surface after the dehydrogenation of a ring carbon in the alpha position.<sup>10,12</sup> An  $\alpha$ -pyridyl intermediate formed on Pt(100) at 300 K after the alpha hydrogen was released between 120 and 300 K. The  $\alpha$ -pyridyl species bonds via a di- $\sigma$  bond between the lone pair of electrons on the nitrogen atom and the  $\alpha$ -carbon. This  $\alpha$ -pyridyl species has been confirmed by several Pt surface studies and it has also been observed on several other metal surfaces.<sup>7,9-11,13</sup> Formation of the  $\alpha$ -pyridyl species occurs after warming the Pt(111) surface to near 300 K. The  $\alpha$ -pyridyl species decomposes at higher temperatures.

After the surface is warmed to 350 K, the characteristic vibrational peaks of the adsorbed species are no longer detected and this process corresponds with the subsequent desorption of additional dihydrogen.<sup>11</sup> The desorption of H<sub>2</sub> near 350-370 K is indicative of dehydrogenation of only the  $\alpha$ -carbon. Desorption of H<sub>2</sub> at 350-370 K is assigned to a desorption-limited process where adsorbed hydrogen atoms recombine to desorb as molecular hydrogen. Thermal desorption studies on Pt(111) have determined that desorption of H<sub>2</sub> in a peak at approximately 350 K corresponds to the loss of only one hydrogen atom from pyridine.<sup>7,13</sup>

Multilayer desorption of pyridine was reported to occur at 190 K, and desorption of pyridine from the monolayer occurred at 347 K.<sup>7</sup> The monolayer desorption peak shifts to lower temperatures, down to 260 K, with increasing exposures. A higher-temperature peak at 473 K was assigned to the desorption of pyridine after the  $\alpha$ -pyridyl intermediate and an adsorbed hydrogen atom recombine.<sup>7</sup> After warming a Pt(111) surface to 400 K, nearly all vibrational modes disappeared due to extensive decomposition of surface species.<sup>10</sup>

The coverage-dependent adsorption geometry observed for pyridine on Pt(111) was also seen on other metal surfaces: Ni(111)<sup>14,15</sup>, Ni(110)<sup>16</sup>, Ni(100)<sup>17</sup>, Ni(001)<sup>18</sup>, Mo(110)<sup>19</sup>, Ni/MoS<sub>x</sub><sup>20</sup>, Ag(110)<sup>21</sup>, Cu(111)<sup>22,23</sup>, Cu(110)<sup>6</sup>, Ir(111)<sup>24</sup>, Pd(111)<sup>25</sup>, Rh(111)<sup>26</sup>, W(110)<sup>27</sup>, and Ru(001)<sup>28</sup>. On Ni(111), the molecular plane of pyridine was oriented at approximately 20° with respect to the surface normal, and the N-Ni bond was determined to be coplanar with the molecular ring.<sup>14</sup> A coverage-dependent adsorption geometry was observed on the Ni(110) surface, which is similar to the adsorption on

platinum surfaces, and it was noted that at room temperature no decomposition of pyridine was detected by high-resolution electron energy loss spectroscopy (HREELS).<sup>16</sup>

On Mo(110), pyridine demonstrated a temperature-dependent adsorption geometry similar to other metals.<sup>19</sup> An  $\eta^1$ -pyridine structure bonded via the nitrogen lone pair of electrons was assigned to the low temperature desorption peak of pyridine at  $375\pm 5$  K. Pyridine molecules adopting an  $\eta^6$ -pyridine geometry desorbed at a higher temperature, 440-530 K, which was dependent on coverage. From both TPD experiments and calculations using density functional theory (DFT), there is evidence that an  $\alpha$ -pyridyl species formed from the  $\eta^6$ -pyridine adsorption geometry, but not from the  $\eta^1$ -pyridine species.

A coverage-dependent adsorption geometry was also observed on Rh(111), Ag(110), Ru(001), Pd(111), Cu(111) and Cu(110). On these surfaces, pyridine adsorbed with the molecular ring parallel to the surface at low coverage, and the molecule tilted upward at higher coverages. Some metal surfaces are much more reactive than others. On Rh(111), HCN and H<sub>2</sub> formed as thermal decomposition products after adsorption of pyridine.<sup>26</sup> On Ru(001), pyridine formed HCN, H<sub>2</sub>, and N<sub>2</sub> after exposures of pyridine causing a near-saturation coverage.<sup>28</sup> The  $\alpha$ -pyridyl species observed on Ni and Pt surfaces was also observed on Ir(111)<sup>24</sup> and Ru(001)<sup>28</sup>, but this reaction intermediate was not observed on Ag, Pd, Cu, or W surfaces<sup>21-23,6,25,27</sup>. From a review of pyridine adsorption studies on these metals, one observes that metals bonding strongly to pyridine cause bond activation. Ni, Mo, Pt, Ir, and Ru all interact with pyridine strongly enough to cause bonds to break and the  $\alpha$ -pyridyl species was observed on these surfaces.

While previous work has focused on the clarification of the adsorbed surface geometry and thermal stability of molecular pyridine on platinum and other metal surfaces, a thorough analysis of the complete decomposition of pyridine has not been reported. Previous thermal decomposition studies have only reported the desorption spectra of molecular pyridine and dihydrogen. The goal of the project described in this chapter was to provide supporting information on the complete thermal decomposition of pyridine on Pt(111). The following analysis reports temperature-programmed desorption (TPD) data of pyridine and decomposition products including dihydrogen, hydrogen cyanide, and cyanogen. Detailed comparisons of the formation of these products to previous literature explain kinetics and thermodynamics behind pyridine adsorption and reaction. This analysis will be helpful in understanding the chemistry of platinum in HDN catalysts.

### 3.2 Experimental Methods

Gas dosing of pyridine ( $C_5H_5N$ , Fisher Scientific 99+%) was carried out as described in Section 2.5. The pyridine sample was degassed by three freeze-pump-thaw cycles. Purity of the pyridine was checked with mass spectrometry and established to have less than 5% impurities. Pyridine was not dried using molecular sieves, although the other two molecules studied for this thesis were dried in this manner. However, water desorption at 18 amu was monitored in subsequent TPD measurements and a negligible amount of contamination of the surface with coadsorbed water was observed. Pyridine exposures are reported using the indicated ion gauge readings and no correction was made for the ion-gauge sensitivity. The gas handling line was reconstructed with

stainless steel gaskets instead of copper gaskets after observing that the copper gaskets were reacting with pyridine.

Prior to each experiment, the Pt(111) crystal was cleaned according to the procedure described in Section 2.3. TPD experiments were conducted after exposures of pyridine on the Pt(111) sample at 100 K. TPD measurements were made using a 9 K/s heating rate and desorbed molecules were monitored using principally the signals for ion masses as follows: pyridine ( $C_5H_5N$ , 56 amu), dihydrogen ( $H_2$ , 2 amu), ammonia ( $NH_3$ , 17 amu), hydrogen cyanide ( $HCN$ , 27 amu), and cyanogen ( $C_2N_2$ , 52 amu).

### 3.3 Results and Discussion

Molecular pyridine desorption from the Pt(111) surface is shown in Figure 3.2. The low-temperature peak at 168 K is due to desorption of physisorbed pyridine from the multilayer. This temperature corresponds to a desorption activation barrier of 10 kcal/mol. Multilayer desorption of pyridine has been reported near 180 K from the Pd(111) surface<sup>25</sup>, and at 190 K on the Pt(111) surface.<sup>7</sup> The desorption peak at 247 K is assigned to desorption of chemisorbed pyridine from the monolayer. This temperature corresponds to  $E_{des}$  of 15 kcal/mol. Desorption of pyridine from Pt(111) was previously reported at 347 K, which is higher than our results. We have no explanation for this result. The small desorption peak at 464 K is similar to the 475 K peak in ref. 7, and this is assigned to the recombination of  $\alpha$ -pyridyl species with adsorbed hydrogen atom to yield desorbed pyridine. Of the pyridine desorbing from the monolayer, approximately 12% comes from the peak at 464 K. The recombination of  $\alpha$ -pyridyl and adsorbed H corresponds to  $E_{des}$  of 28 kcal/mol.

Desorption products that formed from the decomposition of pyridine on Pt(111) are shown in Figure 3.3. In addition to direct pyridine molecular desorption and

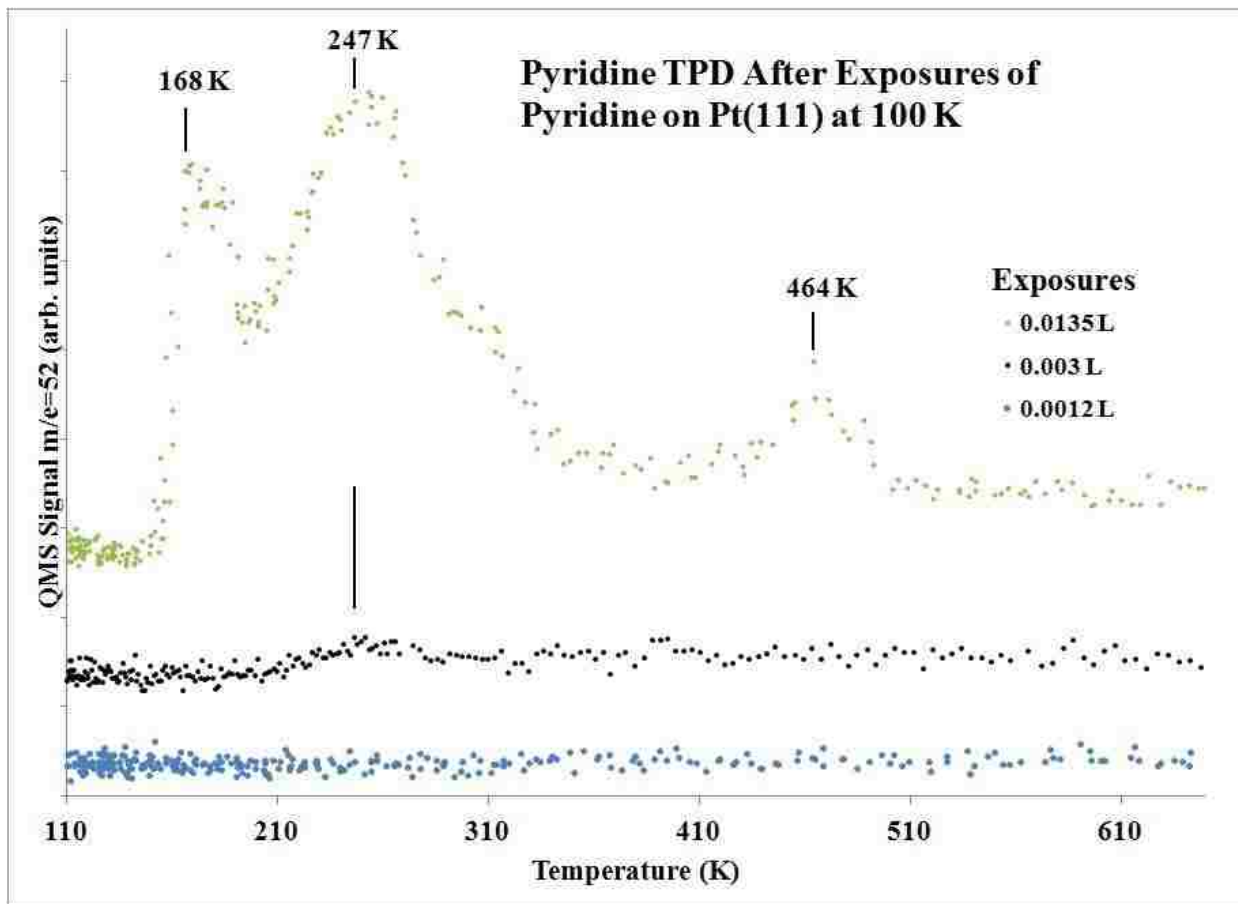


**Figure 3.2** Pyridine TPD after exposures of pyridine on Pt(111) at 100 K of 0.0135 0.003, and 0.0012 L.

recombinative pyridine desorption  $\alpha$ -pyridyl species and adsorbed hydrogen atoms, the following other desorption products were observed:  $H_2$ , HCN,  $NH_3$ , and  $C_2N_2$ . In Figure 3.3, the decline of the pyridine signal near 300 K coincides with the commencement of  $H_2$  desorption. Hydrogen cyanide desorption begins after the second  $H_2$  desorption peak. Both HCN and  $H_2$  desorption cease near 800 K, which is the temperature where  $C_2N_2$  desorption begins, which is due to the depletion of all H atoms from adsorbed reaction intermediates from the decomposition of pyridine on Pt(111). Figures 3.4, 3.5, and 3.6



show additional TPD spectra for the individual products. Ammonia desorption was not reproducible. A desorption peak at 341 K was observed for both 16 and 17 amu, which is indicative of  $\text{NH}_3$  desorption, but the signal was small and not consistently observed in all spectra.

Desorption of  $\text{H}_2$  begins as the desorption of pyridine ceases. The TPD spectra for  $\text{H}_2$  desorption are shown in Figure 3.4. The first desorption peak for  $\text{H}_2$  is at 345 K, which is assigned to a desorption rate-limited process, i.e. adsorbed hydrogen due to dehydrogenation of pyridine exists at lower temperatures, but does not recombine and

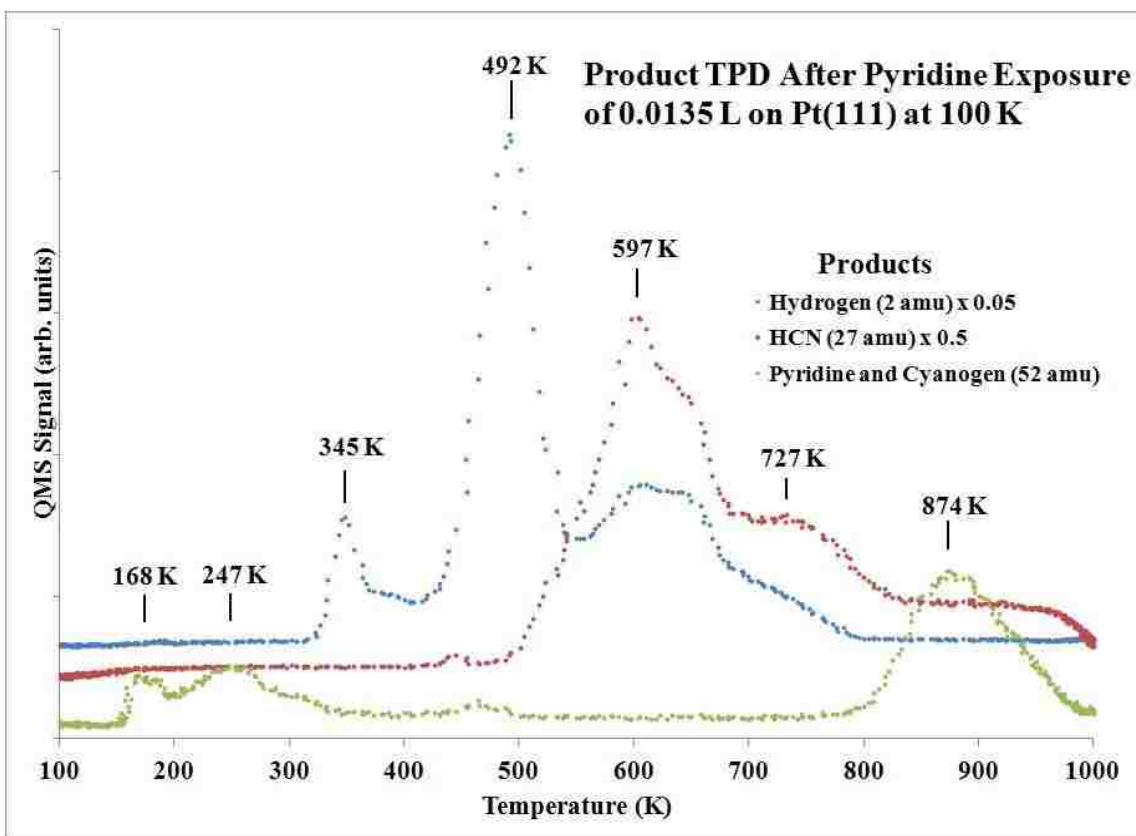


**Figure 3.3** Product TPD after pyridine exposure of 0.0135 L on Pt(111) at 100 K. Pyridine,  $\text{H}_2$ , HCN and  $\text{C}_2\text{N}_2$  desorption is shown by following 52, 2, 27, and 52 amu, respectively. Pyridine and cyanogen were both followed using 52 amu, but the high-temperature desorption was determined to only be cyanogen by simultaneously monitoring 26 amu, a fragment of cyanogen.

desorb as H<sub>2</sub> until the surface is heated to 350-370 K.<sup>32</sup> This first desorption peak at 345 K is assigned to the hydrogen cleaved from the dehydrogenation of the  $\alpha$ -carbon in the pyridine ring. According to previous vibrational studies at low temperature (250-300 K), the dehydrogenation of the  $\alpha$ -carbon forms an  $\alpha$ -pyridyl species, in which the adsorption intermediate is bonded via the nitrogen lone pair of electrons and the  $\alpha$ -carbon.<sup>6</sup> The desorption peak at 345 K constitutes approximately 10% of the hydrogen desorption.

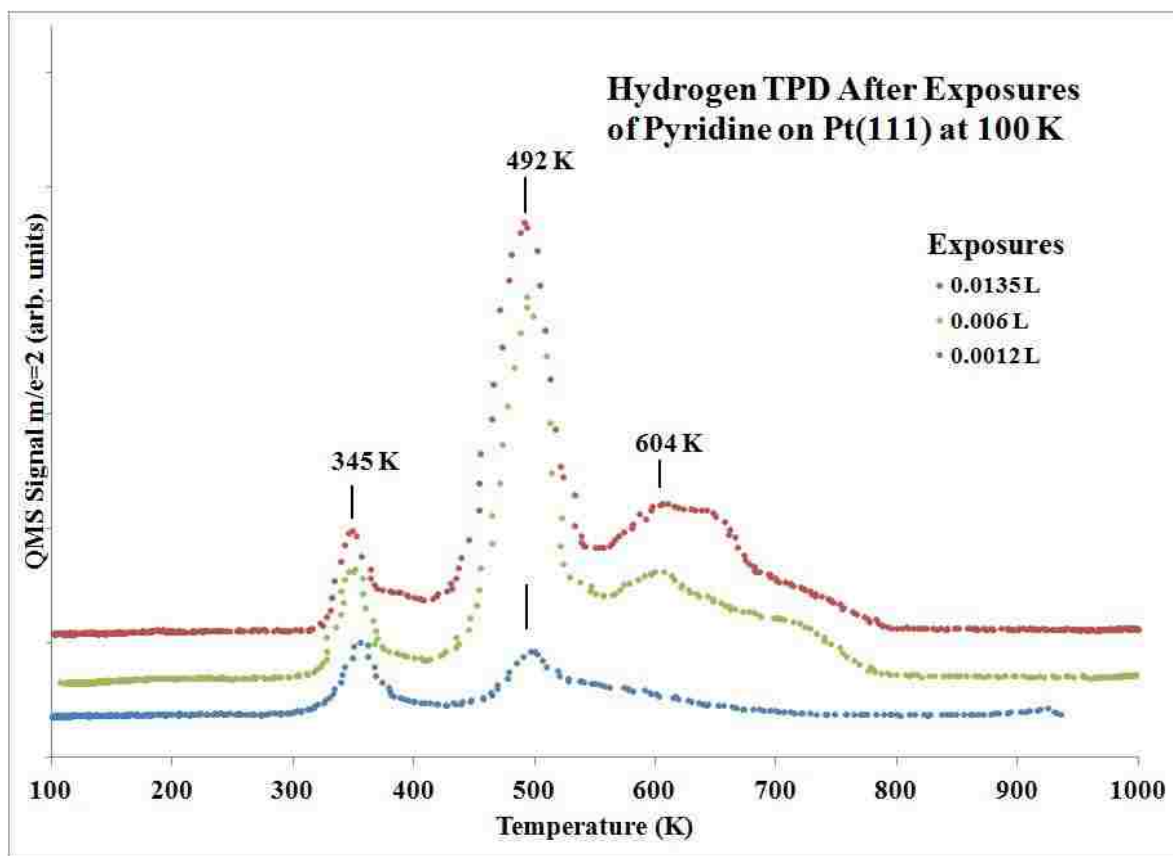


**Figure 3.4** Hydrogen (H<sub>2</sub>) TPD after exposures of pyridine on Pt(111) at 100 K of 0.0135, 0.006, and 0.0012 L.

The higher-temperature H<sub>2</sub> desorption peaks at 492 K and 604 K are assigned to sequential dehydrogenation of the  $\alpha$ -pyridyl species. Vibrational studies have shown that  $\alpha$ -pyridyl species decomposes at 350 K on Pt(111).<sup>6,11</sup> At higher temperatures, the  $\alpha$ -pyridyl species decomposes to form H<sub>2</sub>, HCN and adsorbed CN species. The higher

temperature H<sub>2</sub> desorption peaks are assigned to the loss of hydrogen during these processes. Other hydrogen TPD spectra for pyridine dehydrogenation also showed three major desorption peaks.<sup>7</sup> The two higher temperature H<sub>2</sub> desorption peaks are reaction rate-limited, i.e. the adsorbed hydrogen that leads to these peaks is only present after the activation barriers are overcome to dehydrogenate the remaining ring carbons and then recombinative desorption of H<sub>2</sub> occurs promptly.

Figure 3.5 shows the desorption of HCN from Pt(111) after adsorption of pyridine. Desorption is seen in a small peak at 439 K and a large, broad peak at 530 K, which shifts to higher temperatures with increasing exposures of pyridine. At the highest exposure, a high-temperature shoulder is seen at 727 K. The small peak at 439 K ( $E_{\text{des}} = 26$  kcal/mol) is assigned to molecular desorption of HCN that was created by the decomposition of pyridine, while the larger, broader peak is assigned to recombinative desorption of H<sub>ads</sub> and CN<sub>ads</sub>. This is supported by a previous report that after dissociative adsorption of HCN, desorption from Pt(111) occurred at 470 and 510 K.<sup>33</sup> The small peak assigned to direct HCN desorption constitutes less than 1% of the total HCN desorption at saturation coverage.

The production of HCN indicates the cleavage of carbon-carbon and carbon-nitrogen bonds in pyridine. Desorption of HCN at 439 K is designated as a desorption rate-limited process because the desorption of HCN after direct adsorption on Pt(111) was observed at 470 K.<sup>33</sup> The difference in observed desorption temperatures can be explained by differences in heating rates—the heating rate in ref. 33 was reported to be 30 K/s, while ours is 9 K/s. At higher coverage, HCN was observed to desorb at 510 K after adsorption of HCN on Pt(111).<sup>33</sup> Molecular adsorption of HCN occurs via the

nitrogen lone pair of electrons with the molecule perpendicular to the surface.<sup>34</sup> A hydrogen isocyanide (HNC) surface intermediate was identified on Pt(111) after adsorption of HCN on Pt(111) in ref. 34. This intermediate was determined to have a geometry more parallel to the surface plane. Simultaneous desorption of H<sub>2</sub> and HCN

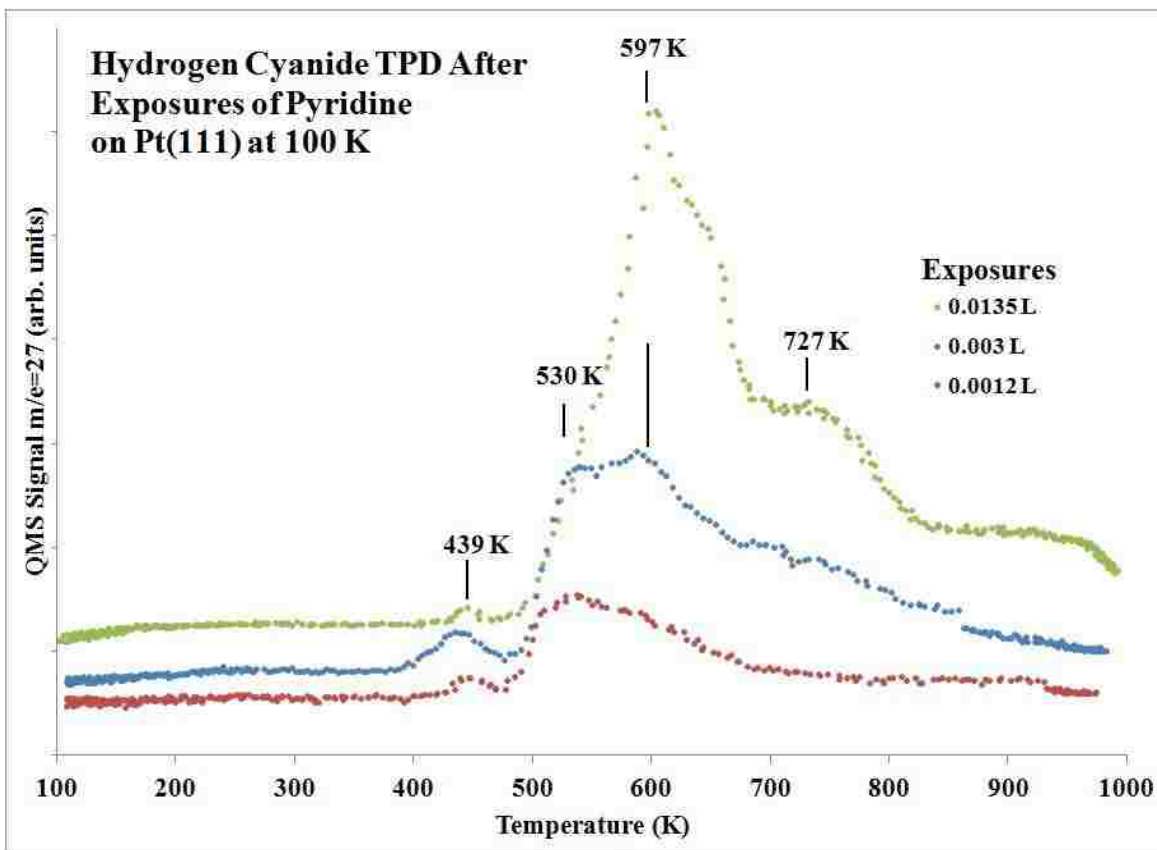


**Figure 3.5** Hydrogen cyanide (HCN) TPD after exposures of pyridine on Pt(111) at 100 K of 0.0135, 0.003, and 0.0012 L.

occurs during the decomposition of pyridine on Pt(111) until near 800 K. After warming the surface to this temperature, the presence of H<sub>ads</sub> has been diminished. The commencement of cyanogen (C<sub>2</sub>N<sub>2</sub>) desorption begins as production of gas-phase H<sub>2</sub> and HCN declines.

Desorption of C<sub>2</sub>N<sub>2</sub> is shown in Figure 3.6 after adsorption of pyridine on Pt(111). Monitoring 79, 52, 27, and 26 amu allowed for the identification of cyanogen by

comparing the TPD profiles of several fragmentation products of cyanogen, HCN, and pyridine. The fragmentation pattern of pyridine includes peaks at 79, 52, and 26 amu, cyanogen has peaks at 52 and 26 amu, and HCN has peaks at 27 and 26 amu. The desorption of cyanogen at 836-874 K was confirmed by observing identical TPD peak profiles for 52 and 26 amu, along with no desorption at 79 amu, over this temperature range.

Cyanogen desorption occurs at high temperature after adsorbed pyridine is dehydrogenated to leave adsorbed cyanide ( $\text{CN}_{\text{ads}}$ ) species on the surface. Cyanogen desorbs via an associative (recombinative) desorption process where two  $\text{CN}_{\text{ads}}$  species combine and then desorb at temperatures above 800 K. Previous literature showed that cyanogen adsorbs on Pt(111) dissociatively to form two  $\text{CN}_{\text{ads}}$  fragments on the surface.<sup>35</sup> Recombination via random coupling of  $\text{CN}_{\text{ads}}$  fragments was shown by an isotope experiment where a combination of  $^{12}\text{C}_2^{14}\text{N}_2$  and  $^{13}\text{C}_2^{15}\text{N}_2$  was dosed on a Pt(111) surface.<sup>35</sup> Dissociative adsorption followed by random associative desorption was observed by thermal desorption studies. Isotopic mixing was identified from the desorption peak at 54 amu, which corresponds to a combination of  $^{12}\text{C}^{14}\text{N}_{\text{ads}}$  and  $^{13}\text{C}^{15}\text{N}_{\text{ads}}$ .

Three desorption features— $\alpha$ ,  $\beta_1$ , and  $\beta_2$ —have been identified for cyanogen on Pt(111) after direct  $\text{C}_2\text{N}_2$  adsorption.<sup>35</sup> Desorption in the  $\alpha$  peak is at low temperature (370 K) and is from a less stable adsorption site. Desorption in the  $\beta_1$  and  $\beta_2$  peaks occur near 670 K, and between 740-780 K, respectively. The highest-temperature desorption species is similar to what is seen after the decomposition of pyridine in the present study. Isotopic studies in ref. 35 identified desorption in the  $\beta_2$  peak as associative desorption

because isotopic mixing was seen in the high temperature peak. Desorption in the  $\alpha$  peak showed no isotopic mixing. Not all authors resolve the high temperature desorption as  $\beta_1$  and  $\beta_2$ , but rather refer to it as one more complex desorption peak that is assigned to associative desorption.<sup>36</sup> Another account of  $C_2N_2$  thermal desorption reported the  $\alpha$  state desorbing near 370 K, while the  $\beta$  state desorbed with a peak maximum near 750 K.<sup>36</sup>

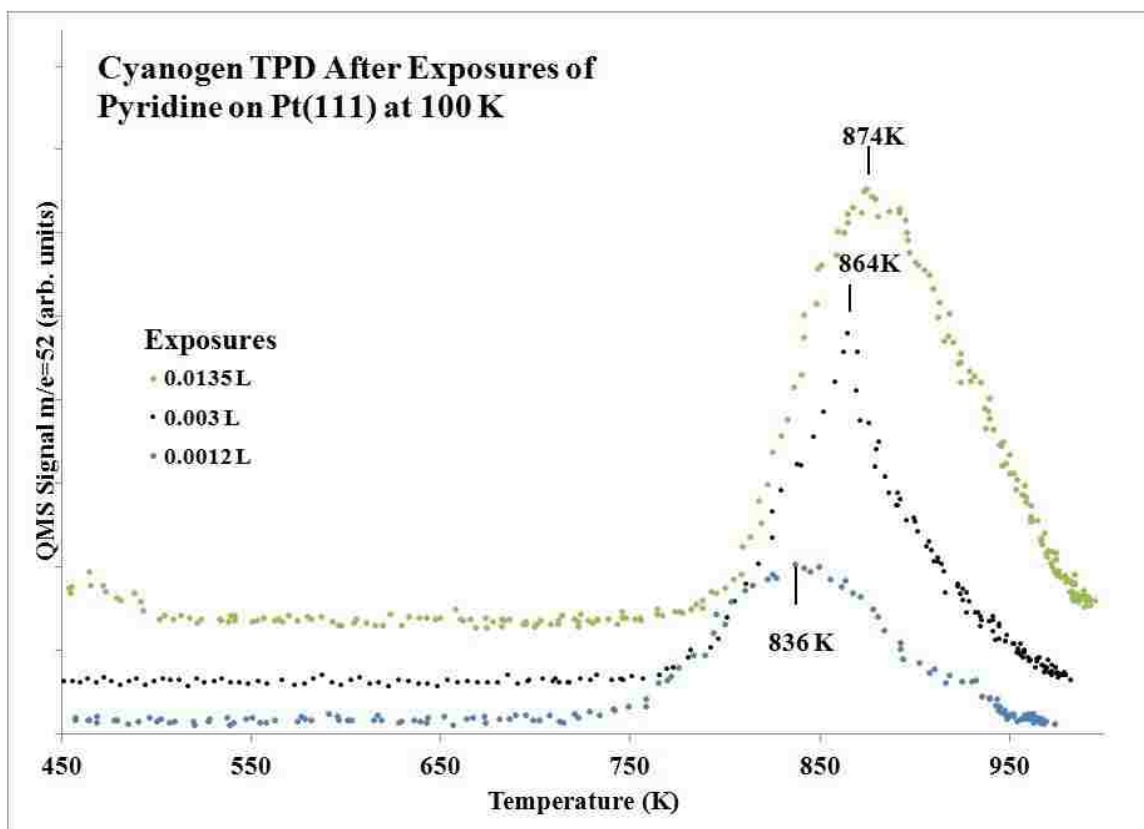


**Figure 3.6** Cyanogen ( $C_2N_2$ ) TPD after exposures of pyridine on Pt(111) at 100 K of 0.0135, 0.003, and 0.0012 L. Mass 26 was also monitored (not shown) to identify that this high temperature desorption was due to cyanogen, since pyridine also produces a cracking fraction at 52 amu.

The desorption temperature for  $C_2N_2$  from pyridine reaction in this thesis is 836 K and shifts to higher temperatures with increased exposures. The  $E_{des}$  corresponding to 836 K is 51 kcal/mol. This high-temperature desorption is attributed to a reaction rate-limited process where dehydrogenation of surface intermediates must occur to create  $CN_{ads}$

before the start of associative desorption. The shifting of the desorption peak to higher temperatures with increasing exposures is likely due to the limited surface sites for dehydrogenation at high coverage. Decomposition of symdimethylhydrazine (SDMH) on Pt(111) yielded a  $C_2N_2$  desorption peak at 890 K, which is similar to what we observed for pyridine reactions.<sup>33</sup>

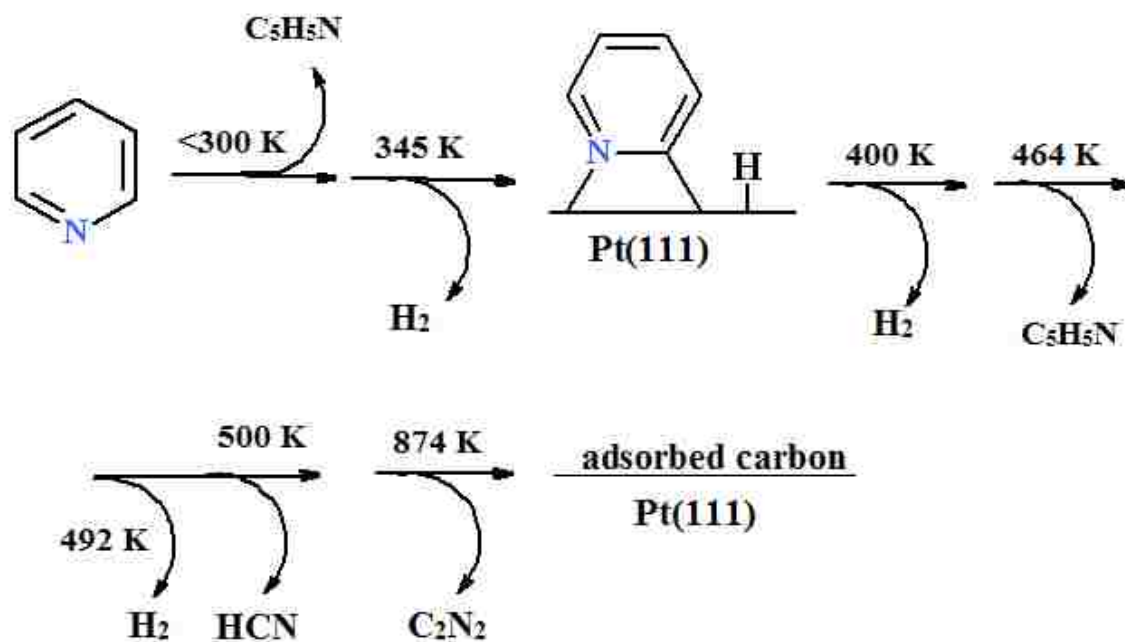
Similar associative desorption phenomena of cyanogen were observed in the decomposition of HCN on Pt(111).<sup>34</sup> Dissociative adsorption of HCN to form  $CN_{ads}$  and  $H_{ads}$  led to desorption of HCN,  $H_2$ , and  $C_2N_2$ , all via associative desorption from Pt(111).<sup>34</sup> Similarly to the liberation of cyanogen from pyridine reaction,  $C_2N_2$  did not desorb until  $H_2$  and HCN desorption slowed, which indicates that the adsorption energy of  $C_2N_2$  is larger than that for HCN and likely that the activation energy for cyanogen production via CC bond coupling of  $CN_{ads}$  species is larger than for hydrogenation of  $CN_{ads}$  species.

The adsorption geometry of  $CN_{ads}$  after dissociation of HCN on Pt(111) was characterized by vibrational spectroscopy to show the carbon-nitrogen bond parallel to the surface.<sup>19</sup> On Pd(111), dissociative adsorption of HCN causes rehybridization of the carbon-nitrogen bond to form a species with  $CN_{ads}$  bound to the surface via a di- $\sigma$  bond.<sup>23</sup> Adsorbed CN species being strongly bonded to the surface explains the high temperature desorption of  $C_2N_2$  in the decomposition of pyridine.

Because pyridine has a nitrogen atom within the ring, the production of HCN and  $C_2N_2$  from decomposition on the surface must be preceded by breaking a carbon-nitrogen bond, and also C-C bonds. On Pt(111), the lowest temperature where either of these products was observed is 439 K, which corresponds to direct desorption of HCN with a

desorption activation energy of 26 kcal/mol. This calculation was based on the Redhead analysis, as described in Section 2.5.<sup>37</sup> Based on previous literature, this desorption peak for HCN is due to a desorption rate-limited process, which means that the C-N bond must have been broken at a lower temperature. The activation barrier for C-N bond cleavage is therefore less than 26 kcal/mol on Pt(111). Previous studies reported that the  $\alpha$ -pyridyl species is stable until approximately 350 K, so this leads to the conclusion that the C-N bond must break between 350 and 439 K, or with an activation barrier between 21 and 26 kcal/mol.

The thermal decomposition of pyridine is detailed in Scheme 3.1, and this description is based on combined information from this thesis work and previous



**Scheme 3.1:** Decomposition pathway for pyridine on Pt(111)



literature. Upon the formation of an  $\alpha$ -pyridyl species on Pt(111), H<sub>2</sub> desorption occurs in a small peak at 345 K, which has been labeled as a desorption rate-limited process. Pyridine partially reversibly adsorbs, desorbing at 247 K. Another pyridine desorption peak at 464 K is assigned to recombinative desorption of the  $\alpha$ -pyridyl species and adsorbed hydrogen atoms. Significant dehydrogenation of the  $\alpha$ -pyridyl species is evident from the large H<sub>2</sub> desorption peak at 492 K. This peak constitutes 42% of the total H<sub>2</sub> desorption. A small peak due to HCN desorption is observed at 439 K, which is the first evidence in TPD of C-N bond cleavage. After the second H<sub>2</sub> desorption peak, a large peak due to HCN desorption appears with a peak maximum at 597 K. Nearly 60% of HCN desorption occurs between 500 and 700 K. Additional HCN continues to leave the surface until ~800 K, which is also the temperature where H<sub>2</sub> desorption stops and all hydrogen has been removed from surface species. The final product from the decomposition of pyridine on Pt(111) is cyanogen, which desorbs between 800 and 1000 K. The likely pathway for cyanogen formation is dehydrogenation to produce CN<sub>ads</sub> species on the surface, followed by recombination of these CN<sub>ads</sub> fragments to yield C<sub>2</sub>N<sub>2</sub> via an associative desorption process.

### 3.4 Conclusion

Pyridine adsorption and reaction was studied on a Pt(111) surface using TPD. Molecular pyridine desorbed at 168 and 247 K from the multilayer and monolayer, respectively, corresponding to desorption activation energies of 10 and 15 kcal/mol, respectively. Dehydrogenation of pyridine to produce  $\alpha$ -pyridyl species and H<sub>ads</sub> occurs prior to 345 K with an activation energy less than 21 kcal/mol. Some recombination of  $\alpha$ -pyridyl species and H<sub>ads</sub> yields a pyridine desorption peak at 464 K, with an activation

energy of 28 kcal/mol. The fraction of irreversibly adsorbed pyridine decomposed to form gas-phase products of H<sub>2</sub>, HCN, C<sub>2</sub>N<sub>2</sub>, and NH<sub>3</sub> during heating in TPD. Carbon-nitrogen bond cleavage was determined to occur between 350 and 439 K, which corresponds to an activation barrier between 21-26 kcal/mol. This information is discussed further in Chapter 5 in the context of cyclohexylamine and piperidine adsorption.

### 3.5 References

1. Furimsky, E.; Massoth, F.; *Catal. Rev. Sci. Eng.* **2005**, *47*, 297-489.
2. Lewandowski, M.; Sarbak, Z. *Appl. Catal., B* **2008**, *79*, 313-322.
3. Vít, Z.; Zdrzil, M.; *J. Catal.* **1989**, *119*, 1-7.
4. Joo, H.S.; Guin, J.A.; *Fuel Proc. Technol.* **1996**, *49*, 137-155.
5. Wu, X.; Waller, F.; Crezee, E.; Shan, Z.; Kapteijn, F.; and Moulijn, J.A.; *Stud. Surf. Sci. Catal.*, **2002**, *143*, 101-109.
6. Haq, S.; King, D. A. *J. Phys. Chem.* **1996**, *100*, 16957-16965.
7. Grassian, V.H.; Muetterties, E.L.; *J. Phys. Chem.* **1986**, *90*, 5900-5907.
8. Johnson, A.L.; Muetterties, E.L.; Stöhr, J.; Sette, F.; *J. Phys. Chem.* **1985**, *89*, 4071-4075.
9. Lee, I.C.; Masel, R.I.; *J. Phys. Chem. B* **2002**, *106*, 368-373.
10. Gland, J.L.; Somorjai, G.A.; *Surf. Sci.* **1973**, *38*, 157-186.
11. Kliewer, C. J.; Somorjai, G. A. *Catal. Lett.* **2010**, *137*, 118-122.
12. Surman, M.; Bare, S.R.; Hofmann, P.; King, D.A.; *Surf. Sci.* **1987**, *179*, 243-253.
13. Connolly, M.; Somers, J.; Bridge, M.E.; Lloyd, D.R.; *Surf. Sci.* **1987**, *185*, 559-568.
14. Fritzsche, V.; Bao, S.; Hofmann, Ph.; Polčik, M.; Schindler, K.-M.; Bradshaw, A.M.; Davis, R.; Woodruff, D.P.; *Surf. Sci.* **1994**, *319*, L1-L6.
15. Cohen, M.R.; Merrill, R.P.; *Langmuir*, **1990**, *6*, 1282-1288.
16. Cohen, M.R.; Merrill, R.P.; *Surf. Sci.* **1991**, *245*, 1-11.
17. Schoofs, G.R.; Benziger, J.B.; *J. Phys. Chem.* **1988**, *92*, 741-750.
18. DiNardo, N.J.; Avouris, Ph.; Demuth, J.E.; *J. Chem. Phys.* **1984**, *81*, 2169-2180.
19. Abdallah, W.A.; Nelson, A.E.; Gray, M.; *Surf. Sci.* **2004**, *569*, 193-206.
20. Rodriguez, J.A.; Dvorak, J.; Jirsak, T.; Li, S.Y.; Hrbek, J.; Capitano, A.T.; Gabelnick, A.M.; Gland, J.L.; *J. Phys. Chem. B* **1999**, *103*, 8310-8318.
21. Hahn, J.R.; Kang, H.S.; *Surf. Sci.* **2010**, *604*, 258-264.

22. Zhong, Q.; Gahl, C.; Wolf, M.; *Surf. Sci.* **2002**, *496*, 21-32.
23. Davies, P.R.; Shukla, N.; *Surf. Sci.* **1995**, *322*, 8-20.
24. Mack, J.U.; Bertel, E.; Netzer, F.P.; *Surf. Sci.* **1985**, *159*, 265-282.
25. Grassian, V.H.; Muetterties, E.L.; *J. Phys. Chem.* **1987**, *91*, 389-396.
26. Netzer, F.P.; Rangelov, G.; *Surf. Sci.* **1990**, *225*, 260-266.
27. Whitten, J.E.; *Surf. Sci.* **2003**, *546*, 107-116.
28. Jakob, P.; Lloyd, D.R.; Menzel, D.; *Surf. Sci.* **1990**, *227*, 325-336.
29. Kim, J.; Welch, L. A.; Olivas, A.; Podkolzin, S. G.; Koel, B. E.; *Langmuir*, **2010**, *26*, 16401-16411.
30. Janin, E.; von Schenck, H.; Ringler, S.; Weissenrieder, J.; Åkermark, T.; Göthelid, M.; *J. Catal.* **2003**, *215*, 245-253.
31. Haubrich, J.; Loffreda, D.; Delbecq, F.; Jugnet, Y.; Sautet, P.; Krupski, A.; Becker, C.; Wandelt, K. *Chem. Phys. Lett.* **2006**, *433*, 188-192.
32. Paffett, M.T.; Gebhard, S.C.; Windham, R.G.; Koel, B.E. *J. Phys. Chem.* **1990**, *94*, 6831-6839.
33. Somers, J.S.; Bridge, M.E.; *Surf. Sci.* **1985**, *159*, L439-444.
34. Jentz, D.; Celio, H.; Mills, P.; Trenary, M.; *Surf. Sci.* **1995**, 1-8.
35. Hoffmann, W.; Bertel, E.; Netzer, F.P.; *J. Catal.* **1979**, *60*, 316-324.
36. Lindquist, J.M.; Ziegler, J.P.; Hemminger, J.C.; *Surf. Sci.* **1989**, *210*, 27-45.
37. Redhead, P.; *Vacuum* **1962**, *12*, 203-211.

## Chapter 4: Adsorption and Reaction of Cyclohexylamine on Pt(111)

### 4.0 Abstract

Adsorption and reaction of cyclohexylamine ( $C_6H_{11}NH_2$ ) was studied on Pt(111) by temperature programmed desorption (TPD). Molecular desorption occurred from the multilayer and the monolayer at 187 and 217 K, respectively. Cyclohexylamine that did not desorb decomposed on the surface to form desorption products of hydrogen ( $H_2$ ), hydrogen cyanide (HCN), cyanogen ( $C_2N_2$ ), and ammonia ( $NH_3$ ). Sequential dehydrogenation of cyclohexylamine begins with the cleavage of amine hydrogens, followed by the removal of H atoms from the ring carbons. Reaction of  $C_6H_{11}NH_2$  did not yield any large, stable desorption products, such as benzene or aniline. The upper bound for the activation barrier for C-N bond cleavage in cyclohexylamine is 20 kcal/mol.

### 4.1 Introduction

As stated in Chapter 3.1, the hydrotreating process in oil refineries removes nitrogen and sulfur from crude oil prior to catalytic reforming.<sup>1</sup> Removal of nitrogen and sulfur reduces toxic emissions from the combustion of fuels, and limits the poisoning of noble metals in catalytic converters.<sup>1</sup> Typical commercial catalysts for hydrotreating are supported bimetallic catalysts composed of nickel, cobalt, molybdenum and tungsten.<sup>1</sup> Studies have shown that supported platinum catalysts exhibit higher activity for hydrodenitrogenation (HDN) and hydrodesulfurization (HDS). Specifically, sulfided Pt catalysts<sup>1</sup> and bimetallic PtSn/SiO<sub>2</sub><sup>2</sup> have shown increased activity for hydrotreating catalysis compared to commercial catalysts such as NiMo/Al<sub>2</sub>O<sub>3</sub>. Work by Lewandowski showed support effects on the activity and selectivity for PtSn in HDN and HDS.<sup>2</sup> Silica-supported PtSn exhibited a higher HDN activity than PtSn/Al<sub>2</sub>O<sub>3</sub>. They reported that more alloyed PtSn phases existed on the silica support than the alumina support and that the electronic effects from alloying could improve catalytic activity. This agrees with previous reports about PtSn alloying on silica supports.<sup>3,4</sup>

Currently, there is no data available regarding the fundamental surface science of cyclic nitrogen-containing molecules on PtSn surfaces. Furthermore, platinum single-crystal surface studies of these molecules are limited to mainly that of pyridine ( $C_5H_5N$ )<sup>5-12</sup> and aniline ( $C_6H_5NH_2$ ).<sup>13</sup> This thesis provides additional information about the fundamental chemistry of these molecules on the Pt(111) single crystal surface. This chapter presents temperature programmed desorption (TPD) data for the adsorption and reaction of cyclohexylamine on Pt(111).

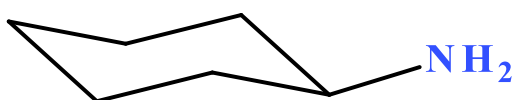


**Figure 4.1**  
**Structure of**  
**cyclohexylamine**

Cyclohexylamine ( $C_6H_{11}NH_2$ ) is a saturated cyclic molecule with an amine group attached to the ring, as seen in Figure 4.1. At the time this thesis was written, there was no record of

cyclohexylamine adsorption studies on the Pt(111) surface, though studies of the adsorption of cyclohexylamine on Ni(111)<sup>14</sup> and Ni(100)<sup>15</sup> reported adsorption geometries and structure-sensitive reactions. A review of surface science studies of simple amines on metal surfaces provides insight into how amine structure affects adsorption and reaction. Methylamine ( $CH_3NH_2$ ), dimethylamine ( $(CH_3)_2NH$ ), and trimethylamine ( $N(CH_3)_3$ ) have all been studied on Pt and other noble metal surfaces.

Two articles reporting adsorption of methylamine on Pt(111) were submitted at approximately the same time.<sup>16,17</sup> Both report TPD results. Methylamine, a primary amine, adsorbed on Pt(111) yielded methane, cyanogen ( $C_2N_2$ ), dihydrogen ( $H_2$ ), hydrogen cyanide (HCN), and nitrogen ( $N_2$ ) as products in TPD<sup>17</sup>, however, ref. 16 reported that no desorption products due to C-N cleavage (methane and nitrogen) were

observed. No ammonia ( $\text{NH}_3$ ) was reported as a desorption product. Isotopic studies revealed that the N-H bonds were less stable than the C-H bonds, and the N-H bonds were cleaved at lower temperatures during TPD.<sup>17</sup> Methylamine adsorbed via the nitrogen lone pair of electrons to the Pt surface. Monolayer desorption of methylamine was observed at 230 K.<sup>16</sup> Desorption of cyanogen began after desorption of  $\text{H}_2$  and HCN diminished, which indicates that the barrier for CN coupling is larger than the barrier to dehydrogenation and that  $\text{C}_2\text{N}_2$  only desorbs following complete dehydrogenation of all intermediate species on the surface. At lower initial coverages,  $\text{C}_2\text{N}_2$  desorption followed second order kinetics as expected from recombination of adsorbed CN fragments. Cyanogen was the only product to desorb above 1000 K.

Methylamine adsorbed on Pd(111) yielded desorption products of  $\text{H}_2$  and HCN in TPD.<sup>18</sup> No C-N bond cleavage was observed. No  $\text{C}_2\text{N}_2$  was observed as a product, which contrasts with the reaction of methylamine on Pt(111). An isotopic study on Pd(111) using  $\text{d}_3$ -methylamine showed that methyl hydrogens are more stable than amino hydrogens, which agrees with ref. 17. Two desorption peaks were observed for HCN; the lower-temperature peak (between 300 and 350 K) was identified as direct, first-order desorption, while desorption between 360 and 510 K was assigned to the recombination of adsorbed CN and H. No desorption was observed above 500 K.<sup>18</sup>

Dimethylamine, a secondary amine, also bonds to metal surfaces via the nitrogen lone pair of electrons.<sup>19-22</sup> Decomposition products during TPD on Pt(111) are  $\text{H}_2$  and HCN. Carbon and CN fragments remained on the surface after TPD. Cyanogen desorption was monitored at 52 amu, but it was not observed, which contrasts with the reaction of methylamine on Pt(111). A more recent study from the Trenary group

reported the formation of methylisocyanide ( $\text{CH}_3\text{NC}$ ) from dimethylamine on Pt(111).<sup>20</sup> Identification of this stable intermediate indicated that after partial dehydrogenation of dimethylamine, adsorption is via one of the methyl carbons instead of through the nitrogen lone pair of electrons. Another stable intermediate, methylaminocarbyne ( $\text{CNHCH}_3$ ), was identified on both the Pt(111) and Ni(111) surfaces.<sup>19-21</sup> Dimethylamine desorbs from Cu(110) at 315 K, and from oxidized Cu(110) at 215 K, which indicates oxidation of copper weakens the molecule's interaction with the surface.<sup>22</sup>

Trimethylamine, a tertiary amine, bonds to metal surfaces via the nitrogen lone pair of electrons.<sup>23,24</sup> Carbon-nitrogen bond cleavage was observed when trimethylamine was adsorbed on Pt(111). The first, second and third C-N bonds were cleaved at 280, 410, and 492 K, corresponding to activation barriers of 18, 26, and 32 kcal/mol, respectively.<sup>23</sup> No HCN or  $\text{C}_2\text{N}_2$  desorbed as products in TPD. Nitrogen desorbed at 500 K and at higher temperatures. Dimethylaminocarbyne ( $\text{CN}(\text{CH}_3)_2$ ) was a stable intermediate which was identified in the reaction of trimethylamine on Pt(111).<sup>24</sup> This intermediate is similar to what was identified in the reaction of dimethylamine.<sup>21</sup> From the review of these simple amines, it is clear that the structure of these three molecules does not affect how they bond to the surface (always via the nitrogen lone pair of electrons), but the differences of the molecules' decomposition pathway and subsequent desorption products are dependent on structure. Methylamine yields  $\text{C}_2\text{N}_2$  and HCN; dimethylamine yields HCN but not  $\text{C}_2\text{N}_2$ ; and trimethylamine only undergoes C-N cleavage. All three molecules produce  $\text{H}_2$  due to dehydrogenation.

Cyclic amine compounds such as aniline and cyclohexylamine (both primary amines) and N-methylaniline ( $\text{C}_6\text{H}_5\text{NHCH}_3$ , a secondary amine) react to form similar

decomposition products as for the mono-, di-, and trimethylamine molecules on metal surfaces. Aniline desorbs from the multilayer on Pt(111) at 200 K and from the monolayer at 240 K, corresponding to an activation barrier for desorption of 15 kcal/mol.<sup>13</sup> Benzene (C<sub>6</sub>H<sub>6</sub>) and NH<sub>3</sub> were observed as hydrogenolysis products between 400 and 500 K during TPD. Hydrogen desorption occurred in peaks at 350 and 470 K and several broad peaks above 500 K. The aniline adsorption geometry was determined to be tilted on Pt(111) with bonding between the nitrogen lone pair of electrons and the surface. Coadsorption of hydrogen caused an adsorption geometry with the ring parallel to the surface. This geometry also led to a larger production of ammonia gas due to enhanced hydrogenolysis activity. Aside from benzene, NH<sub>3</sub>, H<sub>2</sub>, and aniline, no other desorption products were reported in this study. An older study reported aniline adsorption with the molecular ring parallel to the surface on Pt(111) and Pt(100).<sup>25</sup>  $\pi$ -bonding was reported to be the primary bonding interaction between aniline and the two platinum surfaces.

Nickel single crystal studies yielded similar reaction products and structure sensitive reactions.<sup>26-28</sup> Dehydrogenation of aniline on Ni(111) and Ni(100) caused H<sub>2</sub> desorption between 300 and 700 K.<sup>26,27</sup> Cleavage of the carbon-nitrogen bond was favored more on the Ni(100) surface than Ni(111), indicating a more open structure is more conducive to hydrogenolysis.<sup>27</sup> Preadsorption of hydrogen on Ni(111) enhanced hydrogenolysis and caused benzene desorption at 470 K, but even H<sub>2</sub> pressures in the millitorr range did not promote complete hydrogenolysis. Ni(100), however, facilitated complete hydrogenolysis of adsorbed aniline with a H<sub>2</sub> pressure of 10<sup>-6</sup> Torr. Desorption products from the reaction of aniline on nickel single crystals included NH<sub>3</sub>, HCN,



benzene, H<sub>2</sub>, and small amounts of ethylene (C<sub>2</sub>H<sub>4</sub>) and N<sub>2</sub>. An aniline isotope study indicated that N-H bonds were broken at lower temperatures than C-H bonds on the ring.<sup>28</sup> Fluorescence yield near-edge spectroscopy (FYNES) was used to show that aniline adsorbed on the Ni(111) surface with the ring more parallel to the surface than on Ni(100) below temperatures where hydrogenolysis was observed. Stronger  $\pi$  interactions between the adsorbate and the Ni(111) surface were linked to dehydrogenation being the preferred reaction pathway. Conversely, on Ni(100), aniline has weaker  $\pi$  interactions with the surface and even in the absence of H<sub>2</sub> background pressures, hydrogenolysis was reported to be the preferred reaction pathway.<sup>27</sup>

Supported nickel catalysts have been used in hydrogenation reactions to form cyclohexylamine from aniline.<sup>29,30</sup> Alumina-supported nickel yielded N-phenylcyclohexylamine as the major product in the hydrogenation of aniline.<sup>29</sup> N-phenylcyclohexylamine was produced selectively at low conversions and on catalysts with low nickel content. Increasing the nickel content of the catalyst from 10 wt.% to 50 wt.% increased the conversion of aniline. Cyclohexylamine was observed at higher reaction temperatures and when higher conversion was observed. Carbon-nitrogen bond cleavage was observed by the production of cyclohexane at reaction temperatures at and above 573 K. In aniline hydrogenation, rhodium supported on an alumina support was reported to be more selective than Ni/Al<sub>2</sub>O<sub>3</sub> for cyclohexylamine and dicyclohexylamine.<sup>31,32</sup> Hydrogenation of aniline on Ni/La<sub>2</sub>O<sub>3</sub> was more selective for cyclohexylamine after treatment with sodium hydroxide.<sup>32</sup> Addition of NaOH to the supported catalyst had an electronic effect, which complemented the basicity of the lanthana support to promote the isolation of primary amines on the surface and reduce the

selectivity toward secondary amines.<sup>32</sup> Aniline bonded via the nitrogen lone pair of electrons on oxygen-pretreated Ni films, but via  $\pi$  interactions with the aromatic ring on the metallic Ni surface.<sup>33</sup> These reports indicate that the reaction pathway for aniline is not only structure sensitive, but it is also affected by the acidity of the surface sites.

Adsorption of aniline has also been studied on rhodium, silver, and copper single crystal surfaces.<sup>34-36</sup> On Rh(111), physisorbed aniline desorbed between 210 and 230 K. Chemisorbed aniline does not desorb from Rh(111), but instead completely decomposes to yield other desorption products. Aniline reacts on Rh(111) to form H<sub>2</sub>, HCN, and N<sub>2</sub>.<sup>34</sup> No benzene or C<sub>2</sub>N<sub>2</sub> was observed during TPD. Hydrogen desorption occurred in three peaks at 330, 460, and 680 K. The low-temperature peak was determined to be from a desorption-limited process and consisted of amine hydrogens, while H<sub>2</sub> desorption in the two higher-temperature peaks was due to the dehydrogenation of the ring carbons. Desorption of HCN occurred between 550 and 800 K and N<sub>2</sub> desorption began above 800 K.

Aniline adsorption studies on Ag(111) and Ag(110) surfaces revealed a similar structure-sensitive effect to that of nickel surfaces. The aromatic ring geometry is more parallel to the Ag(111) surface compared to that on Ag(110).<sup>36,37</sup> On Ag(111), the ring is relatively flat with an angle between the ring and the surface of  $13\pm 8^\circ$ , while the angle is  $39\pm 5^\circ$  on Ag(110). In addition, desorption from the monolayer occurs at 325 K on Ag(110) and at 250 K on Ag(111). No reaction was reported on either silver surface to yield decomposition or reaction products in TPD. Aniline has a stronger bonding interaction with Ag(110), the more open surface structure. On Cu(110), aniline reaction produced H<sub>2</sub> and N<sub>2</sub>, but no benzene, NH<sub>3</sub>, or ethyne (C<sub>2</sub>H<sub>2</sub>) was observed.<sup>35</sup> Hydrogen

desorption was observed at temperatures below 250 K, while N<sub>2</sub> occurred in desorption peaks at 525 and 775 K. Adsorbed carbon remained on the surface after TPD measurements.

N-methylaniline adsorbed on Pt(111) produces decomposition products of H<sub>2</sub> and HCN during TPD.<sup>38</sup> H<sub>2</sub> desorption was observed in peaks at 365 and 440 K. Hydrogen cyanide desorbed in a range of temperatures between 500 and 850 K. Ammonia, N<sub>2</sub>, benzene, and C<sub>2</sub>N<sub>2</sub> were not observed as decomposition products. This absence of products differs from the decomposition of pyridine. Thermal desorption experiments in ref. 38 reached temperatures as high as 1000 K, so if C<sub>2</sub>N<sub>2</sub> was a decomposition product of n-methylaniline, the activation barrier for its formation is higher than what was observed in pyridine decomposition. The absence of C<sub>2</sub>N<sub>2</sub> as a decomposition product is in agreement with dimethylamine decomposition on Pt(111), and both of these molecules are secondary amines. This similarity indicates that the structure of the amine affects its decomposition pathway.

Adsorption and reaction studies of cyclohexylamine on the Ni(111) surface revealed that the molecule bonds to the surface via the nitrogen atom.<sup>14</sup> Dehydrogenation of the  $\alpha$ -carbon to permit the bonding of the nitrogen and a neighboring carbon atom to the surface weakens the C-N bond and leads to bond cleavage. The rate-limiting step for this reaction was reported to be the dehydrogenation of the molecule to reorient the ring to a geometry more parallel to the surface compared to that when it is upright and bound only by the nitrogen atom.<sup>14</sup>

Thermal desorption studies of cyclohexylamine on Ni(111) yielded decomposition products of H<sub>2</sub>, HCN, benzene, NH<sub>3</sub>, and N<sub>2</sub>. A fragment at 26 amu was

observed and designated as (-CN), but was not assigned to a cracking fragment of HCN or C<sub>2</sub>N<sub>2</sub>. Cyclohexylamine desorbed at 180 and 325 K from the multilayer and monolayer, respectively. Hydrogen desorption was observed to begin at 380 K and continued until 650 K. Desorption of benzene and NH<sub>3</sub> indicated carbon-nitrogen bond cleavage at 380 K.<sup>14</sup>

Cyclohexylamine has a stronger interaction with Ni(100) than Ni(111).<sup>15</sup> Cyclohexylamine desorbed at 200 and 335 K from the multilayer and monolayer, respectively, on Ni(100). This indicates a slightly stronger adsorption bond in the monolayer compared to that on Ni(111). Hydrogen desorption due to dehydrogenation was observed between 320 and 700 K with the largest peak at 350 K. Carbon-nitrogen bond cleavage was indicated by the desorption of NH<sub>3</sub> at 365 K, followed by benzene desorption at 465 K. Hydrogenolysis activity for cyclohexylamine is higher on Ni(100) than on Ni(111), which indicates a structure-sensitive reaction.<sup>14,15</sup>

Cyclohexylamine was studied in addition to pyridine and piperidine to identify the effect of the nitrogen atom environment on the adsorption and reaction of nitrogen containing molecules on Pt(111). An understanding of the surface science of these molecules could lead to an understanding of why supported PtSn demonstrates high activity in HDN reactions.<sup>2</sup> The thermal decomposition pathway for cyclohexylamine on Pt(111) is detailed in this chapter.

## 4.2 Experimental Methods

Gas dosing of cyclohexylamine (Alfa Aesar, 99%) was preceded by three freeze-pump-thaw purification cycles. In addition, cyclohexylamine was placed in the dosing test tube with 4Å molecular sieves (Aldrich, 3.2 mm) to remove water. The molecular

sieves were baked in an oven for 2.5 hrs at 175°C, and then stored in a desiccator until they cooled to room temperature. Purity of the cyclohexylamine leaked into the UHV chamber was checked with mass spectrometry. Corrections were not made for ion-gauge sensitivities in reporting gas exposures. The gas-handling line was constructed with stainless steel gaskets instead of copper gaskets to limit side reactions with copper. Prior to each experiment, the Pt(111) crystal was cleaned according to the procedure described in Section 2.3. Cyclohexylamine (C<sub>6</sub>H<sub>11</sub>NH<sub>2</sub>) was adsorbed on a Pt(111) single crystal at 100 K before performing TPD experiments. Cyclohexylamine was monitored by following 56 amu because it is the largest cracking fraction for this molecule.

#### 4.3 Results and Discussion

The most strongly adsorbed cyclohexylamine desorbs molecularly from the Pt(111) surface at 341 K, initially in a fairly narrow peak at low coverages in the monolayer, but then the TPD profile broadens to include more weakly bound molecules at temperatures down to 187 K where the multilayer, physisorbed cyclohexylamine desorbs (Figure 4.2). Another desorption peak was sometimes observed at 217 K, and this peak could possibly be due to physisorbed species adsorbed in the second layer. Assignment of this desorption feature as a second adsorbed layer agrees with cyclohexylamine desorption on Ni(111), where a small, low-temperature shoulder was observed on the monolayer desorption peak, though there was no explanation provided for this peak.<sup>14</sup> The onset for cyclohexylamine desorption near 170 K after higher exposures leads to a desorption peak at 187 K ( $E_{\text{des}} = 11$  kcal/mol) due to the condensed multilayer film (confirmed in additional experiments, not shown). Cyclohexylamine adsorbed on Ni(111) desorbed from a condensed multilayer state at 180 K.<sup>14</sup>  $E_{\text{des}}$  refers

to the desorption activation barrier, which may be either desorption- or reaction-limited. Desorption-limited activation barriers are due to surface process in which the barrier for desorption is lower than the barrier for decomposition. Reaction-rate limited processes

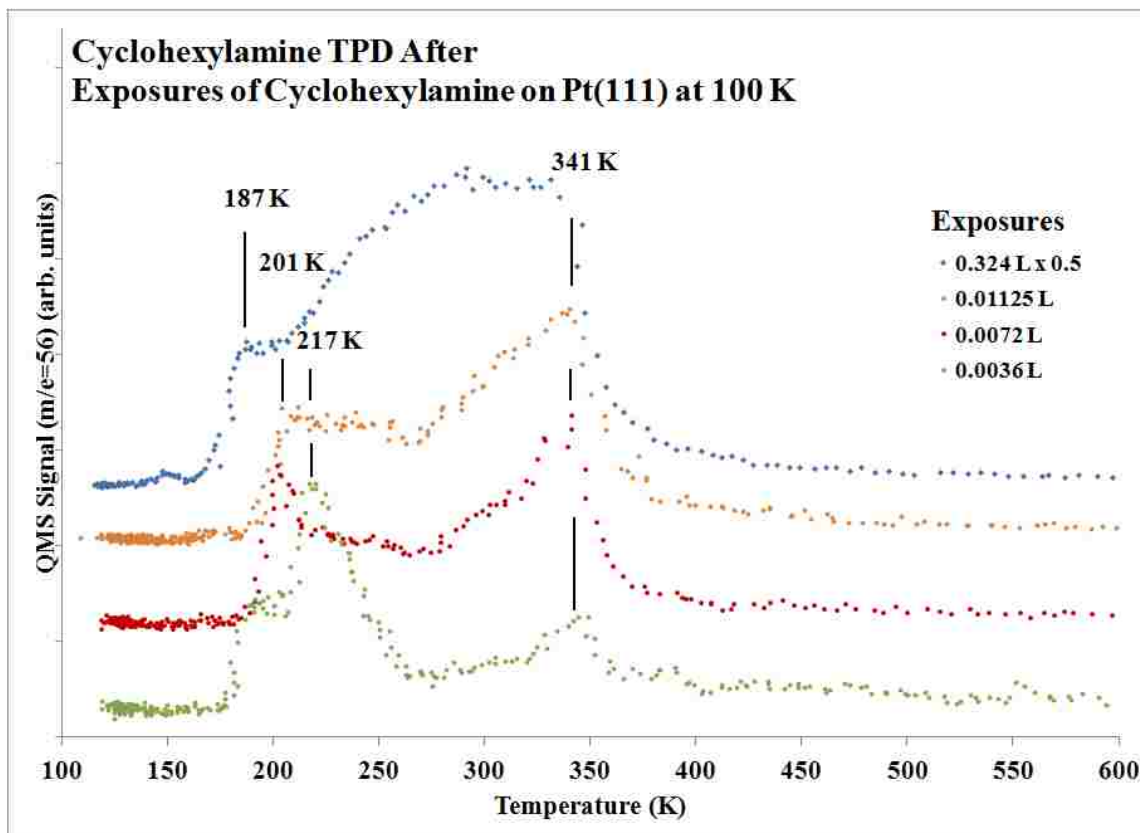


**Figure 4.2** Cyclohexylamine TPD after exposures of cyclohexylamine on Pt(111) at 100 K of 0.324, 0.01125, 0.0072, and 0.0036 L.

occur at higher temperatures due to a higher activation barrier in the formation of desorption products.

Cyclohexylamine desorption peaks at 217 and 341 K correspond to values of  $E_{des}$  of 11 and 19 kcal/mol, respectively. Thus the chemisorption bond strength of molecular cyclohexylamine is 11-19 kcal/mol. The value of  $E_{des}$  for desorption from the multilayer

was 11 kcal/mol. Chemisorbed cyclohexylamine was also dehydrogenated on the surface

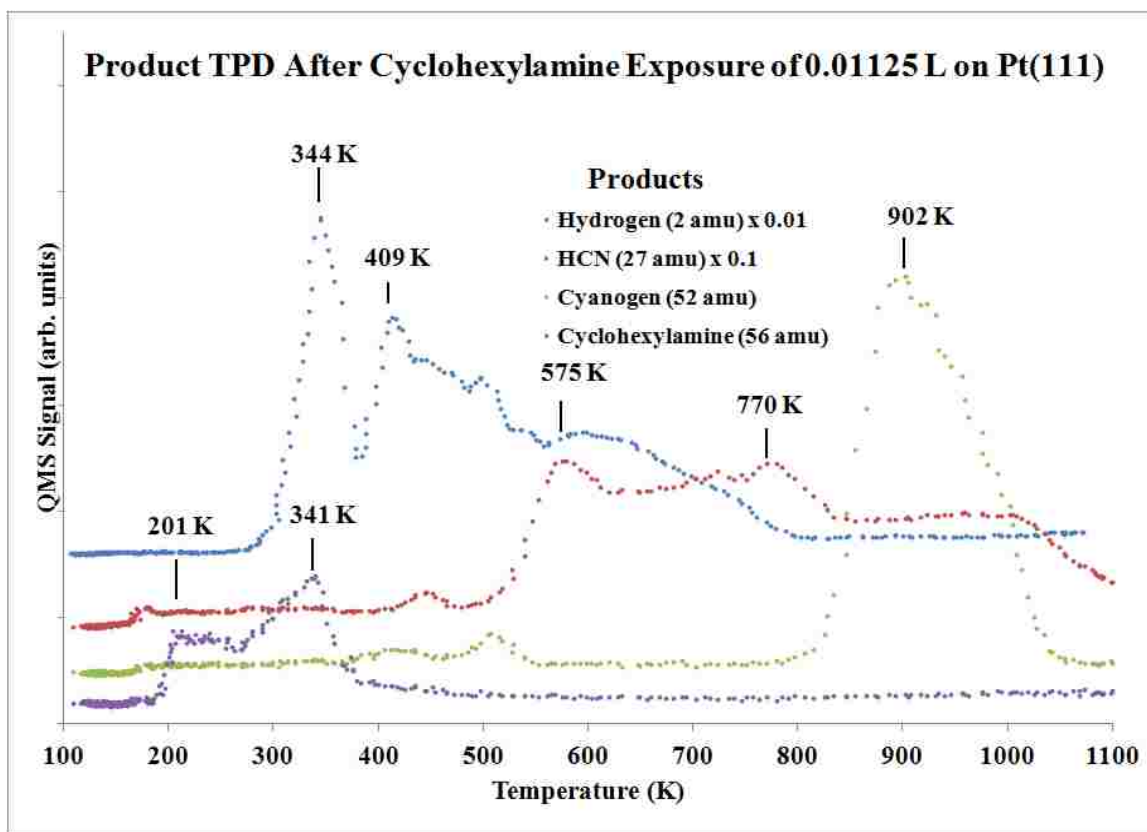


**Figure 4.3** Products monitored by TPD after a cyclohexylamine exposure of 0.01125 L on Pt(111) at 100 K. Signals at 56, 2, 27, and 52 amu were monitored for cyclohexylamine, H<sub>2</sub>, HCN, and C<sub>2</sub>N<sub>2</sub>, respectively. The signals for H<sub>2</sub> and HCN were multiplied by 0.01 and 0.1, respectively, to account for the different sensitivity factors used during data acquisition.

to eventually form surface carbon, as seen by AES (not shown) after TPD measurements.

A comparison of the TPD spectra for cyclohexylamine and the several products that desorb after a cyclohexylamine exposure of 0.01125 L on Pt(111) at 100 K, i.e., H<sub>2</sub>, HCN, and C<sub>2</sub>N<sub>2</sub>, is displayed in Figure 4.3. Desorption of cyclohexylamine stops as soon as the desorption of H<sub>2</sub> begins. Dehydrogenation occurred to liberate H<sub>2</sub>, with the lowest hydrogen-desorption peak at 344 K (Figure 4.4). This peak is the most defined and prominent of the dehydrogenation peaks. This low-temperature H<sub>2</sub> peak is attributed to

cleavage of N-H bonds based on previous isotopic studies that reported N-H cleavage at lower temperatures than C-H bond cleavage.<sup>17</sup> Subsequent H<sub>2</sub> desorption peaks are assigned to dehydrogenation of the ring carbons. Additional H<sub>2</sub> desorbed in peaks at 417 and 515 K, and in broad feature that extended to 800 K. At 800 K, all H atoms are removed from any species on the surface, and HCN desorption also stops at 800 K.

Hydrogen cyanide (27 amu) desorption (Figure 4.5) was observed in a small peak at 445 K, followed by three larger peaks at 575, 770, and 1000 K. The highest temperature HCN desorption feature is difficult to understand, and outgassing of the sample holder may be the cause. Desorption of H<sub>2</sub> ends at 800 K, so no HCN should continue to desorb after this temperature. The small desorption peak at 445 K is assigned to desorption of HCN after dehydrogenation of cyclohexylamine, and this peak constitutes less than 2% of the total HCN desorption. The major desorption peak at 575 K corresponds to a desorption activation energy,  $E_{\text{des}}$  of 35 kcal/mol. The larger peaks at 575 and 770 K are attributed to recombinative desorption from CN<sub>ads</sub> and H<sub>ads</sub> fragments on the surface after extensive dehydrogenation of cyclohexylamine.<sup>39</sup> This desorption phenomenon is similar that what was observed for pyridine reaction on Pt(111), reported in Chapter 3 of this thesis

A C<sub>2</sub>N<sub>2</sub> desorption peak occurs at 902 K, after small amount of C<sub>2</sub>N<sub>2</sub> desorbing in a peak at 509 K (Figure 4.6). The large C<sub>2</sub>N<sub>2</sub> desorption peak, constituting 98% of the total cyanogen desorption, corresponds to an  $E_{\text{des}}$  of 58 kcal/mol. Desorption in this peak is attributed to associative desorption of two CN<sub>ads</sub> fragments, which is similarly discussed in Chapter 3.3, and thus 58 kcal/mol corresponds to the barrier to



recombination.<sup>40,41</sup> Another desorption product from cyclohexylamine decomposition was ammonia.

. Ammonia desorbed in peaks at 334, 384 and 488 K (not shown here, and non-reproducible). Signals at 16, 17 and 18 amu were followed to confirm that these peaks were not cracking fractions of coadsorbed water or CO. Ammonia also desorbed from

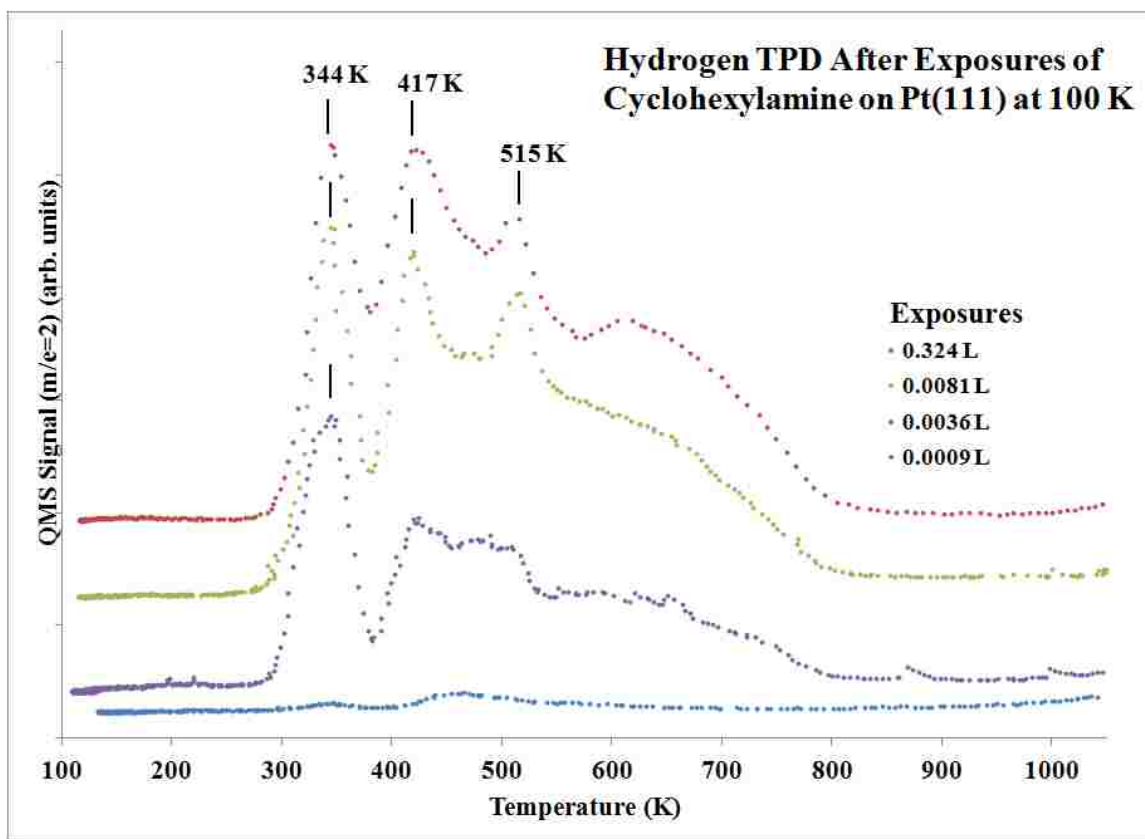


**Figure 4.4** H<sub>2</sub> TPD after exposures of cyclohexylamine on Pt(111) at 100 K of 0.324, 0.0081, 0.0036, and 0.0009 L.

reaction of cyclohexylamine on Ni(111) and Ni(100) between 300 and 400 K in broad features.<sup>14,15</sup>

Desorption products other than cyclohexylamine and H<sub>2</sub> were similar to that of pyridine, including HCN and C<sub>2</sub>N<sub>2</sub>. Aniline was not specifically monitored, but benzene

was monitored, and it was not observed as a product. It is likely that the high dehydrogenation activity of the Pt(111) surface inhibited the desorption of any large intermediate dehydrogenation products. Cyclohexane is dehydrogenated on Pt(111) to form benzene, but mostly carbon accumulates on the surface due to the high

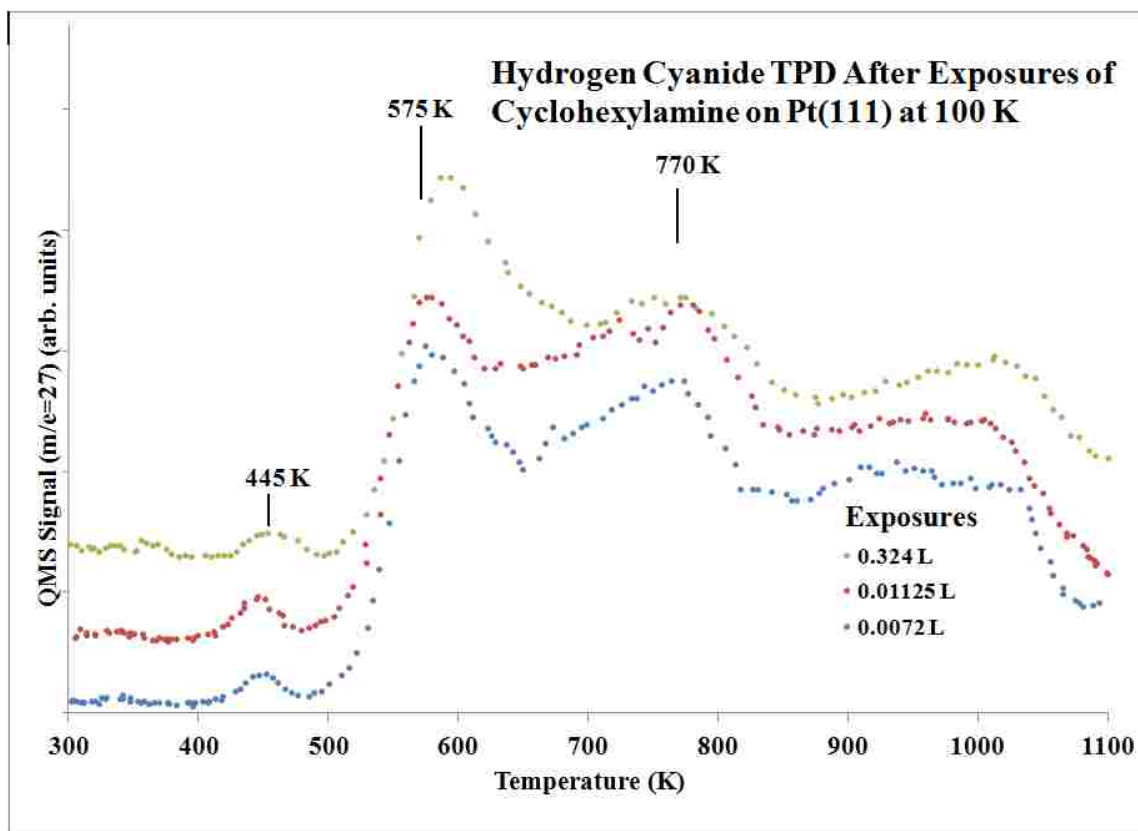


**Figure 4.5** HCN TPD after exposures of cyclohexylamine on Pt(111) at 100 K. The signal at 27 amu was monitored for cyclohexylamine exposures of 0.324, 0.01125, and 0.0072 L.

dehydrogenation activity of Pt(111).<sup>42</sup> The desorption barrier for HCN after cyclohexylamine exposures was compared to the pyridine experiments. Hydrogen cyanide desorbed with an  $E_{\text{des}}$  of 35 kcal/mol, compared to 37 kcal/mol at higher exposures, and 32 kcal/mol at lower exposure in the pyridine experiments. A larger barrier for HCN desorption after higher exposures is linked to an increased barrier for CN or HCN formation. Higher coverages cause competition for dehydrogenation active sites.

Hydrogen cyanide desorption from Pt(111) after cyclohexylamine exposures was consistently at higher temperatures than after pyridine exposures. Cyanogen desorption, with an  $E_{\text{des}}$  of 58 kcal/mol, was the same as that in the pyridine experiments, 56 kcal/mol. After cyclohexylamine exposures,  $\text{C}_2\text{N}_2$  desorbed in a single defined peak, which was comparable to the pyridine experiments.

As discussed before, dehydrogenation must occur in order for cyclohexylamine to

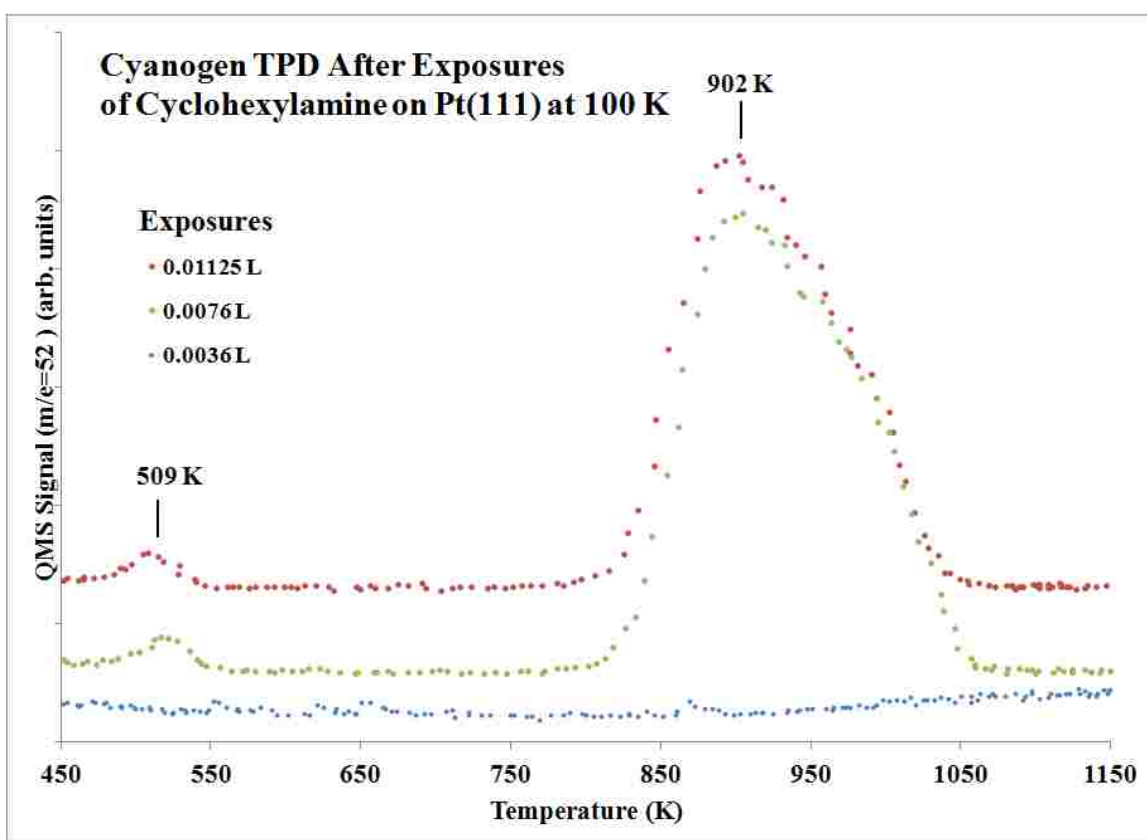
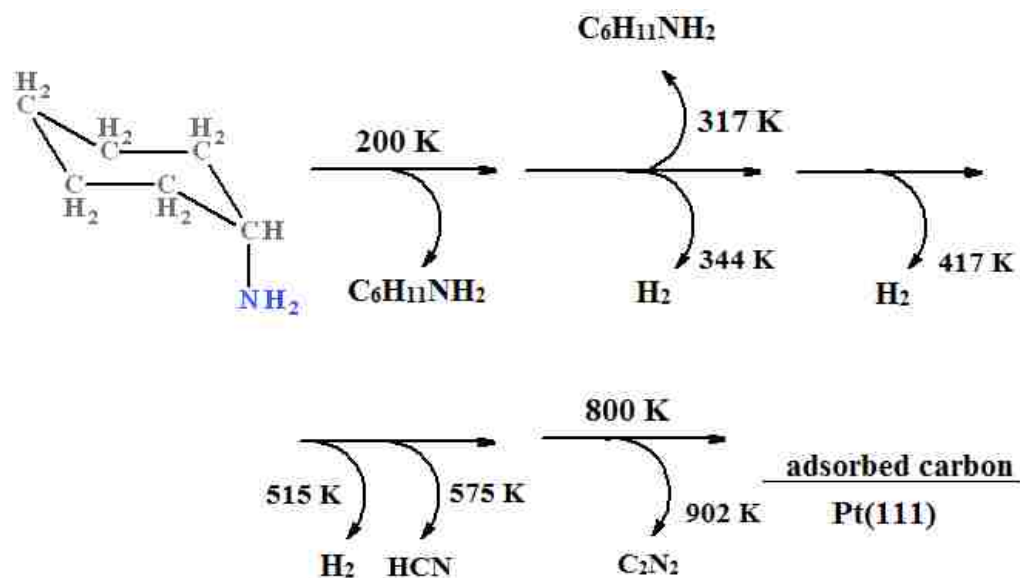


**Figure 4.6** Cyanogen ( $\text{C}_2\text{N}_2$ ) TPD after exposures of cyclohexylamine on Pt(111) at 100 K. The signal at 52 amu was monitored for cyclohexylamine exposures of 0.01125, 0.0076, and 0.0036 L.

strongly interact with the surface and lead to C-N bond cleavage. Desorption of HCN after cyclohexylamine adsorption, in contrast to pyridine, is not an indicator of C-N bond cleavage, because it is not necessary to break a C-N bond in cyclohexylamine to form

HCN. Therefore,  $E_{\text{des}}$  for HCN cannot be used to calculate the activation barrier for C-N bond cleavage. Ammonia desorption, which was observed between 300 and 500 K, indicates C-N bond cleavage in the TPD experiments for cyclohexylamine. The lowest peak desorption temperature for  $\text{NH}_3$  at 334 K corresponds to  $E_{\text{des}}$  of 20 kcal/mol, and this places an upper limit on the activation barrier for C-N bond cleavage because  $\text{NH}_3$  desorbs below this temperature from Pt(111) following  $\text{NH}_3$  adsorption.<sup>43</sup> A reaction scheme of cyclohexylamine on Pt(111) is shown in Scheme 4.1.



**Scheme 4.1** Decomposition pathway for cyclohexylamine on Pt(111)

#### 4.4 Conclusion

Cyclohexylamine adsorption and reaction was studied on Pt(111) using TPD. Molecular desorption was detected from both the multilayer and the monolayer at 187 and 341 K, respectively, corresponding to desorption activation energies of 11 and 20 kcal/mol. Cyclohexylamine that did not desorb decomposed on the surface to form desorption products of  $\text{H}_2$ , HCN,  $\text{C}_2\text{N}_2$ , and  $\text{NH}_3$ . Using the  $\text{NH}_3$  desorption temperature,

we calculated an upper limit on the activation barrier for C-N bond cleavage of 20 kcal/mol. Both cyclic and non-cyclic amines bond to metal surface via the N atom and dehydrogenation of amine hydrogens precedes C-H bond cleavage.

#### 4.5 References

1. Furimsky, E.; Massoth, F.; *Catal. Rev. Sci. Eng.* **2005**, *47*, 297-489.
2. Lewandowski, M.; Sarbak, Z. *Appl. Catal., B* **2008**, *79*, 313-322.
3. Meitzner, G.; Via, G.H.; Lytle, F.W.; Fung, S.C.; Sinfelt, J.H.; *J. Phys. Chem.* **1988**, *92*, 2925-2932.
4. Li, Y.-X.; Klabunde, J.; Davis, B.H.; *J. Catal.* **1991**, *128*, 1-12.
5. Haq, S.; King, D. A. *J. Phys. Chem.* **1996**, *100*, 16957-16965.
6. Grassian, V.H.; Muetterties, E.L.; *J. Phys. Chem.* **1986**, *90*, 5900-5907.
7. Johnson, A.L.; Muetterties, E.L.; Stöhr, J.; Sette, F.; *J. Phys. Chem.* **1985**, *89*, 4071-4075.
8. Lee, I.C.; Masel, R.I.; *J. Phys. Chem. B* **2002**, *106*, 368-373.
9. Gland, J.L.; Somorjai, G.A.; *Surf. Sci.* **1973**, *38*, 157-186.
10. Kliewer, C. J.; Somorjai, G. A. *Catal. Lett.* **2010**, *137*, 118-122.
11. Surman, M.; Bare, S.R.; Hofmann, P.; King, D.A.; *Surf. Sci.* **1987**, *179*, 243-253.
12. Connolly, M.; Somers, J.; Bridge, M.E.; Lloyd, D.R.; *Surf. Sci.* **1987**, *185*, 559-568.
13. Huang, S.X.; Fischer, D.A.; Gland, J.L.; *J. Vac. Sci. Technol. A* **1994**, *12*, 2164-2169.
14. Huang, S.X.; Gland, J.L.; *J. Phys. Chem.* **1996**, *100*, 13629-13635.
15. Huang, S.X.; Gland, J.L.; *J. Phys. Chem.* **1996**, *100*, 2206-2212.
16. Hwang, S.Y.; Seebauer, E.G.; Schmidt, L.D.; *Surf. Sci.* **1987**, *188*, 219-234.
17. Bridge, M.E.; Somers, J.; *Vacuum* **1988**, *38*, 317-320.
18. Chen, J.J.; Winograd, N.; *Surf. Sci.* **1995**, *326*, 285-300.
19. Kang, D.-H.; Trenary, M.; *Surf. Sci.* **2002**, *519*, 40-56.
20. Mudiyansele, K.; Trenary, M.; Meyer, R.J.; *J. Phys. Chem. C* **2008**, *112*, 3794-3799.
21. Chalker, S.; Haq, S.; Birtill, J.J.; Nunney, T.S.; Raval, R.; *Surf. Sci.* **2006**, *600*, 2364-2371.
22. Kelber, J.A.; Rogers, Jr., J.W.; Banse, B.A.; Koel, B.E.; *Appl. Surf. Sci.* **1990**, *44*, 193-204.
23. Erley, W.; Xu, R.; Hemminger, J.C.; *Surf. Sci.* **1997**, *389*, 272-286.

24. Kang, D.-H.; Chatterjee, B.; Herceg, E.; Trenary, M.; *Surf. Sci.* **2003**, *540*, 23-38.
25. Gland, J.L.; Somorjai, G.A.; *Adv. Coll. Interf. Sci.* **1976**, *5*, 205-243.
26. Huang, S.X.; Fischer, D.A.; Gland, J.L.; *Catal. Lett.* **1995**, *34*, 365-374.
27. Huang, S.X.; Fischer, D.A.; Gland, J.L.; *J. Phys. Chem.* **1996**, *100*, 10223-10234.
28. Schoofs, G.R.; Benziger, J.B.; *J. Phys. Chem.* **1988**, *92*, 741-750.
29. Narayanan, S.; Unnikrishnan, R.; Vishwanathan, V.; *Appl. Catal. A* **1995**, *129*, 9-19.
30. Mink, G.; Horváth, L.; *React. Kin. Catal. Lett.* **1998**, *65*, 59-65.
31. Vishwanathan, V.; Sajjad, S.M.; Narayanan, S.; *Indian J. Chem.*, **1991**, *30A*, 679-681.
32. Vishwanathan, V.; Narayanan, S.; *J. Chem. Soc., Chem. Commun.*, **1990**, 78-80.
33. Kishi, K.; Chinomi, K.; Inoue, Y.; Ikeda, S.; *J. Catal.* **1979**, *60*, 228-240.
34. Xu, X.; Friend, C.M.; *J. Vac. Sci. Technol. A* **1991**, *9*, 1599-1603.
35. Plank, R.V.; DiNardo, N.J.; Vohs, J.M.; *Surf. Sci. Lett.* **1995**, *340*, L971-L977.
36. Rockey, T.J.; Yang, M.; Dai, H.; *Surf. Sci.* **2005**, *589*, 42-51.
37. Solomon, J.L.; Madix, R.J.; Stöhr, J.; *Surf. Sci.* **1991**, *255*, 12-30.
38. Mudiyansele, K.; Trenary, M.; *Surf. Sci.* **2009**, *603*, 3215-3221.
39. Somers, J.S.; Bridge, M.E.; *Surf. Sci.* **1985**, *159*, L439-444.
40. Hoffmann, W.; Bertel, E.; Netzer, F.P.; *J. Catal.* **1979**, *60*, 316-324.
41. Lindquist, J.M.; Ziegler, J.P.; Hemminger, J.C.; *Surf. Sci.* **1989**, *210*, 27-45.
42. Xu, C.; Tsai, Y.-L.; Koel, B.E.; *J. Phys. Chem.* **1994**, *98*, 585-593.
43. Gland, J.L.; Kollin, E.B.; *Surf. Sci.* **1981**, *104*, 478-490.

## Chapter 5: Adsorption and reaction of piperidine on Pt(111) and Sn/Pt(111) Surface Alloys

### 5.0 Abstract

Adsorption and reaction of piperidine ( $C_5H_{10}NH$ ) was studied by temperature programmed desorption (TPD) on the Pt(111) and Sn/Pt(111) alloy surfaces. On Pt(111), some reversible desorption was observed at 293 K from the monolayer and at 172 K from the multilayer. Decomposition of piperidine produced major products of hydrogen ( $H_2$ ), hydrogen cyanide (HCN), cyanogen ( $C_2N_2$ ), and pyridine ( $C_5H_5N$ ) on Pt(111). Pyridine was a product of dehydrogenation and had a higher heat of adsorption and desorption temperature than piperidine. Hydrogen desorbed over a large range of temperatures in well-defined peaks indicative of step-wise dehydrogenation of piperidine and subsequent intermediates. Hydrogen cyanide desorbed at high temperatures and is a marker for C-N bond cleavage. Cyanogen desorption occurred in a broad peak at 917 K, above the temperature of removal of all hydrogen from surface species. Adsorption of piperidine was slightly weakened on Sn/Pt(111) alloy surfaces compared to the Pt(111) surface. Reaction products from piperidine on the Pt and PtSn surfaces were similar in identity, but dehydrogenation products desorbed at higher temperatures on the alloy surface.

### 5.1 Introduction

Piperidine ( $C_5H_{10}NH$ ) is the saturated form of pyridine, as illustrated in Figure 5.1. Piperidine is frequently compared to pyridine in hydrodenitrogenation (HDN) studies.<sup>1</sup> In HDN, hydrogenation is generally the first step in removal of nitrogen from an aromatic species, so understanding the adsorption and reaction of the saturated form of pyridine in addition to pyridine adsorption and reaction is important to elucidate the reaction pathway of these molecules.<sup>1</sup>

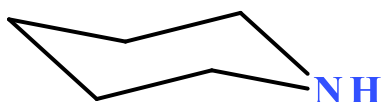


**Figure 5.1**  
**Structure**  
**of piperidine**

While supported HDN catalysts are typically composed of combinations of nickel, molybdenum, and cobalt, a recent study showed the superior activity of a PtSn/SiO<sub>2</sub> catalyst for simultaneous HDN and hydrodesulfurization (HDS).<sup>2</sup> This thesis is focused on the adsorption and reaction of nitrogen-containing cyclic hydrocarbons on a Pt(111) single

crystal, and in this chapter, new information regarding the adsorption and reaction of piperidine on both Pt(111) and Sn/Pt(111) surface alloys is presented from temperature programmed desorption (TPD) studies. Surface science studies such as these on single crystals are helpful in identifying the fundamental surface chemistry between metal surfaces and adsorbates, which can then be applied to understand catalytic reactions on supported catalysts.

Limited surface science data is available for the adsorption and reaction of piperidine. A recent paper reported the study of pyridine hydrogenation on the Pt(111) and Pt(100) surfaces using sum frequency generation (SFG) vibrational spectroscopy.<sup>3</sup> Piperidine was determined to be adsorbed via the nitrogen atom prior to desorption from Pt(111). Vibrational frequencies indicative of piperidine were not seen above 350 K, and the adsorbed surface species were reported to have been disordered after being warmed to higher temperatures. On Ni(100), piperidine adsorption was compared to pyridine and other organonitrogen molecules.<sup>4</sup> Desorption products were observed at 250, 485, and 660 K. Products from piperidine reaction on Ni(100) were reported to be ethene (C<sub>2</sub>H<sub>4</sub>) and H<sub>2</sub> at 660 K. Other desorption and reaction products were similar to that of pyridine, which included pyridine (C<sub>5</sub>H<sub>5</sub>N), piperidine (C<sub>5</sub>H<sub>10</sub>NH), methane (CH<sub>4</sub>), hydrogen cyanide (HCN), and methylamine (CH<sub>3</sub>NH<sub>2</sub>). The major difference between the reaction of pyridine and piperidine was that more H<sub>2</sub> desorption was observed at low temperature, which can be expected since piperidine has six additional hydrogen atoms per molecule, and the products would also be expected to be the same if pyridine is an intermediate in piperidine decomposition.



Although piperidine has not been extensively studied on single crystal surfaces, it can be compared to other saturated cyclic molecules, such as cyclohexane. Cyclohexane ( $C_6H_{12}$ ) adsorption on Pt(111) yields a significant amount of hydrogen desorption from the stepwise formation of cyclohexene and benzene, and a large carbon accumulation occurs during TPD due to benzene dehydrogenation reactions.<sup>4,5</sup> The desorption of  $C_6H_{12}$  from Pt(111) corresponds to a desorption activation barrier of 14 kcal/mol.<sup>5</sup> Piperidine differs from cyclohexane in structure in that it contains an electronegative heteroatom, which causes a tilted adsorption geometry, as was observed on Pt(111) previously by SFG experiments.<sup>3</sup> Bonding of cyclohexane is weaker than benzene on Pt(111), and some cyclohexane reversibly adsorbs.<sup>4,5</sup> Benzene bonds more strongly to the surface due to  $\pi$  interactions with the surface, and no desorption of benzene was observed in TPD after small benzene exposures.<sup>4</sup>

As was reported in Chapter 3 and in the previous literature therein, pyridine partially reversibly adsorbs on Pt(111), just as benzene does. At low coverage, pyridine adopts an adsorption geometry with the ring parallel to the surface, as does benzene, but at higher coverage the adsorption geometry shifts to a more vertical position due to using the lone pair of electrons on the nitrogen atom to form the chemisorption bond.<sup>6-10</sup> The desorption activation barrier energy for  $C_6H_6$  from Pt(111) is 30 kcal/mol.<sup>5</sup>

The alloying of Sn in the Pt(111) surface has led to higher activity and less carbon formation in surface science studies of hydrocarbon surface reactions.<sup>11-14</sup> For example, in the reaction of acetylene, a coke precursor and thus an indicator for resistance to coking, on Sn/Pt(111) surface alloys, much less carbon was formed in TPD studies compared to Pt(111).<sup>12</sup> The activity for hydrogenation of crotonaldehyde was

approximately twice as high on (2x2)-Sn/Pt(111) alloy surfaces than on Pt(111).<sup>14</sup> Also, Sn decreased the reactivity of the surface in the adsorption and reaction of cyclohexanone.<sup>15</sup> Inhibition of decomposition pathways, e.g. extensive dehydrogenation, can alter selectivity of a surface for desired products.

In this chapter, we report on studies of piperidine on both the Pt(111) surface and an alloyed Sn/Pt(111) surface by TPD to identify dehydrogenation products and activation barriers for surface processes. We will also compare these results to the chemistry of other nitrogen-containing cyclic molecules, pyridine and cyclohexylamine, on Pt(111).

## 5.2 Experimental Methods

Piperidine (Alfa Aesar, 99%) was placed in a dosing test tube with 4Å molecular sieves (Aldrich, 3.2 mm). The molecular sieves were baked in an oven for 2.5 hrs at 175 °C, stored in a desiccator until they were cooled to room temperature, and then placed in the dosing test tube prior to filling with piperidine. Piperidine was stored in a bottle which required a syringe to remove the liquid. A metal syringe was baked in an oven and then stored in a desiccator prior to being used for the transfer. The piperidine was degassed by three freeze-pump-thaw cycles. Teflon ferrules and Swagelok™ fittings were used to connect the dosing test tube to the gas handling line because piperidine vapor caused deterioration of the O-rings in UltraTorr™ connectors.

TPD experiments were carried out in a manner similar to the process used for pyridine and cyclohexylamine experiments, and this process was described in Section 2.5. Corrections in the stated exposures were not made for ion-gauge sensitivities. The Pt(111) and Sn/Pt(111) alloy surfaces were prepared as described in Sections 2.3 and 2.4.

In TPD experiments following piperidine exposures on Pt(111) and Sn/Pt(111) alloy surfaces, no N<sub>2</sub>, CH<sub>4</sub>, or benzene were observed to desorb, even though signals at 14, 26, 27, 28, and 78 amu were monitored to detect these molecules.

### 5.3 Results and Discussion

#### 5.3.1 Piperidine Adsorption on Pt(111)

After small piperidine exposures, piperidine desorption from the Pt(111) surface (Figure 5.2) was observed in a peak at 293 K, as monitored by the 85 amu signal. Thus, piperidine adsorption is at least partially reversible even at low coverages. This peak is associated with desorption of chemisorbed piperidine. This peak broadens to lower temperatures with increasing coverage, and another peak was seen at 226 K, but it is not clear if this peak arises from the chemisorbed monolayer or second layer. A similar lower-temperature shoulder was observed in a study of cyclohexylamine on Ni(111), but no explanation was provided for this feature.<sup>16</sup> Piperidine desorption in a peak at 165-172 K comes from the multilayer, as was established by checking that this peak did not saturate in signal at much higher exposures.

The main desorption products in addition to piperidine seen in TPD spectra from the Pt(111) surface after piperidine exposures were H<sub>2</sub> (2 amu), pyridine (79 amu), cyanogen (52 amu), HCN (27 amu), and NH<sub>3</sub> (17 amu). Figure 5.3 shows a combined plot of piperidine, H<sub>2</sub>, HCN, and C<sub>2</sub>N<sub>2</sub> TPD spectra. In this figure, as in Figure 5.2, piperidine desorbs in a broad feature that peaks at 293 K. Piperidine desorption stops with the onset of H<sub>2</sub> desorption due to dehydrogenation. Hydrogen desorbs in three distinct peaks at 315, 402 and 490 K, and then a broad feature that extends to 800 K. The first peak at 315 K is due to the loss of 6 H atoms/molecule needed to form pyridine on

the surface. Pyridine desorption occurs at the same temperature, indicating the first H<sub>2</sub> desorption peak leads to pyridine as a stable intermediate, which desorbs upon formation.

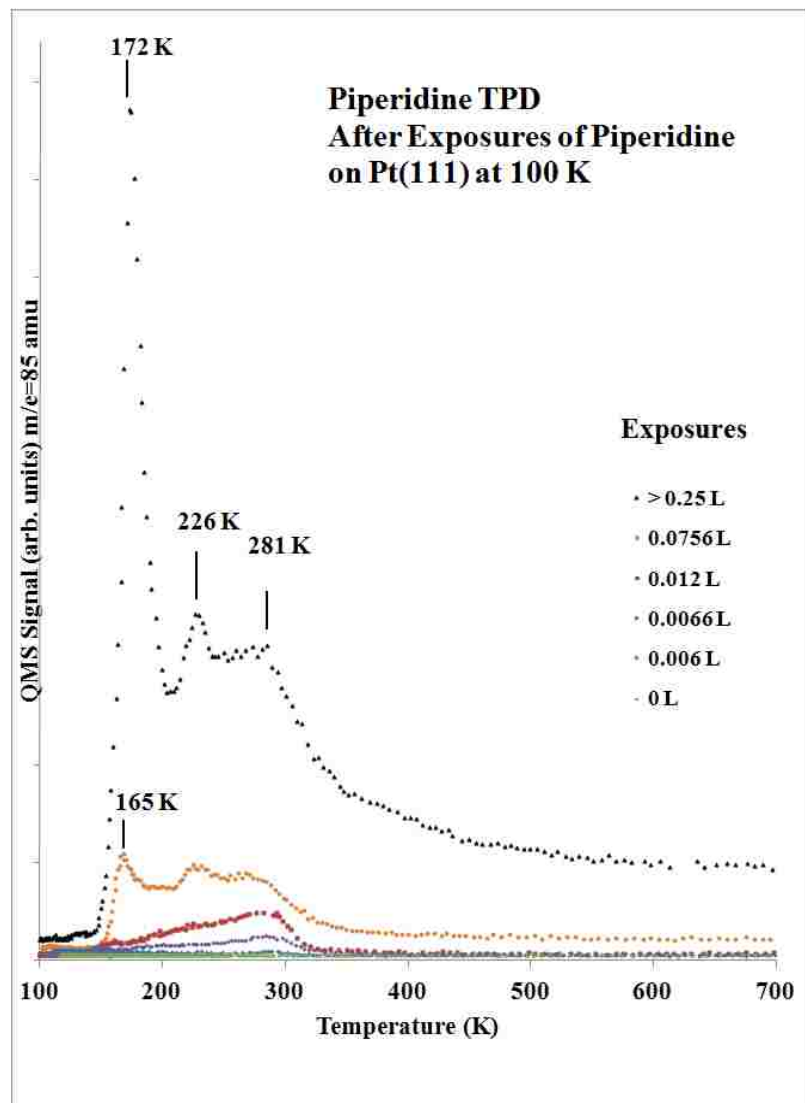


**Figure 5.2** Piperidine TPD after exposures of piperidine on Pt(111) at 100 K of >0.25, 0.0756, 0.012, 0.0066, 0.006, and 0 L.

The desorption of pyridine as a dehydrogenation product is assigned to a reaction-rate limited process, since desorption of pyridine from Pt(111) after pyridine adsorption occurred at 247 K. The second and third peaks at 402 and 490 K correspond to the loss H atoms from ring carbons during pyridine decomposition. C-C bond cleavage in the ring

occurs above 490 K, since the start of HCN desorption was observed, leading to a peak at 539 K with a broad feature to higher temperatures. The 27 amu signal is still observed, which could be due to H<sub>2</sub> outgassing from the sample holder, after the crystal was warmed past 800 K. This additional hydrogen facilitated further HCN desorption by reacting with remaining CN fragments on the surface. Cyanogen desorbs in a broad peak

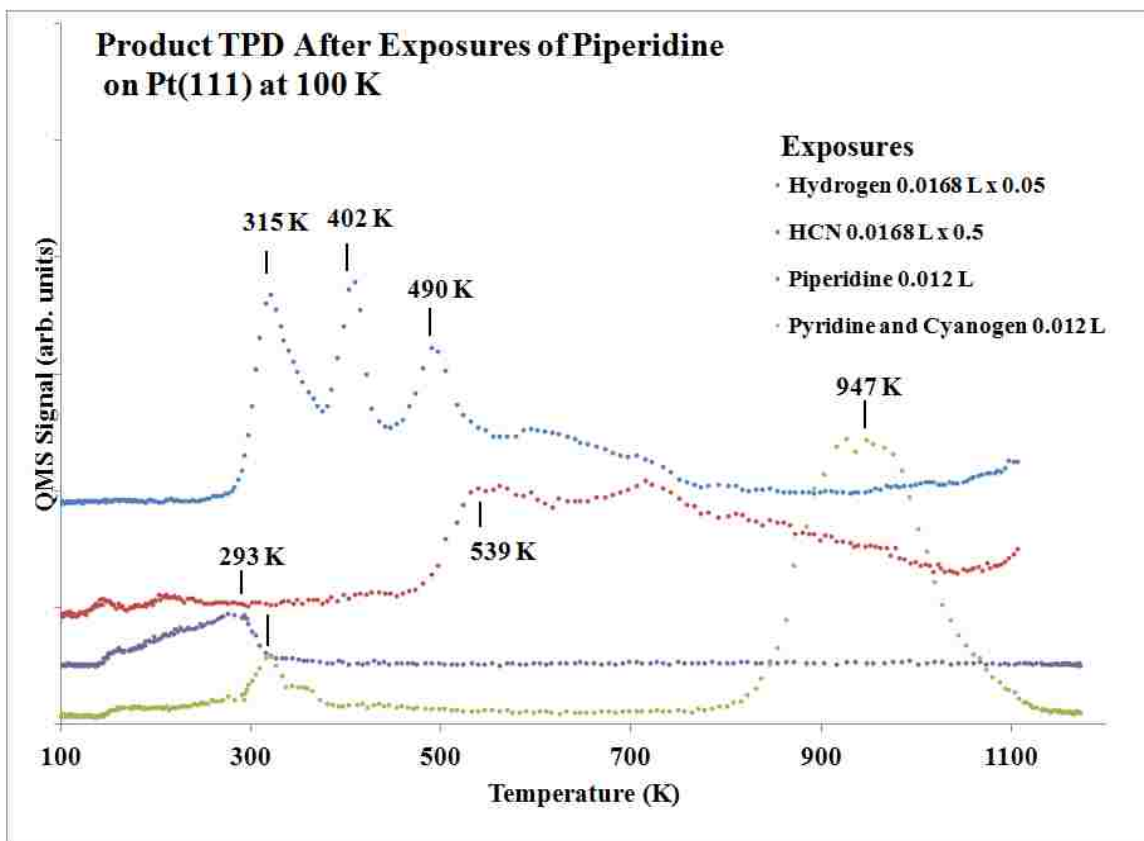


**Figure 5.3** Product TPD after exposures of piperidine on Pt(111) at 100 K. Desorption of H<sub>2</sub> (2 amu) and HCN (27 amu), was monitored after a piperidine exposure of 0.0168 L. Desorption of piperidine (85 amu), pyridine and C<sub>2</sub>N<sub>2</sub> (both monitored by 52 amu) was monitored after a piperidine exposure of 0.0012 L.

at 947 K. Desorption observed for 52 amu above 700 K was determined to be due to C<sub>2</sub>N<sub>2</sub> by simultaneous monitoring of CN (26 amu), a fragment ion of C<sub>2</sub>N<sub>2</sub>.

The H<sub>2</sub> desorbing from the Pt(111) surface as seen in the H<sub>2</sub> TPD spectra (Figure 5.4) is indicative of extensive dehydrogenation of piperidine. The H<sub>2</sub> desorption profiles are similar to those from both the reaction of pyridine and cyclohexylamine, where three main peaks were observed in the dehydrogenation of these molecules. These three well-

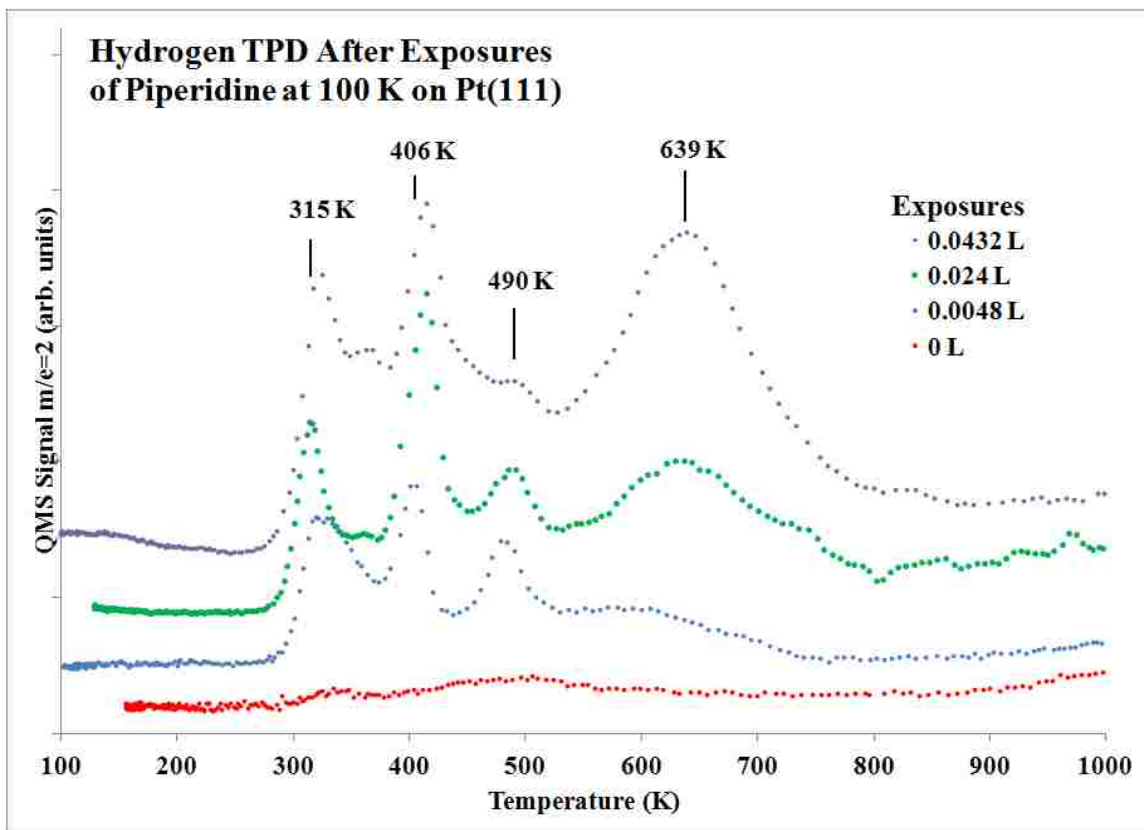


**Figure 5.4** Hydrogen (H<sub>2</sub>) TPD after 0.0432, 0.024, 0.0048, and 0 L exposures of piperidine on Pt(111) at 100 K.

defined peaks indicate sequential dehydrogenation of piperidine and subsequent reaction intermediates. Also, this agrees with results from the reaction of n-methylaniline reaction on Pt(111), where H<sub>2</sub> desorption was also observed in three main peaks.<sup>17</sup>

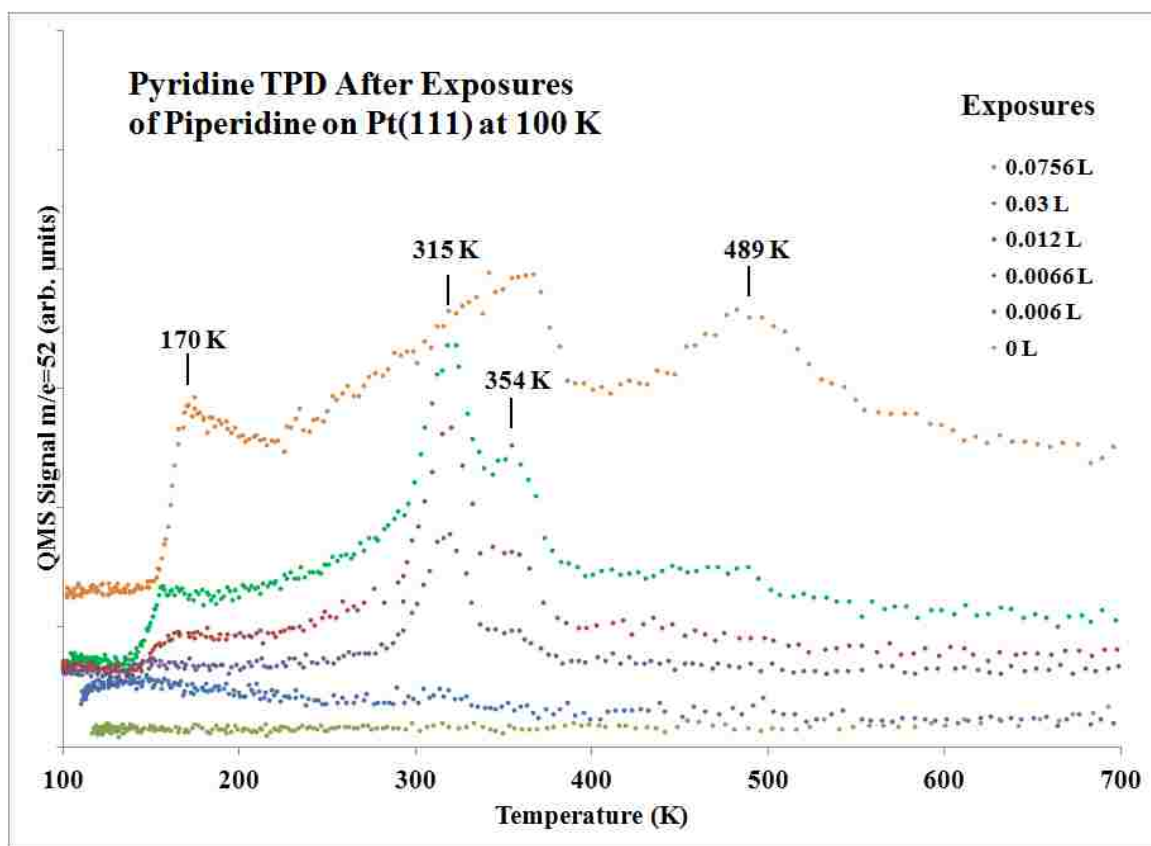


**Figure 5.5** Pyridine TPD after exposures of piperidine on Pt(111) at 100 K of 0.0756, 0.03, 0.012, 0.0066, 0.006, and 0 L.

The desorption of pyridine after exposures of piperidine was observed at 315 and 354 K from the Pt(111) surface (Figure 5.5). The parent peak at 79 amu was monitored simultaneously with 52 amu to confirm pyridine as a desorbed product. The signal at 52 amu was conveniently used to follow both the desorption of  $C_2N_2$  and pyridine. Desorption above 700 K for 52 amu was determined to be due to cyanogen, by simultaneously monitoring 26 amu, and therefore, this figure only shows desorption at 52 amu up to 700 K. Desorption of pyridine proves that dehydrogenation of piperidine proceeds via formation of a pyridine intermediate.

Figure 5.6 shows HCN TPD profiles after piperidine exposures on the Pt(111) surface. At lower exposures, an HCN desorption peak appeared at 531 K, which shifted slightly to 561 K with higher exposures. The long desorption tail extending to higher

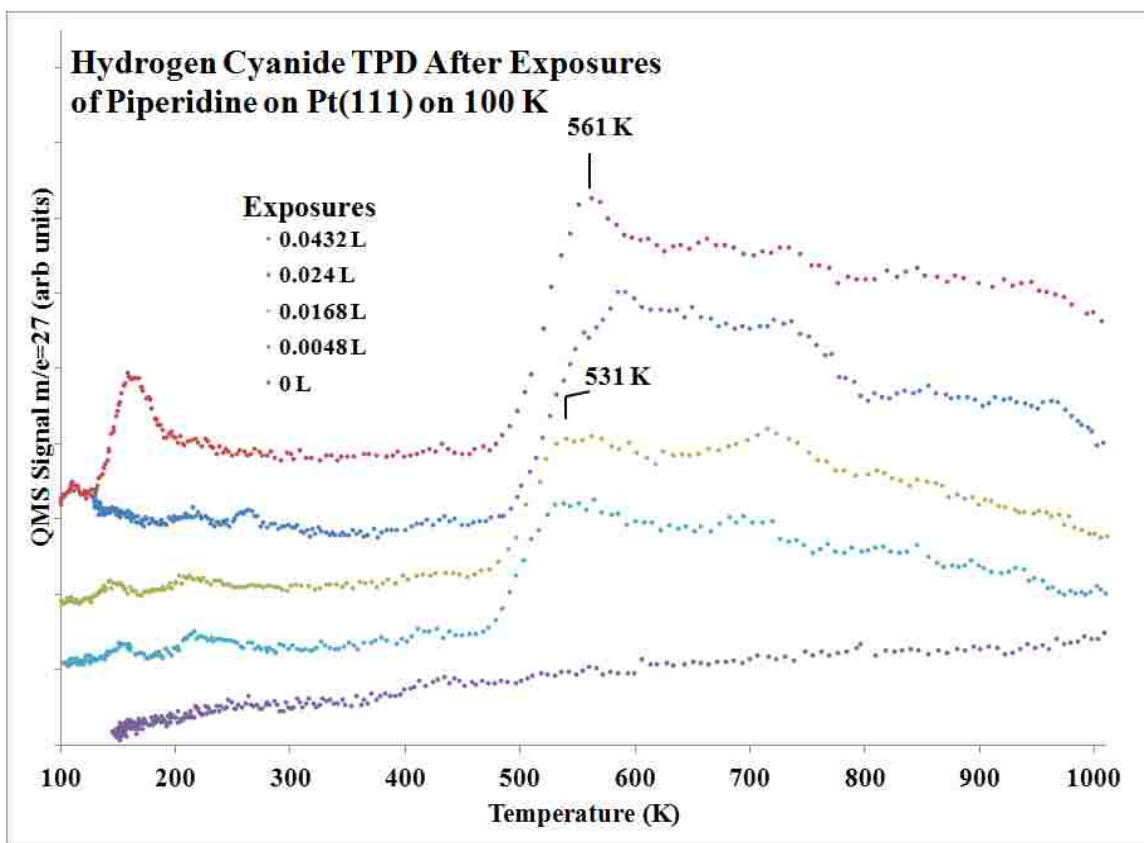


**Figure 5.6** Hydrogen cyanide (HCN) TPD after exposures of piperidine on Pt(111) at 100 K of 0.0432, 0.024, 0.0168, 0.0048, and 0 L.

temperatures is difficult to understand, but as stated before, can be attributed to outgassing of the sample holder. The HCN desorption profile was the same as we observed for the reaction of pyridine and cyclohexylamine on Pt(111), in that a large, broad desorption feature was observed above 500 K. The desorption of HCN from the reaction of both pyridine and cyclohexylamine both produced a low-temperature peak at 439 and 445 K, respectively, which were assigned to direct desorption of HCN after dehydrogenation on the surface.<sup>16</sup> Reaction of piperidine on Pt(111) does not produce a



similar low-temperature direct HCN desorption peak. Instead, all HCN desorption occurs at in a large, broad feature above 500 K.

The onset of  $C_2N_2$  desorption (Figure 5.7) occurs above 800 K, the temperature at which all H is removed from the surface via  $H_2$  or HCN desorption. Cyanogen desorption after lower piperidine exposures occurs in a broad peak at 917 K, and this shifts to 992 K with a broad tail at higher exposures. Cyanogen desorption in a fairly symmetrical desorption peak derives from second-order desorption kinetics resulting from the recombination of two  $CN_{ads}$  fragments formed by dehydrogenation of surface intermediates.<sup>18,19</sup> Desorption of  $C_2N_2$  after reaction of symdimethylhydrazine and HCN on Pt(111) has been assigned to associative desorption.<sup>18,19</sup>

Desorption of piperidine from the physisorbed multilayer occurred on the Pt(111) surface near 172 K, corresponding to an  $E_{des}$  of 8 kcal/mol. Desorption of piperidine from the monolayer occurred in a peak 281 K, corresponding to  $E_{des}$  of 15 kcal/mol. At 300 K, hydrogen desorption from the dehydrogenation of adsorbed piperidine commenced. Desorption of hydrogen continued until temperatures near 800 K. Dehydrogenation of piperidine on Pt(111) produced pyridine, some of which desorbed in peaks at 315 and 354 K, corresponding to  $E_{des}$  of 17 and 20 kcal/mol, respectively. These  $E_{des}$  both correspond to reaction rate-limited processes, since pyridine desorbs from Pt(111) at 247 K, as evidenced in Chapter 3. This result is consistent with earlier vibrational studies on Pt(111) that showed no evidence of pyridine above 350 K.<sup>3</sup> Above 354 K, further dehydrogenation of surface intermediates continued, allowing more desorption of  $H_2$  and, eventually, HCN and  $C_2N_2$ .

Desorption of HCN occurred at 531 K, corresponding to  $E_{\text{des}}$  of 32 kcal/mol, which corresponds to the activation barrier for cleavage of the C-N bond, for HCN desorption from piperidine decomposition. HCN desorption from HCN dosing occurs at

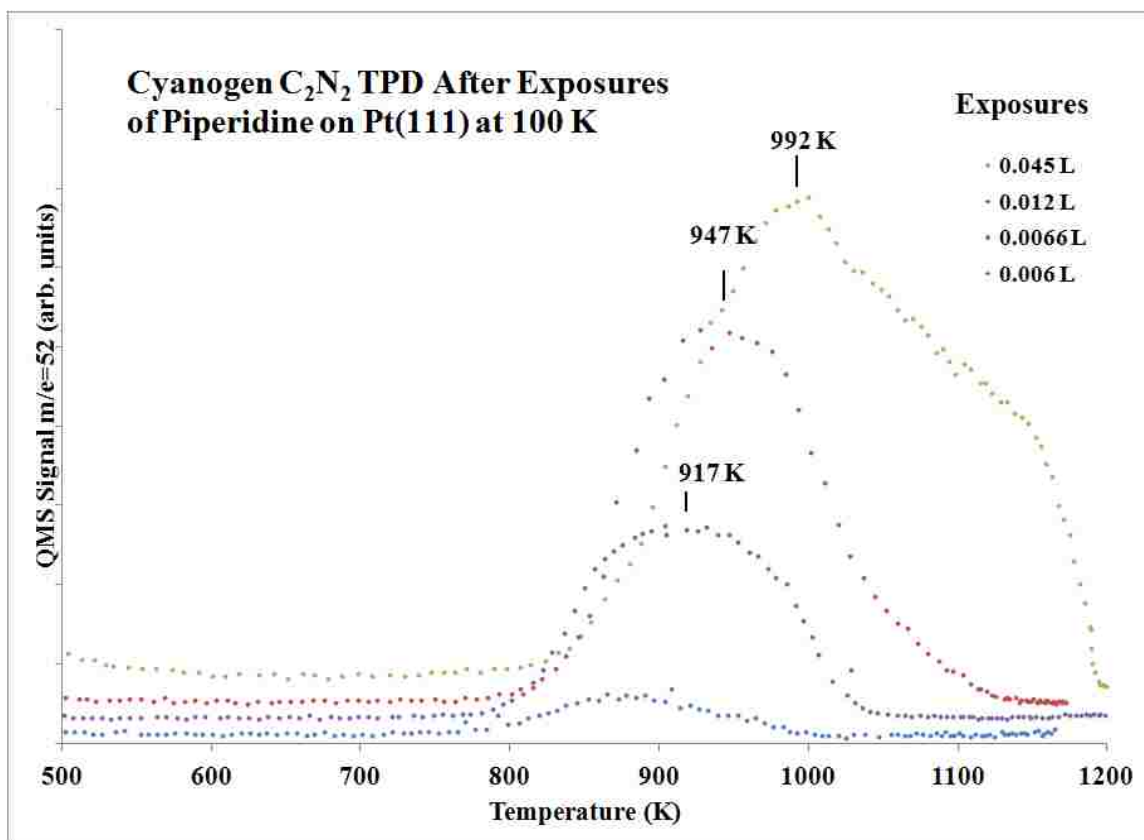
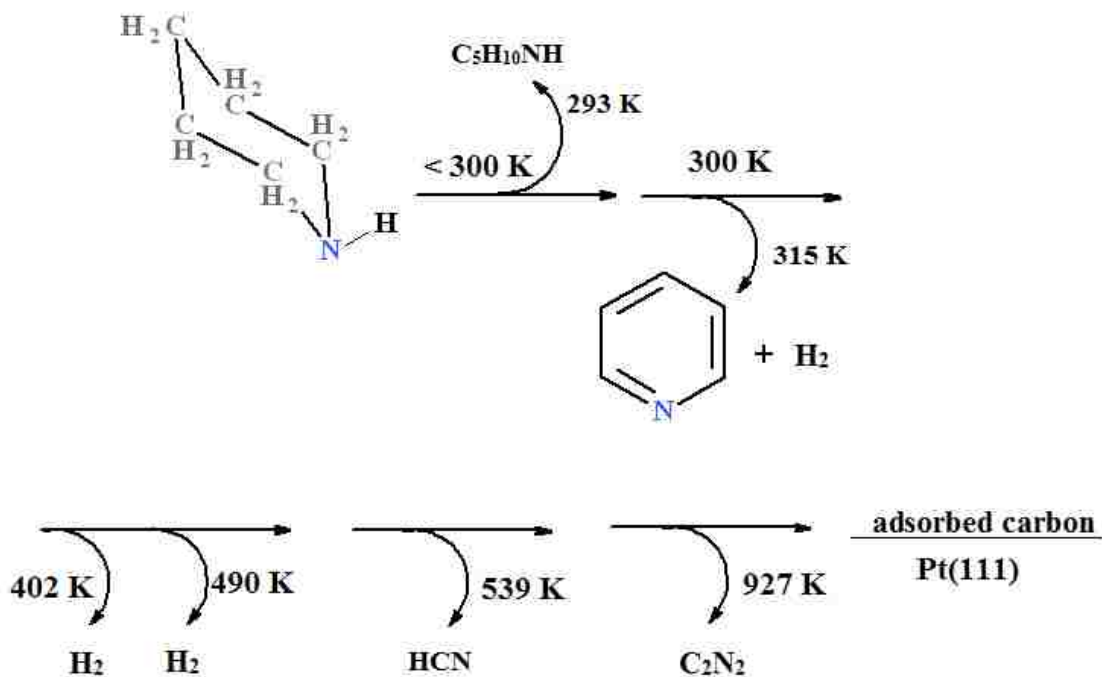


**Figure 5.7** Cyanogen ( $C_2N_2$ ) TPD after exposures of piperidine on Pt(111) at 100 K of 0.045, 0.012, 0.0066, and 0.006 L.

470 and 510 K,<sup>18</sup> where the lower desorption peak is from direct desorption and the higher desorption peak was assigned to recombinative desorption. As soon as  $CN_{\text{ads}}$  is formed, hydrogenation of  $CN_{\text{ads}}$  by  $H_{\text{ads}}$  occurs to produce HCN desorption.

Cyanogen desorption in a peak at 947 K corresponds to an  $E_{\text{des}}$  of 58 kcal/mol, which is the activation energy for C-C bond formation in the associative desorption of  $C_2N_2$ . When no hydrogen atoms remained to combine with  $CN_{\text{ads}}$ , associative desorption

of  $C_2N_2$  was observed. This associative desorption is consistent with what was observed



**Scheme 5.1** Decomposition pathway for piperidine on Pt(111)

for pyridine and cyclohexylamine on Pt(111) in this thesis. Scheme 5.1 displays piperidine decomposition reactions on Pt(111) after piperidine adsorption.

### 5.3.2. Piperidine Adsorption on Sn/Pt(111) Surface Alloys

Piperidine was also adsorbed on an alloyed Sn/Pt(111) surface to analyze the effect of Sn on the adsorption and reaction of piperidine. Low energy electron diffraction (LEED) patterns obtained for the surface studied indicated that it was a mixture of the  $2 \times 2$  and the  $\sqrt{3}$  surface alloy phases. Figure 5.8 shows the comparison of piperidine desorption from monolayer coverages on both the Pt(111) and the Sn/Pt(111) alloy surfaces. Two TPD spectra were obtained from the alloy surface after 0.09 and a 0.0135 L piperidine exposures, so TPD spectra with similar exposures on the Pt(111) surface (0.0756 L and 0.012 L) were chosen for comparison. Desorption from the Pt(111)

surface occurred at 268 K and 290 K. Desorption from the surface alloy occurred at 251 and 259 K. So both of the exposures on the Pt(111) surface caused desorption peaks higher than the two exposures on the alloy surface. Relative amounts of decomposition

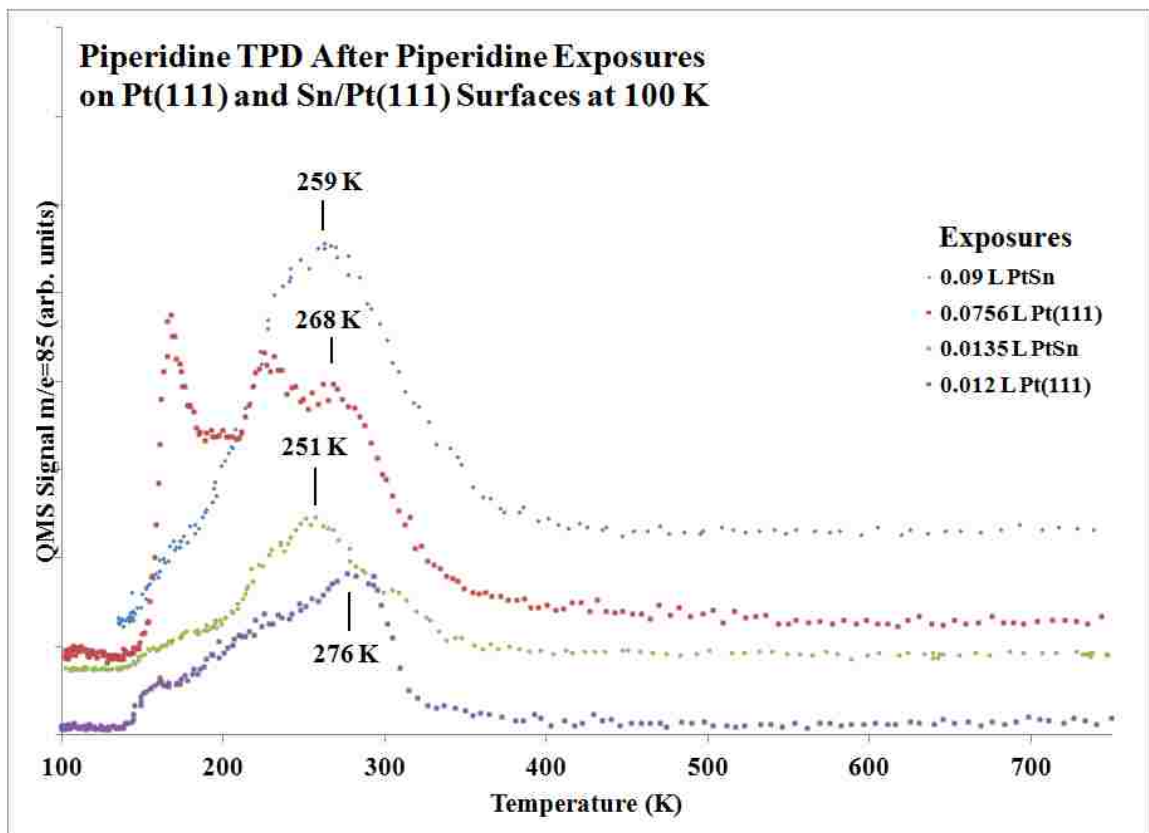


**Figure 5.8** Piperidine TPD after exposures of piperidine on Pt(111) and Sn/Pt(111) surfaces at 100 K. This figure shows spectra obtained after a low-exposure and a high-exposure dose of piperidine on Pt(111) and Sn/Pt(111) alloy surfaces. Piperidine exposures on Pt(111) were 0.0012 and 0.0756 L, and exposures on the Sn/Pt(111) surface alloy were 0.0135 and 0.09 L.

on the surface alloys and on Pt(111) could not be determined.

At the higher exposure, there was a difference in desorption temperature of 9 K, corresponding to a difference in  $E_{\text{des}}$  of 0.6 kcal/mol. At the lower exposures, there was a difference in desorption temperature of ~39 K, which corresponds to a change in  $E_{\text{des}}$  of 3

kcal/mol. These differences in desorption temperatures indicate that Sn alloyed with Pt in the surface only weakens slightly the strength of the interaction of piperidine with the surface. This result is expected because a decrease in desorption temperature was observed for other molecules such as cyclohexane, cyclohexadiene, and benzene when reacted on the PtSn alloy surfaces.<sup>5,24</sup>

Desorption products from the reaction of piperidine on the PtSn surface alloy were the same as was observed on Pt(111), including piperidine, pyridine, H<sub>2</sub>, HCN, and C<sub>2</sub>N<sub>2</sub>. Desorption temperatures, however were slightly higher for the dehydrogenation products of H<sub>2</sub>, HCN, and C<sub>2</sub>N<sub>2</sub>. These results are not consistent with other studies, in that usually dehydrogenation activity diminishes on the alloy surfaces and desorption of products due to surface reactions shifts to lower temperatures.<sup>5,24</sup> The higher desorption temperature for H<sub>2</sub> desorption is consistent with an increase from Pt(111) to the 2×2 alloy in the dehydrogenation of 1,3-cyclohexadiene.<sup>24</sup> The desorption temperature increased from 280 and 315 K on Pt(111) to 335 K on the 2×2 surface. In the reaction of piperidine, H<sub>2</sub> desorbed in the first two peaks at 315 K and 406 K on Pt(111), and at 380 and 479 K on the surface alloy. Adsorbed cyclohexyl on Pt(111) and Sn/Pt(111) surface alloys also showed an increase in the desorption temperature of H<sub>2</sub> from dehydrogenation from the Pt(111) surface to the 2×2 surface.<sup>5</sup>

### 5.3.3. Comparison of Pyridine, Cyclohexylamine and Piperidine Adsorption on Pt(111)

Figure 5.9 shows the comparison of pyridine, cyclohexylamine and piperidine desorption after monolayer adsorption of these molecules on Pt(111) at 100 K. The trend in desorption peak temperatures indicates the trend in adsorption strengths for these

molecules. Cyclohexylamine adsorbs with the highest strength (21 kcal/mol), followed by piperidine (17 kcal/mol), and then pyridine (15 kcal/mol). Typically, aromatic molecules adsorb more strongly to the Pt(111) surface than saturated molecules, so pyridine bonding with the weakest adsorption energy does not make sense at first glance. However, pyridine bonding strongly via the aromatic ring decomposes and does not desorb, while the desorbing pyridine molecules are those bonding to the surface via the

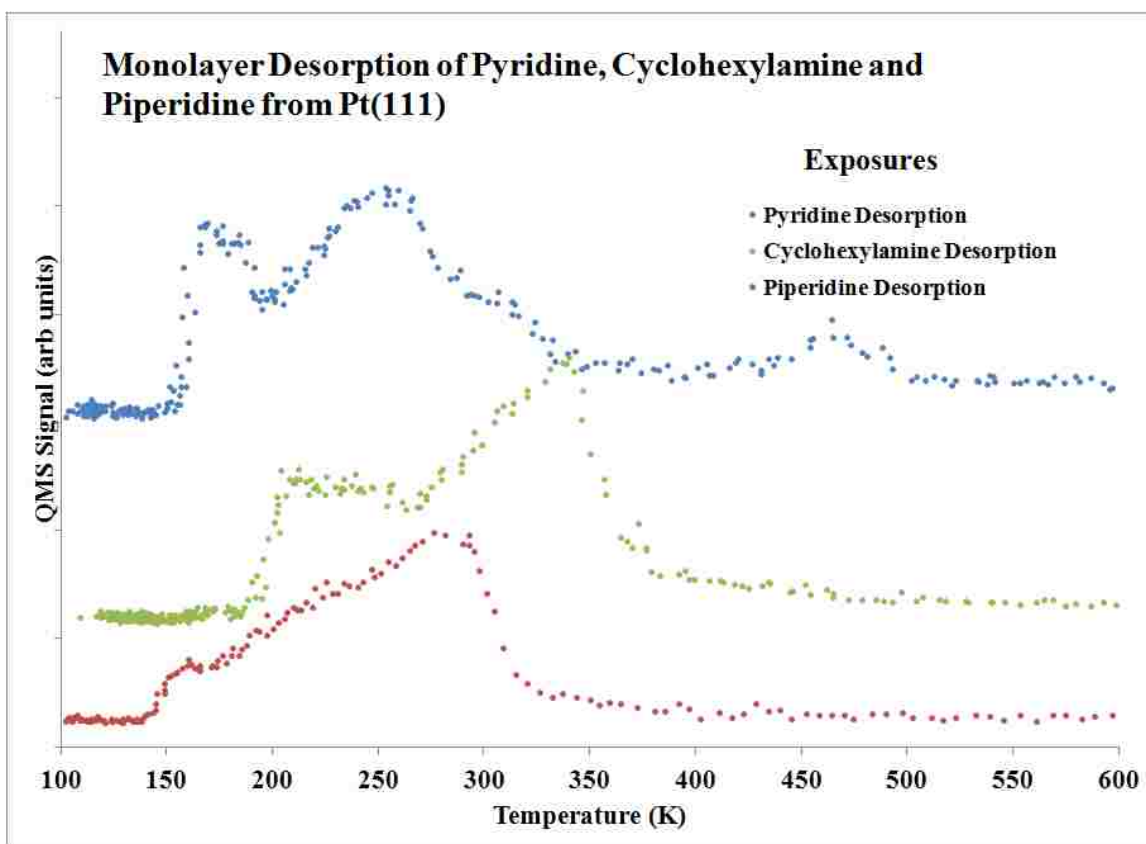


**Figure 5.9** TPD of monolayer molecular desorption of pyridine, cyclohexylamine, and piperidine from Pt(111).

nitrogen atom. Since the saturated molecules also bond to the surface via the N atom, the adsorption energies are quite similar.

It is also useful to compare adsorption of smaller amines, such as methylamine, dimethylamine and trimethylamine, on Pt(111), which indicate that the number of carbon

atoms bound to the nitrogen does not affect adsorption strength.<sup>25-27</sup> For these smaller amines, methylamine desorbs at 380 K, dimethylamine does not desorb from the chemisorbed state, and trimethylamine desorbs at 291 K from Pt(111). These desorption temperatures correspond to desorption activation barriers of 24 and 18 kcal/mol, for methylamine and trimethylamine, respectively. There is no trend in desorption activation energy for these simple primary, secondary and tertiary amines to connect with surface reactions.

Figure 5.10 compares H<sub>2</sub> desorption after approximate monolayer exposures of

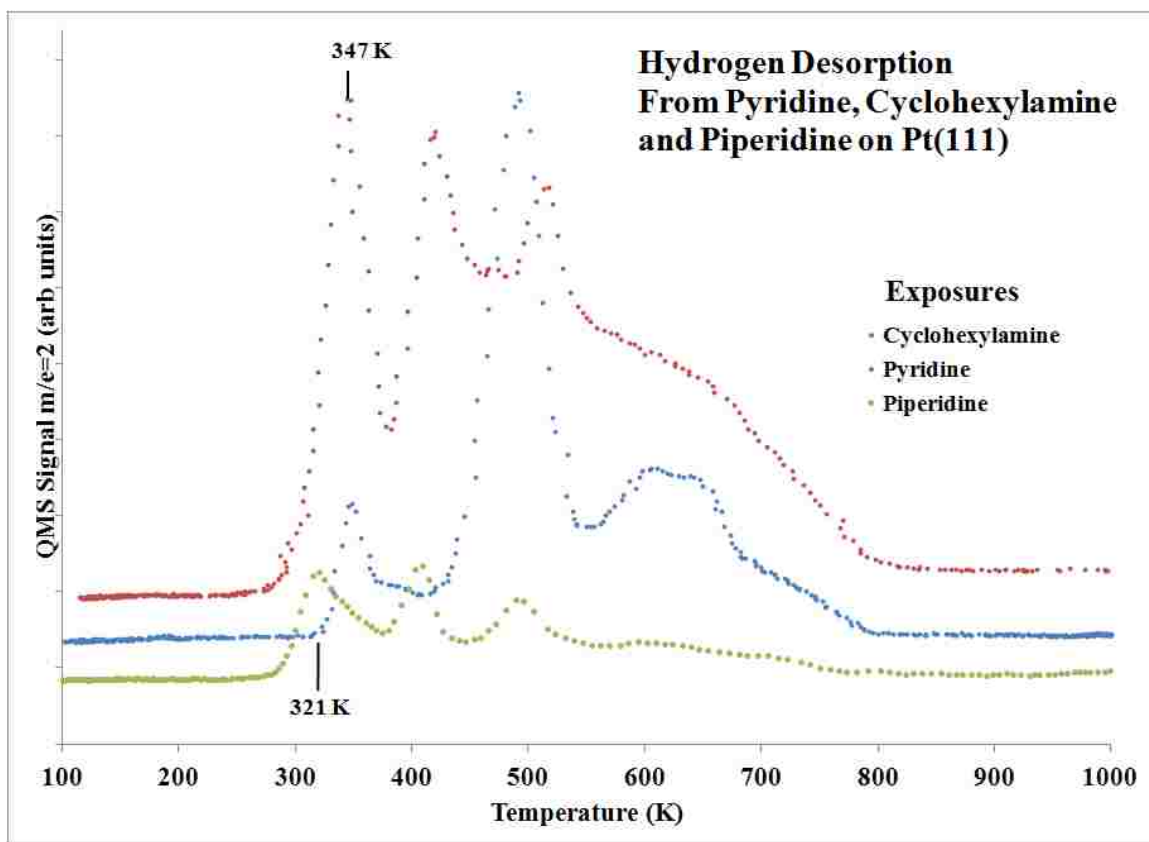


**Figure 5.10** H<sub>2</sub> TPD after monolayer exposures of pyridine, cyclohexylamine, and piperidine on Pt(111) at 100 K.

pyridine, cyclohexylamine and piperidine on the Pt(111) surface at 100 K.

Cyclohexylamine and piperidine reaction on Pt(111) both cause H<sub>2</sub> desorption near 300

K, due to low-temperature dehydrogenation to produce desorption rate limited peaks at 321-347 K. Piperidine eventually goes through a stable pyridine intermediate, but cyclohexylamine does not yield any large desorption products, such as aniline or benzene, during dehydrogenation.

Hydrogen desorption for the saturated molecules occurred in three main peaks, which is assigned to stepwise dehydrogenation of the molecules. Both cyclohexylamine and piperidine dehydrogenation commence at lower temperatures compared to H<sub>2</sub> TPD after pyridine adsorption. This difference is explained by the dehydrogenation of amine hydrogens prior to the cleavage of C-H bonds in the rings.<sup>18</sup> The first H<sub>2</sub> desorption peak for piperidine creates a pyridine intermediate, and subsequent H<sub>2</sub> desorption mirrors the desorption profile of the H<sub>2</sub> TPD spectra in Chapter 3. Both have a peak near 490 K and a broad feature above 500 K, which broadens with higher exposures. Desorption features after 350 K correspond to dehydrogenation of ring carbons, since vibrational studies revealed no evidence of pyridine after warming the surface to this temperature.

Cyclohexylamine dehydrogenation yields H<sub>2</sub> desorption peaks similar to that of aniline on Pt(111), which indicates aniline may be present on the surface during dehydrogenation, but the activation barrier for dehydrogenation must be higher than the desorption barrier for aniline or benzene. All hydrogen is eliminated from surface species resulting from all three molecules by 800 K.

#### 5.4 Conclusion

Piperidine adsorption and reaction on Pt(111) and Sn/Pt(111) surfaces was monitored by TPD. On Pt(111), some reversible adsorption occurs and molecular desorption was observed at 226 and 281 K from the monolayer, and at 172 K from the multilayer on Pt(111). Decomposition of piperidine during heating in TPD produced



major gas phase products of H<sub>2</sub>, HCN, C<sub>2</sub>N<sub>2</sub>, and pyridine on Pt(111). Pyridine desorption clearly establishes pyridine as an intermediate in piperidine dehydrogenation. Hydrogen desorbed in clearly defined peaks indicating stepwise dehydrogenation and the formation of well-defined intermediates. Desorption of HCN at 531 K establishes an upper limit on the activation energy barrier for C-N bond cleavage of 32 kcal/mol. The influence of Sn in the Sn/Pt(111) alloy surface was to slightly weaken the adsorption of piperidine. No significant difference was observed in reaction products between the Pt and PtSn surfaces.

### 5.5 References

1. Furimsky, E.; Massoth, F.; *Catal. Rev. Sci. Eng.* **2005**, *47*, 297-489.
2. Lewandowski, M.; Sarbak, Z. *Appl. Catal., B* **2008**, *79*, 313-322.
3. Kliewer, C. J.; Somorjai, G. A. *Catal. Lett.* **2010**, *137*, 118-122.
4. Schoofs, G.R.; Benziger, J.B.; *J. Phys. Chem.* **1988**, *92*, 741-750.
5. Xu, C.; Tsai, Y.-L.; Koel, B.E.; *J. Phys. Chem.* **1994**, *98*, 585-593.
6. Carter, E.A.; Koel, B.E.; *J. Molec. Catal. A* **1998**, *101*, 2895-2906.
7. Haq, S.; King, D. A. *J. Phys. Chem.* **1996**, *100*, 16957-16965.
8. Grassian, V.H.; Muetterties, E.L.; *J. Phys. Chem.* **1986**, *90*, 5900-5907.
9. Johnson, A.L.; Muetterties, E.L.; Stöhr, J.; Sette, F.; *J. Phys. Chem.* **1985**, *89*, 4071-4075.
10. Lee, I.C.; Masel, R.I.; *J. Phys. Chem. B* **2002**, *106*, 368-373.
11. Gland, J.L.; Somorjai, G.A.; *Surf. Sci.* **1973**, *38*, 157-186.
12. Panja, C.; Saliba, N.A.; Koel, B.E.; *Catal. Lett.* **2000**, *68*, 175-180.
13. Zhao, H.; Koel, B.E.; *J. Phys. Chem.* **2009**, *113*, 18152-18162.
14. Jerdev, D.; Olivas, A.; Koel, B.E.; *J. Catal.* **2002**, *205*, 278-288.
15. Zhao, H.; Welch, L. A.; Koel, B. E. *Surf. Sci.*, **2009**, *603*, 3355-3360.
16. Huang, S.X.; Gland, J.L.; *J. Phys. Chem.* **1996**, *100*, 13629-13635.

17. Mudiyansele, K.; Trenary, M.; *Surf. Sci.* **2009**, *603*, 3215-3221.
18. Somers, J.S.; Bridge, M.E.; *Surf. Sci.* **1985**, *159*, L439-444.
19. Jentz, D.; Celio, H.; Mills, P.; Trenary, M.; *Surf. Sci.* **1995**, 1-8.
20. Zhao, H.; Koel, B. E. *J. Phys. Chem. C* **2009**, *113*, 18152-18162.
21. Tsai, Y.-L.; Koel, B.E. *J. Phys. Chem. B* **1997**, *101*, 2895-2906.
22. Tsai, Y.-L.; Xu, C.; Koel, B.E.; *Surf. Sci.* **1997**, *385*, 37-59.
23. Zhao, H.; Koel, B.E.; *J. Phys. Chem.* **2009**, *113*, 18152-18162.
24. Peck, J.W.; Koel, B.E.; *J. Am. Chem.Soc.*, **1994**, *118*, 2708-2717.
25. Bridge, M.E.; Somers, J.; *Vacuum* **1988**, *38*, 317-320.
26. Kang, D.-H.; Trenary, M.; *Surf. Sci.* **2002**, *519*, 40-56.
27. Kang, D.-H.; Chatterjee, B.; Herceg, E.; Trenary, M.; *Surf. Sci.* **2003**, *540*, 23-38.

## Chapter 6: Thermal Decomposition of Metal Oxides Formed by NO<sub>2</sub> Oxidation

### 6.0 Abstract

High-resolution x-ray photoelectron spectroscopy (HR-XPS) was used to study the oxidation of a ( $\sqrt{3}\times\sqrt{3}$ )R30° Sn/Pt(111) surface alloy with NO<sub>2</sub> and consequent thermal reduction. Platinum 4*f*, Sn 3*d*, and O 1*s* XPS regions were monitored by HR-XPS. The O 1*s* XPS region was decomposed into three oxygen peaks due to oxygen in an oxide form with Sn, oxygen in a quasimetallic environment with Sn, and oxygen species in a hydroxyl species on the surface. The HR-XPS spectra show that NO<sub>2</sub> oxidized the Sn in the surface alloy, but no evidence was seen for oxidation of platinum under ultrahigh vacuum (UHV) conditions using NO<sub>2</sub>. Heating the surface thermally decomposed the Sn oxide species to leave a metallic surface. The decomposition of quasimetallic Sn was observed below 700 K, while the decomposition of Sn<sup>4+</sup> was observed at 743 K. Formation of platinum oxide must be accomplished with a stronger oxidizing agent.

### 6.1 Introduction

Supported PtSn catalysts with Sn in an oxidized form have been shown to improve catalytic reforming processes,<sup>1-3</sup> as well as the selective hydrogenation of  $\alpha,\beta$ -unsaturated aldehydes.<sup>4-7</sup> Fundamental studies of the oxidation of PtSn alloys and the thermal stability of the oxide phases formed help clarify the role of these oxides in such catalytic processes. In this chapter, we present results from surface science studies of the oxidation and thermal reduction of a  $\sqrt{3}\text{Sn}/\text{Pt}(111)$  surface alloy using NO<sub>2</sub> as an aggressive oxidant to simulate higher pressure O<sub>2</sub> conditions.

Several surface-science studies have been done previously to understand the oxidation of ordered Pt and PtSn surfaces. Saliba, et al., used ozone (O<sub>3</sub>) to oxidize the Pt(111) surface.<sup>8</sup> There was a shift observed in the Pt NNO Auger peak from 236.8 eV at  $\Theta_{\text{O}}=0.11$  ML to 236.0 eV at  $\Theta_{\text{O}}=2$  ML, indicating the formation of Pt oxide species. NO<sub>2</sub> has also been utilized to oxidize the Pt(111) surface, and surface characterization was accomplished with high resolution electron energy loss spectroscopy (HREELS) and temperature programmed desorption (TPD).<sup>9</sup> In these studies, the surface was heated to

400 K to remove coadsorbed NO from NO<sub>2</sub> decomposition without causing any oxygen (O<sub>2</sub>) desorption.

The Weaver group used an oxygen atom source, which emits ion-free atomic oxygen by using a gas cracker, to oxidize Pt surfaces and form Pt oxide.<sup>10,11</sup> Oxidation of a Pt(100) surface caused peak broadening in X-ray photoelectron spectroscopy (XPS) data in the Pt 4*f* region.<sup>11</sup> At  $\Theta_{\text{O}} = 1.0$  ML, no broadening of the Pt signal was observed, but as the oxygen coverage grew to 1.8 and 3.1 ML, a noticeable shoulder appeared on the high-BE side of the Pt 4*f* peaks, which signified the production of Pt oxide species. Oxidation of the Pt(111) surface also produced this high-BE shoulder on the Pt 4*f* peaks after reaching oxygen coverages above 1.1 ML, where noticeable broadening was observed at oxygen coverages of 1.5 and 2.6 ML.<sup>10</sup> These high-binding energy shoulders observed in oxidized platinum XPS data provide a reference for comparison to this thesis work. However, no evidence of platinum oxide was found in the experiments for this thesis.

One study investigated the oxidation of Pt(111) by O-atom dosing and analyzed the surface by angle-resolved XPS.<sup>12</sup> After exposure to 50 L of atomic oxygen, reducing the take-off angle from 90° to 15° revealed a more pronounced, high-BE shoulder (shifted by 2.3 eV) on the Pt 4*f* peaks as the angle dropped. The O 1*s* spectra showed two species of oxygen at 530.2 and 530.8 eV BE.

Oxidation of two surface alloys-(2×2) Sn/Pt(111) and ( $\sqrt{3}\times\sqrt{3}$ )R30° Sn/Pt(111)- have been studied, and we will refer to these as the 2×2 and  $\sqrt{3}$  alloys, respectively, for brevity. Oxidation of the 2×2 and  $\sqrt{3}$  surface alloys by O<sub>2</sub> was determined to be dependent on temperature.<sup>13</sup> The oxygen uptake increased as the temperature of the 2×2

surface was increased from 380 to 425 K. The oxygen uptake at 425 K for the  $\sqrt{3}$  surface, up to an oxygen coverage of 1.4 ML, was higher than for the  $2\times 2$  surface, at 425 K up to 1.2 ML. No evidence for the oxidation Pt was seen in XPS, but Sn was oxidized. The Sn  $3d_{5/2}$  peak had three components, which were located at 484.9, 485.5, and 486.3 eV BE after exposure to oxygen causing coverages of oxygen  $\Theta_{\text{O}}=1.2$  and 1.4 ML on the  $2\times 2$  and  $\sqrt{3}$  alloys, respectively. The lowest BE component was designated as metallic Sn, while the middle- and high-BE components were assigned to quasimetallic and oxidic Sn species, respectively. The so-called quasimetallic Sn species refers to Sn atoms in intimate contact with Pt, but that are also partially oxidized with an oxidation state between zero and plus two. The O  $1s$  spectra revealed two types of oxygen on the surface at 529.7 and 531.8 eV. The low-BE component was labeled as a combination of oxygen in the oxidic and quasimetallic species, while the higher-BE component was assigned to hydroxyl contamination at the surface. The location of the O  $1s$  BE peaks was not affected by the concentration of Sn in the surface alloy.

Ozone ( $\text{O}_3$ ) is a stronger oxidant than molecular oxygen, and oxidation of the PtSn surface alloys by ozone was done to show the difference in oxide.<sup>14</sup> Oxidation of the surface alloys by ozone permits much larger oxygen coverages than ultrahigh vacuum (UHV) exposures of  $\text{O}_2$  and  $\text{NO}_2$  (discussed later).  $\text{O}_2$  TPD spectra after exposures of ozone on the  $2\times 2$  alloy showed desorption peaks at 730, 820, 960, and 1015 K. After exposures of ozone to the  $\sqrt{3}$  alloy,  $\text{O}_2$  desorption was observed at 730, 760, 834, 1002, and 1078 K. Auger electron spectroscopy (AES) spectra showed a shift in the Sn peak from 430.1 eV kinetic energy (KE) at  $\Theta_{\text{O}}=0.2$  ML to 428.5 eV at  $\Theta_{\text{O}}=1.2$  ML for the  $2\times 2$  surface, and a similar shift was observed for the  $\sqrt{3}$  surface. No shifts in Pt AES spectra

were reported. Unpublished data from Saliba, et al compared O<sub>2</sub> desorption after O<sub>3</sub> exposures on Pt(111), the two PtSn surface alloys, and a thick Sn film.<sup>15</sup> Analysis of this data pointed to a destabilization of a tin oxide species when Sn was alloyed with Pt. The evidence for this conclusion was in the drop in O<sub>2</sub> desorption peak from 1172 K on the thick Sn film to 836 and 820 K on the  $\sqrt{3}$  and 2×2 surface alloys, respectively. Desorption of O<sub>2</sub> from Pt(111) was even lower, at 707 K. Analysis of these systems with HR-XPS would explain the identity of these surface species.

Oxidation of the 2×2 and  $\sqrt{3}$  alloys was also accomplished by exposures of NO<sub>2</sub> at 400 K.<sup>16-19</sup> Oxygen uptake measurements were made by dosing NO<sub>2</sub> on the alloys at 400 K, because previous work showed that NO<sub>2</sub> dissociates on the surfaces to form NO<sub>ads</sub> and O<sub>ads</sub> and that all adsorbed NO desorbs below 400 K to leave adsorbed oxygen atoms cleanly on the surface. O<sub>2</sub> desorbs only after warming the surface to near 600 K, so dosing NO<sub>2</sub> at 400 K is an efficient technique for preparing oxygen-covered surfaces. Coverages of oxygen produced by this method have a maximum at 0.75 ML.<sup>16</sup>

Analysis by XPS of both PtSn surface alloys after oxidation by NO<sub>2</sub> showed three Sn species at 486.5 eV, 485.5 eV, and 484.9 eV. These binding energies were correlated to oxidized Sn, quasimetallic Sn, and metallic Sn, respectively.<sup>17</sup> No calculated coverages of oxygen were reported in this paper after NO<sub>2</sub> exposures. Though it was not shown in a published figure, a shift in the Pt 4f signal was reported to have a shift of +0.2 eV after oxidation and this shift disappeared after annealing to 840 K.

A number of oxidic nanostructures have been observed on the  $\sqrt{3}$  alloy after oxidation by NO<sub>2</sub> and annealing, and these were characterized with XPS, low energy electron diffraction (LEED) and scanning tunneling microscopy (STM).<sup>18</sup> XPS showed

three forms of Sn at 484.6, 485.0, and 486.0 eV BE and these were assigned as metallic Sn, quasimetallic Sn, and SnO<sub>2</sub>, respectively.<sup>16</sup> Glancing-angle XPS data exhibited an enhanced concentration of the higher-BE oxidic Sn<sup>4+</sup> state and lower-BE Sn<sup>0</sup> components and a reduction in the quasimetallic component. Perpendicular take-off angle data showed enhanced concentrations of the quasimetallic Sn. The O 1s data was decomposed into two components at 529.9 and 528.8 eV BE, each with a full-width-at-half-maximum (FWHM) of 1.4 eV. The higher-BE component was assigned to oxidic Sn in SnO<sub>2</sub> and the lower-BE component was assigned to oxygen bound to quasimetallic Sn.

As this review shows, oxidation of Pt in PtSn alloys was detected by XPS after exposures by ozone (O<sub>3</sub>) and an O atom source. In other studies, it was concluded that NO<sub>2</sub> was not strong enough to oxidize Pt in UHV, though it easily oxidized Sn. However, high-resolution XPS (HR-XPS) had not been carried out to verify this conclusion. This chapter presents HR-XPS data obtained with a Scienta ESCA 300 instrument to investigate whether or not NO<sub>2</sub> oxidizes Pt in the PtSn alloys previously studied in UHV. We were also interested in obtaining new data on the Sn oxidation state as the Sn oxide species decompose due to thermal reduction. A previous study of these alloys oxidized by ozone showed that an oxygen desorption peak appeared between the temperatures at which Pt oxide decomposed on the Pt(111) surface and Sn oxide decomposed from a thick film of Sn oxide.<sup>15</sup> The origin of this oxygen desorption peak was undetermined. Stepwise heating of the oxidized surface in combination with HR-XPS data should be helpful in determining what changes in oxidation state at the surface occurred during thermal decomposition of oxide species.

## 6.2 Experimental Methods

This experiment was carried out in the Scienta ESCA facility at Lehigh University. The base chamber pressure in the analysis chamber for this experiment was  $1 \times 10^{-9}$  Torr. The Pt(111) crystal was cleaned in an attached preparation chamber by Ar<sup>+</sup> sputtering, and then the crystal was annealed to 1200 K for 30 s after transferring it to a custom electron beam heater stage in the preparation chamber. A survey XPS spectrum showed that the surface was clean except for a small amount of Sn. No oxygen or carbon contamination was detectable. Tin was evaporated from the Sn doser onto the crystal with a current of 21 A for 3.5 minutes. The Sn doser was described in Section 2.1. The crystal was then annealed using the electron beam heater to 770 K for approximately 10 s. The  $\sqrt{3}$  Sn/Pt(111) surface alloy was observed via the LEED pattern obtained at a beam energy of 70 eV. An example of the LEED image was shown in Section 2.5. HR-XPS survey spectra and regional spectra (Pt 4*f*, Sn 3*d*<sub>5/2</sub>, and O 1*s*) were obtained with the photoelectron take-off angle of 25° away from the surface plane. Pass energies were 300 eV for the O 1*s* spectra, 75 eV for the Pt 4*f* spectra, 150 eV for the Sn 3*d* spectra, and 150 eV for the survey spectra and the acquisition time for each series of spectra was 20 minutes. Spectra were fitted using the CasaXPS software using a linear background subtraction. For the Sn 3*d* spectra, a Gaussian-Lorentzian (GL) function of GL(85) was used. For the O 1*s* spectra, a GL(60) line shape was used.

The crystal was warmed on the sample heater in the analysis chamber until the thermocouple at the base of the stub read approximately 430 K. Previous measurements showed that the crystal on the stub is approximately 30 K lower than this reading. With the crystal warmed to 400 K, 6 L NO<sub>2</sub> was dosed on the crystal from a dosing tube in



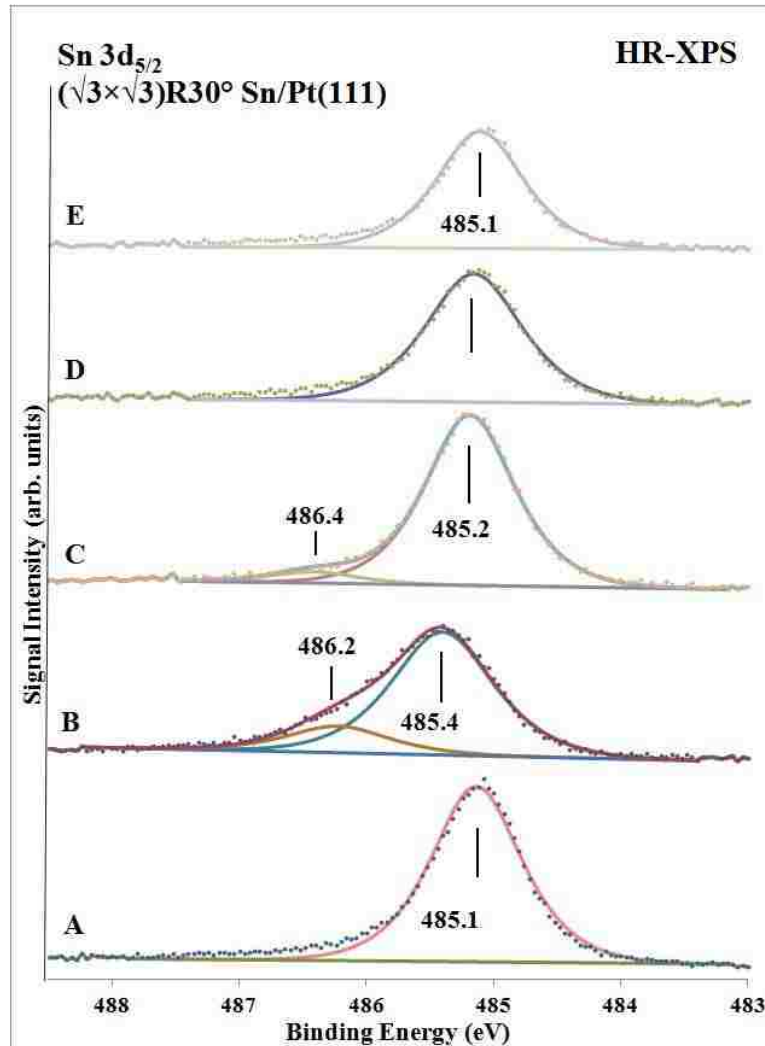
direct line of sight of the crystal surface. This dose was determined to be more than a saturation dose because larger doses did not increase the O:Pt XPS signal ratio. Gaskets in the doser line were gold-coated to limit side reactions, and the NO<sub>2</sub> line was flushed between doses.

HR-XPS scans were taken for the clean and dosed surfaces, and then the surface was heated incrementally and HR-XPS data were taken after each heating step. The crystal had to be transferred to the preparation chamber to be heated on the electron beam heater to temperatures of 700, 743, and 1000 K. The crystal was heated to each annealing temperature for 30 s. After each of these heating steps, the crystal was cooled to room temperature, transferred back to the analysis chamber, and HR-XPS data were taken. The entire process took less than 3 min from the time annealing ended to starting the HR-XPS scanning, and 20 min until completion of the HR-XPS spectra.

### 6.3 Results and Discussion

The Sn  $3d_{5/2}$  HR-XPS spectra are displayed in Figure 6.1. The peak positions and FWHM values for each Sn peak are organized in Table 6.1. The Sn  $3d_{5/2}$  peak from the clean  $\sqrt{3}$  PtSn alloy is given in Figure 6.1A and has a FWHM of 0.8 eV at 485.1 eV BE. After the maximum NO<sub>2</sub> exposure, the peak broadened to 0.9 eV FWHM and it can be decomposed into two species at 485.4 and 486.2 eV BE. The low-BE species is assigned to quasimetallic Sn and the high-BE species is assigned to oxidized Sn in the form of SnO<sub>2</sub>. This result is consistent with previous XPS studies of the oxidation of this alloy showing peaks at 485.0 and 486.0 eV BE.<sup>16</sup> Heating the surface to 700 K reduced the intensity of the high BE peak and this narrowed the FWHM to 0.8 eV and shifted the overall peak to lower BE. Annealing to 743 K caused further reduction of the intensity of

the high BE peak and narrowing of the FWHM. Annealing to 1000 K removed all oxidized Sn peaks and produced a Sn peak at 485.1 eV with a FWHM of 0.8 eV, identical to that in curve A.



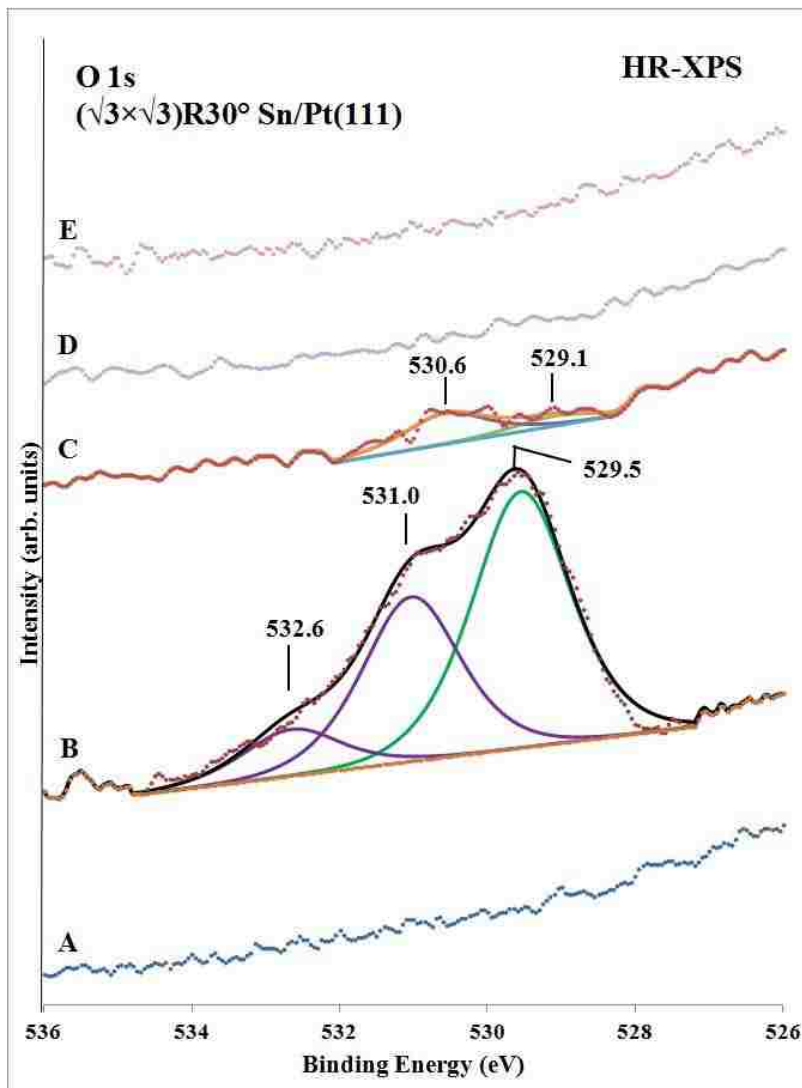
**Figure 6.1** Sn  $3d_{5/2}$  HR-XPS spectra of the  $(\sqrt{3}\times\sqrt{3})R30^\circ$  Sn/Pt(111) alloy before and after oxidation by  $\text{NO}_2$  and thermal reduction: (A) clean  $\sqrt{3}$  alloy; (B)  $\sqrt{3}$  alloy after maximum exposure at 400 K; (C) after thermal reduction of (B) by annealing to 700 K; (D) after thermal reduction of (C) by annealing to 743 K; and (E) after thermal reduction of (D) by annealing to 1000 K.

Figure 6.2 presents HR-XPS spectra for the O 1s region obtained at the same time as those in Fig. 6.1. Following the NO<sub>2</sub> exposure, Figure 6.2B indicates three species of oxygen at 529.5, 531.0, and 532.6 eV BE, all with a FWHM of 1.3 eV. The

	<i>Binding Energy</i> (eV)	<i>FWHM</i> (eV)
Clean Surface	485.1	0.8
Oxidized with NO <sub>2</sub>	485.4	0.9
	486.2	0.9
Annealed to 700 K	485.2	0.8
	486.4	0.8
Annealed to 743 K	485.2	0.8
Annealed to 1000 K	485.1	0.8
<i>a. Full width at half maximum (FWHM)</i>		

peak at 532.6 eV is attributed to hydroxyl groups formed by water contamination from background gas exposure. The high partial pressure of H<sub>2</sub> present in the analysis chamber, while it may reduce the amount of oxygen due to water formation and evolution, does not contribute to this hydroxyl peak, as shown in high pressure photoemission spectroscopy (HP-PES) experiments.<sup>20</sup> The peak at 531.0 eV BE is attributed to oxygen in SnO<sub>2</sub>, while the lower-BE peak at 529.5 eV BE is assigned to oxygen associated with quasimetallic Sn. The largest oxygen component is the quasimetallic oxygen species, followed by oxidic oxygen and then the hydroxyl contaminant. The assignments of the SnO<sub>2</sub> and quasimetallic components are based on the assignments of Batzill, et al, who reported O 1s peaks due to SnO<sub>2</sub> at 529.9 eV and oxygen with quasimetallic Sn at 528.8 eV.<sup>16</sup> After exposures of NO<sub>2</sub> on the  $\sqrt{3}$  alloy at 600 K, desorption of O<sub>2</sub> in TPD was observed at 804 and 1084 K.<sup>19</sup> The desorption peak

at 804 K begins near 650 K and corresponds to the decomposition observed in XPS in this thesis after warming to 700 K. The high-temperature O<sub>2</sub> desorption in TPD in ref. 34 cannot be explained by this HR-XPS data.



**Figure 6.2** O 1s spectra of the  $(\sqrt{3}\times\sqrt{3})R30^\circ$  Sn/Pt(111) alloy before and after oxidation by NO<sub>2</sub> and thermal reduction: (A) clean  $\sqrt{3}$  alloy; (B)  $\sqrt{3}$  alloy after maximum exposure at 400 K; (C) after thermal reduction of (B) by annealing to 700 K; (D) after thermal reduction of (C) by annealing to 743 K; and (E) after thermal reduction of (D) by annealing to 1000 K.

Heating the surface to 700 K removed nearly all of the surface oxygen and all of the hydroxyl contaminants. Heating the surface to 743 K or above caused all remaining

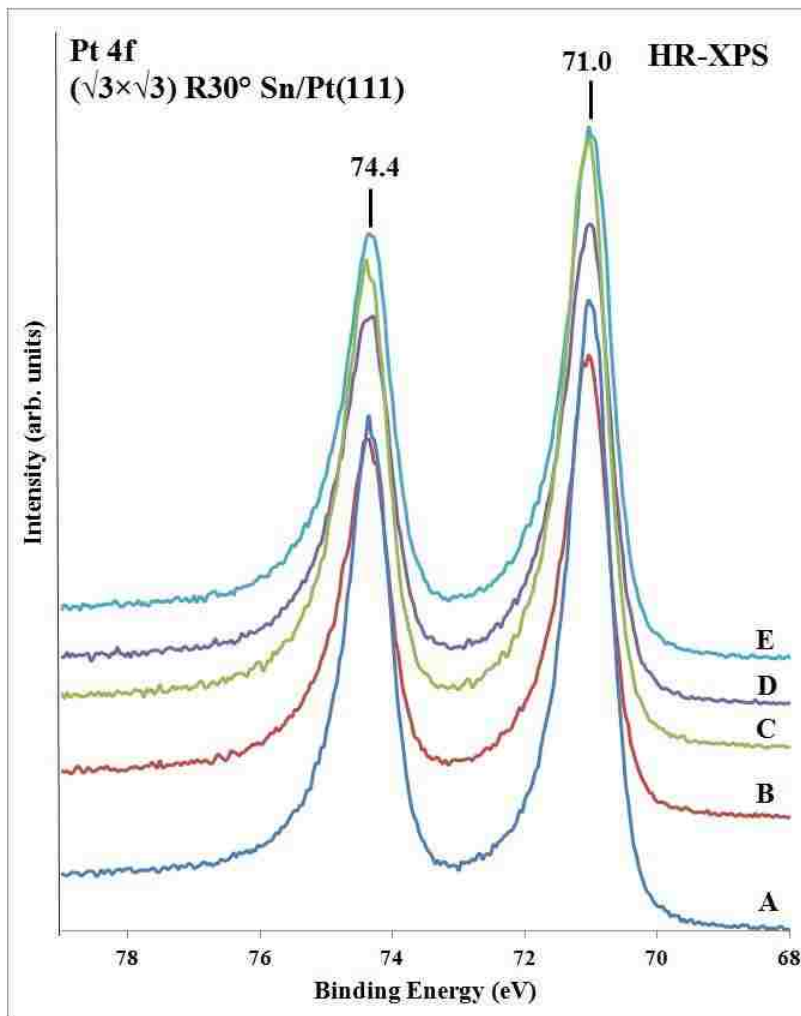


**Figure 6.3** Pt 4f spectra of the  $(\sqrt{3}\times\sqrt{3})R30^\circ$  Sn/Pt(111) alloy before and after oxidation by  $\text{NO}_2$  and thermal reduction: (A) clean  $\sqrt{3}$  alloy; (B)  $\sqrt{3}$  alloy after maximum exposure at 400 K; (C) after thermal reduction of (B) by annealing to 700 K; (D) after thermal reduction of (C) by annealing to 743 K; and (E) after thermal reduction of (D) by annealing to 1000 K.

oxygen to desorb, as seen in Figures 6.2D-E. HR-XPS spectra from the Pt 4f region shown in Figure 6.3 did not show any sign of Pt oxidation through peak broadening or

appearance of a new high-BE peak after NO<sub>2</sub> exposure. The curves were completely superimposable.

The HR-XPS data obtained in these experiments showed that exposure of the  $\sqrt{3}$  PtSn alloy to NO<sub>2</sub> caused Sn oxidation, but no Pt oxidation. Subsequently, after warming the surface to 700 K, much of the surface oxygen was removed, and also indicated that both the quasimetallic and hydroxyl oxygen species are less thermally stable than the oxidic species. All remaining oxygen on the surface disappeared after warming the surface to 743 K. This is sharp disagreement with previous results of O<sub>2</sub> TPD, which show a high-temperature desorption peak at 1084 K due to a stable Sn oxide species, and we are forced to conclude that the high partial pressures of H<sub>2</sub> and CO in the chamber that react with and remove surface oxygen do not allow us to make conclusions about the thermal stability of Sn oxide species in UHV. Unpublished work by Liu et al showed the facile H<sub>2</sub> reduction of Sn/Pt(111) surfaces oxidized by NO<sub>2</sub>.<sup>20</sup>

#### 6.4 Conclusion

A ( $\sqrt{3}\times\sqrt{3}$ )R30° Sn/Pt(111) surface alloy was oxidized with NO<sub>2</sub> in UHV and then monitored with HR-XPS during thermal reduction in vacuum. We confirm previous conclusions that exposure of PtSn alloy surfaces to NO<sub>2</sub> does not form platinum oxide at 400 K under UHV conditions. Tin was oxidized to form Sn<sup>4+</sup> and quasimetallic Sn, but no evidence of oxidized Pt was observed. Heating the surface thermally decomposed the Sn oxide species to leave a metallic surface. The decomposition of quasimetallic Sn was observed below 700 K, while the decomposition of Sn<sup>4+</sup> was observed at 743 K.

## 6.5 References

1. Mal, N. K.; Sasidharan, M.; Matsukata, M.; Sivasanker, S.; Ramaswamy, A. V. *Stud. Surf. Sci. Catal.* **2004**, *154C*, 2403-2410.
2. Fuercht, A.; Tungler, A.; Szabob, S. *React. Kinet. Catal. Lett.* **2002**, *76*, 227-233.
3. Rangel, M. C.; Carvalho, L. S.; Reyes, P.; Parera, J. M.; Figoli, N. S. *Catal. Lett.* **2000**, *64*, 171-178.
4. Merlo, A. B.; Machado, B. F.; Vetere, V.; Faria, J. L.; Casella, M. L. *Appl. Catal. , A* **2010**, *383*, 43-49.
5. Ruiz-Martinez, J.; Coloma, F.; Sepulveda-Escribano, A.; Anderson, J. A.; Rodriguez-Reinoso, F. *Catal. Today* **2008**, *133-135*, 35-41.
6. Merlo, A. B.; Santori, G. F.; Sambeth, J.; Siri, G. J.; Casella, M. L.; Ferretti, O. A. *Catal. Commun.* **2006**, *7*, 204-208.
7. Abid, M.; Ammari, F.; Liberkova, K.; Touroude, R. *Stud. Surf. Sci. Catal.* **2003**, *145*, 267-270.
8. Saliba, N. A.; Tsai, Y. L.; Panja, C.; Koel, B. E. *Surf. Sci.* **1999**, *419*, 79-88.
9. Bartram, M.E.; Windham, R.G.; Koel, B.E.; *Langmuir*, **1988**, *4*, 240-246.
10. Weaver, J. F.; Chen, J. J.; Gerrard, A. L. *Surf. Sci.* **2005**, *592*, 83-103.
11. Shumbera, R. B.; Kan, H. H.; Weaver, J. F. *Surf. Sci.* **2007**, *601*, 235-246.
12. Parkinson, C. R.; Walker, M.; McConville, C. F.; *Surf. Sci.* **2003**, *545*, 19-33.
13. Jerdev, D. I.; Koel, B. E. *Surf. Sci.* **2001**, *492*, 106-114.
14. Saliba, N. A.; Tsai, Y. L.; Koel, B. E. *J. Phys. Chem. B* **1999**, *103*, 1532-1541.
15. Saliba, N. A. *unpublished work*.
16. Batzill, M.; Kim, J.; Beck, D. E.; Koel, B. E. *Phys. Rev. B* **2004**, *69*, 165403-165414.
17. Batzill, M.; Beck, D.E.; Jerdev, D.; Koel, B.E.; *J. Vac. Sci. Technol. A*, **2001**, *19*, 1953-1958.
18. Batzill, M.; Beck, D. E.; Koel, B. E. *Phys. Rev. B* **2001**, *64*, 245402-245412.

19. Voss, M. R.; Zhao, H.; Koel, B. E. *Surf. Sci.* **2004**, *560*, 235-245. 12.
20. Liu, G. *unpublished work*, **2009**.



## Chapter 7: Summary and Outlook

The research presented in this dissertation extends previous investigations of a number of hydrocarbon and organic molecules on Pt(111) and Sn/Pt(111) surfaces, using primarily temperature programmed desorption (TPD). This research was inspired mainly by the recent strengthening of government regulations regarding reducing diesel engine emissions, the need for more efficient HDN catalysts, as well as an interest in probing the surface chemistry of a large class of hydrocarbons that contain N heteroatoms on Pt and Pt alloys. The specific contributions of the research presented in this thesis is a better understanding of the basic surface chemistry and decomposition of three different nitrogen-containing cyclic compounds with varying levels of saturation on Pt(111) surfaces. Pyridine, piperidine, and cyclohexylamine were studied by TPD.

Reaction of these molecules on Pt(111) formed desorption products including H<sub>2</sub>, HCN, and C<sub>2</sub>N<sub>2</sub>. Desorption of H<sub>2</sub> from the dehydrogenation of cyclohexylamine and piperidine began at a lower temperature than pyridine due to a lower activation barrier for the cleavage of N-H bonds versus C-H bonds. Piperidine was the only molecule to react and cause a large, stable dehydrogenation product, pyridine. All three molecules underwent stepwise dehydrogenation, which was evidenced by sharp, well-defined H<sub>2</sub> desorption peaks in TPD.

Comparison of piperidine adsorption on Pt(111) and a Sn/Pt(111) alloy revealed that Sn weakened the interaction between the molecule and the surface, consistent with previous studies on other hydrocarbons. In the future, high-pressure catalysis experiments using these single crystal model catalysts should be able to establish the

expected increase in selectivity of Sn/Pt(111) alloys over that of Pt(111) to catalyze HDN of such molecules.

The high-resolution X-ray photoelectron spectroscopy (HR-XPS) work in this thesis extended previous research aimed at understanding the oxidation of PtSn alloys and the thermal stability of Sn oxides formed. Oxidation of a Sn/Pt(111) alloy surface by exposure to NO<sub>2</sub> was shown to create Sn oxide, but not Pt oxide. This establishes and confirms previous preliminary conclusions from that NO<sub>2</sub> is not strong enough to cause the oxidation of Pt in UHV. Future studies using HR-XPS of the oxidation of these PtSn alloys and the thermal stability of mixed metal oxides formed on these PtSn alloys could easily be carried out using a more efficient oxidant (i.e. ozone, O plasma, or O atom source).

Curriculum Vitae  
Lindsey A. Welch, Ph.D.c.  
310 Saucon View Drive • Bethlehem, PA 18015  
LAWelch@cedarcrest.edu • (570) 974-9656

**SUMMARY:** I am a Ph.D. level chemist trained in physical and inorganic chemistry. I am self-motivated with a passion for teaching. In addition to my experience as a teaching assistant at Lehigh University and Lycoming College, I have volunteered at science fairs to inspire local youth to follow an educational path in the sciences. While at Lehigh I attended seminars for teaching development and sat on the University Committee on Discipline to promote academic integrity on campus.

**EDUCATION:**

**Ph.D., Lehigh University**, Bethlehem, PA 2012  
Dissertation: “Surface Science Studies of Nitrogen-Containing Cyclic Hydrocarbons on Pt(111) and Sn/Pt(111) Surface Alloys”  
Advisor: Prof. Bruce E. Koel

**B.S., Lycoming College**, Williamsport, PA 2006  
Major: **Chemistry**  
Minor: **Biology**

**EMPLOYMENT / TEACHING EXPERIENCE:**

**Inorganic Chemistry Instructor** August 2011-Present  
*Cedar Crest College, Allentown, PA*

- Concepts in Chemistry - CHE 103
- Inorganic Chemistry lecture and laboratory - CHE 331
- Physical Chemistry laboratory - CHE 335
- Physical Chemistry II lecture - CHE 336
- Instrumental Analysis laboratory - CHE 302
- Advising undergraduate research project: “Selective Liquid-phase Hydrogenation of Cinnamaldehyde Using a Pd/C Catalyst”

**Adjunct Instructor** August 2011-Present  
*Pennsylvania State University – Lehigh Valley Campus, Center Valley, PA*

- Teaching Experimental Chemistry Laboratory – CHM 111

**Adjunct Instructor** August 2011-June 2012  
*Lehigh Carbon Community College, Schnecksville, PA*

- Teaching Physiological Chemistry lecture and laboratory to nursing/health profession students- CHE 106 and CHE 106L

**Research Assistant** May 2007-August 2011  
*Lehigh University, Bethlehem, PA*

- Investigated the surface science of Pt-Sn alloy catalysts by studying model single crystal systems by UHV surface techniques and electron spectroscopies

**Teaching Assistant** Fall 2006-Fall 2009  
*Lehigh University, Bethlehem, PA*

- Taught General, Organic, and Physical Chemistry Laboratories
- Prepared lab experiments, oversaw lab activities, graded lab reports, notebooks, lecture exams

**Chemistry Tutor** January-June 2008  
*Private Tutoring, Bethlehem, PA*

- Tutored a high school sophomore in chemistry.

**Student Researcher** Spring 2006  
*Lycoming College, Williamsport, PA*

- “Chelation-Assisted Intramolecular Hydroacylation: Synthesis of Medium Rings”- Wilkinson’s (**homogenous**) Rh catalyst used for synthesis of medium rings from carbon chain with S tether atom.

**Chemistry Laboratory and Teaching Assistant** Fall 2003-Fall 2005  
*Lycoming College, Williamsport, PA*

- Taught General and Organic Chemistry Laboratories
- Oversaw lab activities, graded lab reports

**Nurse Extender / Home Health Aide / Hospice Aide** May 2003-July 2006  
*Susquehanna Health System, Williamsport, PA*

## **INSTRUMENTATION / LABORATORY EXPERIENCE:**

HR-XPS (High Resolution – X-ray Photoelectron Spectroscopy (Scienta ESCA 300)  
TPD – Temperature Programmed Desorption      AES – Auger Electron Spectroscopy  
MS – Mass Spectrometry      UHV – Ultra-High Vacuum  
LEED – Low Energy Electron Diffraction      Basic scientific glass blowing

## **PUBLICATIONS:**

1. **Welch, L. A.**; Koel, B. E. “A Review of Reactions over Pt-Sn Bimetallic Catalysts and Surfaces: The Role of Pt-Sn Alloys” *Catalysis Reviews: Science and Engineering*, to be submitted.
2. Kim, J.; **Welch, L. A.**; Olivas, A.; Podkolzin, S. G.; Koel, B. E. “Adsorption and Decomposition of Cyclohexanone on Pt(111) and the (2×2) and ( $\sqrt{3}\times\sqrt{3}$ )R30°-Sn/Pt(111) Surface Alloys” *Langmuir*, **2010**, *26*, 16401-16411.

3. Yang, X.; **Welch, L. A.**; Fu, J.; Koel, B. E. "Surface Structure of Pd<sub>3</sub>Fe(111) and Effects of Oxygen Adsorption," Proceedings of the Materials Research Society Fall 2009 Symposium, Boston, MA, November 3 - December 4, 2009, submitted. Y: Catalytic Materials for Energy, Green Processes, and Nanotechnology.
4. Zhao, H.; **Welch, L. A.**; Koel, B. E. "Site-blocking effects of preadsorbed H on Pt(111) probed by 1,3-butadiene adsorption and reaction" *Surf. Sci.*, **2009**, *603*, 3355-3360.

*Acknowledged in:*

Zhao, H.; Koel, B. E. "Probing selectivity over Pt-Sn catalysts in reactions of n-C<sub>6</sub> hydrocarbons: Adsorption and reactivity of n-hexane, 1-hexene, and 1,5-hexadiene on Pt(111) and Sn/Pt(111) surface alloys" *J. Phys. Chem. C*, **2009**, *113*, 18152-18162.

**PRESENTATIONS:**

March 16, 2011 – "Decomposition of Pyridine (C<sub>5</sub>H<sub>5</sub>N) on Pt(111)" **Welch, L.A.**; Koel, B.E. The Catalysis Society of Metropolitan New York Spring Symposium Poster Session, Rutgers University, Piscataway, NJ

March 17, 2010 – "Steady State Kinetics of Adsorption and Reaction of 1,3-Cyclohexadiene on Pt(111) and Ordered Sn/Pt(111) Alloy Surfaces" **Welch, L.A.**; Koel, B.E. The Catalysis Society of Metropolitan New York Spring Symposium Poster Session, Lehigh University, Bethlehem, PA

February 18, 2010 – "Adsorption and Reaction of Cyclohexanone (C<sub>6</sub>H<sub>10</sub>O) on Pt(111) and the (2×2) and (√3×√3)R30°-Sn/Pt(111) surface alloys" Kim, J.; **Welch, L. A.**; Olivas, A.; Podkolzin, S. G.; Koel, B. E. Invited Talk for CHE 352 Chemistry Seminar Course, Chemistry Dept., Cedar Crest College, Allentown, PA

November 17, 2008 – "Adsorption and Reaction of Cyclohexanone (C<sub>6</sub>H<sub>10</sub>O) on Pt(111)" Kim, J.; **Welch, L. A.**; Olivas, A.; Koel, B. E. 47<sup>th</sup> Eastern Analytical Symposium & Exposition: Poster Session, Garden State Exhibit Center, Somerset, NJ

June 11, 2008 – "Adsorption and Reaction of Cyclohexanone (C<sub>6</sub>H<sub>10</sub>O) on Pt(111)" Kim, J.; **Welch, L. A.**; Olivas, A.; Koel, B. E. AVS 30<sup>th</sup> Annual Symposium on Applied Surface Analysis Poster Session, The Pennsylvania State University, University Park, PA

March 25, 2008 – "Adsorption and Reaction of Cyclohexanone (C<sub>6</sub>H<sub>10</sub>O) on Pt(111)" Kim, J.; **Welch, L. A.**; Olivas, A.; Koel, B. E. The Catalysis Society of Metropolitan New York's Spring Symposium Poster Session, Seton Hall University, South Orange, NJ

## **ACADEMIC AND COMMUNITY SERVICE ACTIVITIES:**

Cedar Crest College Falcon Games – Judge  
Cedar Crest College ΓΣΕ – Rho Xi Chemistry Honor Society Adviser  
Lehigh University Committee on Discipline – Panel member in disciplinary hearings  
Lehigh University Graduate Research Review – Editor 2008-Present  
Lehigh Valley Science and Engineering Research Fair – Volunteer Judge  
Pennsylvania Junior Academy of Science – Volunteer Judge  
Graduate Student Senate Unit Representative  
Graduate Student Senate Secretary 2008-2009  
Graduate Student Team Captain Jingle Bell Run 5K 2009-2010  
Graduate Student Orientation Ambassador  
Girls on the Run Volunteer Running Buddy

## **AFFILIATIONS / HONORS:**

**American Chemical Society – Active in Lehigh Valley Chapter**  
American Vacuum Society  
Sigma Xi Scientific Research Society – Associate Membership  
Catalysis Society of Metropolitan New York  
National Association of Professional Women  
**LU Teacher Development Training: Level 1 Certificate**  
**Graduate Student Senate “Champion” Honor, 2011**  
Safe Zone Trained LGBTQIA Ally  
Lycoming College ΓΣΕ – Rho Delta Chemistry Honor Society  
Lycoming Scholars Program  
BBB Biology Honor Society – *Associate Member*  
Lycoming College Dean’s List  
Lycoming College Valedictorian Scholarship  
Lycoming College Chemistry Club – *Treasurer*  
Jaramillo Memorial Award for Spanish Achievement